

**RAMAN SPECTROSCOPY IN MoS₂-TYPE TRANSITION-METAL
DICHALCOGENIDES**

by

BRUNO RICARDO DE CARVALHO

Supervisor:

Marcos Assunção Pimenta

Co-supervisor(s):

Cristiano Fantini Leite

&

Mauricio Terrones

(from The Pennsylvania State University)

A thesis submitted in partial fulfillment of
the requirements for the degree of

Doctor of Philosophy

(Physics)

at the

UNIVERSIDADE FEDERAL DE MINAS GERAIS

February 2017

© Copyright by BRUNO RICARDO DE CARVALHO: *Raman spectroscopy*
in MoS₂-type transition-metal dichalcogenides
February 2017
All Rights Reserved

Supervisor:

Prof. Dr. Marcos Assunção Pimenta

Co-Supervisor(s):

Prof. Dr. Cristiano Fantini Leite

&

Prof. Dr. Mauricio Terrones

Departamento de Física
Instituto de Ciências Exatas
Universidade Federal de Minas Gerais
Belo Horizonte, Brazil

To my family.

ACKNOWLEDGMENTS

Throughout my years at Universidade Federal de Minas Gerais, I received help, support and assistance by many people, in which without them this thesis would not be possible.

I would like to express my gratitude to my advisor, Marcos A. Pimenta ("*Marquin*"), for his guidance, encouragement and support throughout the course of my thesis research. I owe him my scientific education, and learned from him how to approach of breaking down complex problems into simpler sub-problems that can be addressed more readily and directly. He gave me the freedom to explore what I wanted to pursue and taught me the importance of developing clear physical insights in research. As an inspiring and knowledgeable advisor, he was always available for countless discussions and chats, which often evolved from the one, very brief question I originally brought along.

I would like also to express my gratitude to my co-advisor Cristiano Fantini and to Prof. Leandro Malard, who lending me with numerous helps and set for me a high standard in graduate research, specially for their patience, help in setting-up experiments and availability to discuss physics.

All of the members of the Raman laboratory have been generous in sharing their knowledge and their equipment with me: Amanda Coimbra, Janaina, Elena del Corro, Sara Costa, Fabio, Eliel Silva, Rafael Gontijo, Rogério Amaral, Sangram. Also Luciano Moura, although he had already left when I joined the group, he was also lending me with numerous helps for my research project. Working in the Raman group has been a wonderful experience. I believe that the friendships built up here will continue beyond my graduate study.

To my friends in the Department of Physics: Juliana Alves, Ingrid, Regiane, Leandra, Bárbara Rosa, Alisson, Andreij, Edrian, Joilson and Yuri.

We have shared a lot during the past four years.

To the members leading the graduate Department of Physics: Paulo Sérgio, Juliana Miranda and Ana Luiza. They truly helped me a lot in my four years journey. Also to Shirley, from the library, for recommending good books and, patience on finding some really hard (sometimes unknown) articles.

I would also like to take this opportunity to express my gratitude toward Prof. Mauricio Terrones, whom accepted me in his group during my one year doctorate internship at Pennsylvania State University. He shaped my graduate path with his guidance and wisdom which I will carry throughout my scientific career.

All the Terrones's group members for the assistance they provided at all levels of the research project, and especially for their friendship. I should particularly mention, Zhong Lin, Victor Carozo, Simin Feng and Kazunori Fujisawa, who kindly introduced me to the group and lending me with numerous helps and set during my stay at Penn State. I have benefited much through a joint project with Yuanxi Wang, who is especially motivating and supportive. We had many discussions that are sparked with interesting ideas, and we made good progress in our research as a result of these discussions. I will carry these built friendships beyond my graduate study.

It is an extremely valuable experience to have met the Brazilian group in State College, or better, the members of *Natudos*: Robson Machado, Fernanda, Laura, Bernardo, Juliana, João, Gustavo Silveira, Clarissa, Agata, Caitano, Victor Motta, Regis, Welligton and Diego.

I would also like to thank my family for the support they provided me through my entire life. In particular, I am very grateful to Amanda, without whose love, and encouragement, I would not have finished this thesis.

I thank the Brazilian agencies FAPEMIG, CAPES and CNPq for funding

this thesis research and for belief in science in Brazil.

Many thanks to everybody!

CONTENTS

Contents vi

List of Tables viii

List of Figures ix

List of Publications xiii

Resumo xv

Abstract xvi

Welcome to the flatland 1

1 Introduction and Background 2

1.1 *Introduction* 2

1.2 *Raman active-modes in transition metal dichalcogenides* 4

1.3 *The optical property in transition metal dichalcogenides* 6

1.4 *Excitons in MoS₂* 7

1.5 *Outline of the Thesis* 10

2 Basic concepts on Raman scattering theory 12

2.1 *The macroscopic theory of Raman scattering* 12

2.2 *The microscopic theory of Raman scattering* 17

2.3 *Overview of Raman spectroscopy in graphene and MoS₂ transition metal dichalcogenide* 24

3 Experimental Methodology 31

3.1 *Sample preparation* 31

3.2 *The Raman spectrometer* 35

3.3 *Enhancement factor due to optical interference in the SiO₂ layer* 38

3.4	<i>Resonant Raman behavior of silicon</i>	43
4	Symmetry-dependent exciton-phonon coupling in 2D and bulk MoS₂ observed by resonance Raman scattering	45
4.1	<i>Introduction</i>	45
4.2	<i>The first-order Raman modes in MoS₂: the exciton-phonon coupling</i>	48
4.3	<i>Conclusion</i>	57
5	Intervalley scattering by acoustic phonons in 2D MoS₂ revealed by double-resonance Raman spectroscopy	58
5.1	<i>Introduction</i>	58
5.2	<i>Experimental analysis</i>	60
5.3	<i>Theoretical model</i>	64
5.4	<i>Assignment of the second-order Raman features of MoS₂</i>	71
5.5	<i>Disorder-induced DRR bands</i>	75
5.6	<i>Excitonic effects</i>	77
5.7	<i>Conclusion</i>	81
6	Conclusion and Prospect	83
A	Angle dependence of MoS₂	85
B	Ultrasensitive molecular sensor using N-doped graphene through enhanced Raman scattering	89
C	Optical identification of sulfur vacancies: Bound excitons at the edges of monolayer tungsten disulfide	109
	References	128

LIST OF TABLES

- 3.1 **Laser sources of the Raman laboratory.** List of laser sources equipping the two spectrometers of the Raman Laboratory. The excitation wavelength of the 899-01 Dye Ring laser depends on the type of dye used. 35
- B.1 **Ultrasensitive molecular sensor.** Comparison of the performance of different graphene samples as GERS substrates for molecular sensing. R6G, rhodamine 6G; PPP, protoporphyrin; CuPc, copper phthalocyanine. 101
- B.2 **Comparison of the calculated HOMO-LUMO gap.** Calculated HOMO-LUMO gap, adsorption data and resonant Raman laser energy for each molecule in electron volts. ΔG and E_L stands for HOMO-LUMO gap and laser energy, respectively. . 103

LIST OF FIGURES

1.1	Structural polytypes of pristine TMD layers. Chalcogen atoms are shown	4
1.2	The phonon and electronic dispersion of MoS₂. (a) Phonon dispersion	5
1.3	The MoS₂'s absorption spectra and exciton wave function. (a) Absorption	8
2.1	Schematics of the Raman spectrum. The Rayleigh, Stokes and anti-Stokes	15
2.2	Explanation of the usage of Feynman diagrams. (Right-side) Feynman	18
2.3	All six Feynman diagrams contributions for one-phonon Stokes process. Feynman	22
2.4	Raman spectra comparison of graphene and TMDs. Raman spectra of	25
2.5	The Double-resonance Raman spectra. Dependence of the double-resonance	29
3.1	The Scotch-tape method. (a-c) mechanical exfoliation method used for	32
3.2	The CVD method. (a) Schematics showing the experimental set-up	33
3.3	Basic set-up of a Raman spectrometer. Schematic view of a (a) monochromator and	37
3.4	Optical interference. (a) Schematic diagram of the multiple reflections interference	39
3.5	Raman cross section of silicon. Raman scattering cross section of first-order	44

4.1	Exfoliated 1L-, 2L- 3L-MoS₂ and bulk samples studied in this thesis. (a–c) Optical	48
4.2	Resonance Raman spectra of MoS₂. Raman spectra of MoS ₂ samples	49
4.3	The Raman excitation profile. Raman excitation profiles of the E _{2g} ¹	50
4.4	Extracted phonon and finite lifetime of the exciton-phonon coupling in MoS₂. (a) Energies	53
4.5	Intensity ratio of the first-order modes. (a) Ratio of the intensities of the A _{1g} and E _{2g} ¹	55
5.1	Resonance Raman results on 1L and bulk MoS₂. (a) and (b) Raman spectra of	61
5.2	Dispersive behavior of the second-order features on 1L and bulk MoS₂. (a) and (b) Laser	63
5.3	Double-resonance Raman model. (a) Representation of a DRR process where	66
5.4	Alternative representations of the DRR process. Others customary	67
5.5	Diagram of possible wave vector in intervalley scattering. (a) The top diagram	69
5.6	Calculated resonance Raman spectra. Calculated second-order Raman for	70
5.7	Resonance Raman on defective 1L MoS₂. (a) Raman spectra of defective 1L MoS ₂	76
5.8	Intervalley scattering as modelled using single-particle and excitonic band structures. (a) In single	78
A.1	Polarized Raman spectra. Raman spectra of bulk MoS ₂ sample with different	86

B.1	HRTEM and STM images of as-transferred NG. (A and B)	
	HRTEM images	92
B.2	NG sheets typical Raman spectra with different synthesis conditions. (A) Raman spectra	94
B.3	Enhancement factor efficiency of the N-doped graphene. Enhancement factors for	96
B.4	Raman mapping of PG and NG. Raman mapping of the intensity ratio	97
B.5	Resonant Raman scattering effect on NG sheets probed for different dye molecules. Excitation	98
B.6	Comparison of the enhanced Raman scattering effect between NG and PG sheets when probing RhB with different concentrations. Raman signals	100
B.7	DOS of the clusters representing the adsorbed organic dyes on PG and NG. DOS for	104
B.8	Simulated Raman spectra of the dye molecules. (A) Simulated configuration	106
C.1	Bound excitons at the edges. (A) Atomic structure of monolayer 1H-WS₂	112
C.2	Identification of sulfur vacancies. (A) Optical image of transferred WS₂	115
C.3	Evolution of PL spectra with laser power density. (A) interior area and	116
C.4	Dependence of PL spectra with temperature. (A) PL intensity map of neutral	117
C.5	Temperature-dependent PL for the interior and edge regions. PL intensity map	119
C.6	First-principles calculations of mono-sulfur vacancy. (A) Band structure of	121

- C.7 Band structure of a 5×5 WS_2 supercell with an N_2 or O_2 molecule adsorbed on the surface at a sulfur vacancy site. The bands with red or blue circles 125**
- C.8 Band structure of a WS_3 vacancy within a 5×5 supercell. (A) The red component of 126**

LIST OF PUBLICATIONS

PUBLICATIONS COVERED IN THIS THESIS

1. **CARVALHO, BRUNO R.**; Malard, Leandro M.; Alves, Juliana M.; Fantini, Cristiano; Pimenta, Marcos A.; Symmetry-Dependent Exciton-Phonon Coupling in 2D and Bulk MoS₂ Observed by Resonance Raman Scattering, **PHYSICAL REVIEW LETTERS** 114 (13), 136403 (2015)–Erratum: 2016. **PHYSICAL REVIEW LETTERS** 116:089904.
2. **CARVALHO, BRUNO R.**^ξ; Wang, Yuanxi^ξ; Mignuzzi, Sandro; Roy, Debudulal; Terrones, Mauricio; Fantini, Cristiano; Crespi, Vincent H.; Malard, Leandro M.; Pimenta, Marcos A.; Intervalley scattering by acoustic phonons in two-dimensional MoS₂ revealed by double-resonance Raman spectroscopy, **NATURE COMMUNICATIONS** 8, 14670 (2017).
3. Pimenta, Marcos A.; del Corro, Elena; **CARVALHO, BRUNO R.**; Fantini, Cristiano; Malard, Leandro M.; Comparative Study of Raman Spectroscopy in Graphene and MoS₂-type Transition Metal Dichalcogenides, **ACCOUNTS OF CHEMICAL RESEARCH** 48 (1), 41-47 (2015).
4. Feng, Simin^ξ; dos Santos, Maria C.^ξ; **CARVALHO, BRUNO R.**^ξ; Lv, Ruitao; Li, Qing; Fujisawa, Kazunori; Elías, Ana Laura; Perea-López, Nestor; Endo, Morinobu; Pan, Minghu; Pimenta, Marcos A.; Terrones, Mauricio; Ultrasensitive molecular sensor using N-doped graphene through enhanced Raman scattering, **SCIENCE ADVANCES** 2 (7), E1600322 (2016). This work has been highlighted in numerous news sites including **Penn State News** ([LINK](#)), **Phys.org** ([LINK](#)), **ScienceDaily** ([LINK](#)), **(e) Science News** ([LINK](#)) and **AZO Nano** ([LINK](#)).
5. Carozo, Victor; Wang, Yuanxi; Fujisawa, Kazunori; **CARVALHO, BRUNO R.**; McCreary, Amber; Feng, Simin; Lin, Zhong; Zhou, Chanjing;

Perea-Lopez, Nestor; Elias, Ana Laura; Kabius, Bernd; Crespi, Vincent H.; Terrones, Mauricio; Optical identification of sulfur vacancies: Bound excitons at the edges of monolayer tungsten disulfide, *SCIENCE ADVANCES* 3 (4), E1602813 (2017).

PUBLICATIONS *not* COVERED IN THIS THESIS

6. **CARVALHO, BRUNO R.**; Hao, Yufeng; Righi, Ariete; Rodriguez-Nieva, Joaquin F.; Colombo, Luigi; Ruoff, Rodney S.; Pimenta, Marcos A.; Fantini, Cristiano; Probing carbon isotope effects on the Raman spectra of graphene with different ^{13}C concentrations, *PHYSICAL REVIEW B* 92 (12), 125406 (2015).
7. Lin, Zhong; **CARVALHO, BRUNO R.**; Kahn, Ethan; Lv, Ruitao; Rao, Rahul; Terrones, Humberto; Pimenta, Marcos A.; Terrones, Mauricio; Defect Engineering of Two-Dimensional Transition Metal Dichalcogenides, *2D MATERIALS* 3 (2), 022002 (2016).
8. Sun, Yifan; Wang, Yuanxi; Sun, Du; **CARVALHO, BRUNO R.**; Read, Carlos G.; Lee, Chia-hui; Lin, Zhong; Fujisawa, Kazunori; Robinson, Joshua A.; Crespi, Vincent H.; Terrones, Mauricio; Schaak, Raymond E.; Low-Temperature Solution Synthesis of Few-Layer 1T'-MoTe₂ Nanostructures Exhibiting Lattice Compression, *ANGEWANDTE CHEMIE INTERNATIONAL EDITION* 55 (8), 2830 (2016).
9. Mania, Edrian; Alencar, Ananias B.; Cadore, Alisson R.; **CARVALHO, BRUNO R.**; Watanabe, Kenji; Taniguchi, Takashi; Neves, Bernardo R. A.; Chacham, Helio; Campos, Leonardo C.; Spontaneous Doping on High Quality talc-graphene-hBN Van der Waals Heterostructures, **SUBMITTED**.

^ξ These authors contributed equally to the work.

RESUMO

Esta tese apresenta um estudo de espalhamento Raman ressonante com diferentes energias de laser de excitação em únicas e poucas camadas de MoS₂, tendo como objetivo compreender a dinâmica de interação entre éxcitons e fônons e a origem dos modos Raman de segunda ordem neste material, ao qual pode ser aplicado a outros sistemas semicondutores semelhantes. Na investigação do perfil de excitação Raman, envolvendo os modos Raman de primeira ordem do MoS₂ (bandas E_{2g}¹ e A_{1g}), demonstra-se que o perfil do modo A_{1g} é intensificado quando a energia de laser de excitação encontra-se em ressonância com os éxcitons A, B e C do MoS₂, enquanto o perfil do modo E_{2g}¹ é intensificado apenas quando a energia de laser de excitação coincide-se com a energia do éxciton C. Tal perfil de ressonância é devido a interação dos orbitais dos éxcitons e fônons. No estudo dos modos de segunda ordem, a espectroscopia Raman ressonante é usada em conjunto com a teoria do funcional da densidade para explicação do processo de dupla-ressonância em única camada de MoS₂ e *bulk*. Nossos resultados mostram que a frequência Raman destes modos desviam-se quando se muda a energia de excitação do laser e, cálculos de primeiros princípios confirmam que isso é ocasionado por fônons acústicos distintos, conectando diferentes estados de vale dentro da primeira zona de Brillouin. Além disso, observa-se que o processo Raman de dupla-ressonância é afetado pela transição *bandgap* indireto para direto e, uma comparação detalhada dos resultados em monocamada e *bulk* permitem a atribuição de cada modo Raman com o respectivo fônon em torno dos pontos **M** ou **K** na zona de Brillouin. Estes resultados destacam o espalhamento entre-vales dos elétrons pelos fônons acústicos em sistemas semicondutores bidimensionais da família dos dicalcogênitos de metais de transição, o qual é essencial para a despolarização de vales em MoS₂.

ABSTRACT

This thesis presents a multiple energy excitation resonant Raman study on mono- and few-layered MoS₂. Our aim is to obtain the understanding of their exciton and phonon dynamics and the origin of the second-order features, as well as their potential to the understanding other semiconducting transition metal dichalcogenide materials. In our investigation of the Raman excitation profile of the two most pronounced features of the Raman scattering spectrum of MoS₂ (E_{2g}^1 and A_{1g} bands). We demonstrate that the A_{1g} feature is enhanced when the excitation laser is in resonance with the A, B and C excitons of MoS₂, while the E_{2g}^1 feature is shown to be enhanced only when the excitation laser matches the C exciton energy. We analyze the exciton-phonon interaction and show that the excitons' orbital and the phonons are the responsible for the enhancement behavior of both modes. In the study of the second-order modes, Raman spectroscopy in conjunction with density functional theory calculations unveil the double-resonance Raman scattering process in monolayer and bulk MoS₂. Our findings show that the frequency of some Raman features shifts when changing the excitation energy and, first-principle simulations confirm that such bands arise from distinct acoustic phonons, connecting different valley states. The double-resonance Raman process is affected by the indirect-to-direct bandgap transition, and a detailed comparison of results in monolayer and bulk allow the assignment of each Raman feature to specific phonons near the **M** or **K** points of the Brillouin zone. These findings highlight the underlying physics of intervalley scattering of electrons by acoustic phonons in semiconducting two dimensional transition metal, which is essential for valley depolarization in MoS₂.

WELCOME TO THE FLATLAND

“True” said the Sphere “it appears to you a plane because you are not accustomed to light and shade and perspective just as in flatland a hexagon would appear a straight line to one who has not the art of sight recognition but in reality it is a solid as you shall learn by the sense of feeling”

— EDWIN A. ABBOTT (1884)

Above is a quote from the book *“Flatland: A romance of many dimensions”* which illustrates the bidimensional world. This sentence might not have been shocking in the 19th century, but now all that we heard is about the flatland. So, why all the fuss now and not centuries ago? All start in a mere pencil trace. A pencil is made of graphite, which is composed of several atomically thin carbon sheets stacked onto each other, but that is not all. The interaction between these carbon sheets is weak, making easy to separate them by just rubbing the graphite on a solid surface until an only one-atom-thick sheet of carbon atoms remain. It is like “tracing a pencil on a white piece of paper”. By doing this, everything becomes smaller, and all its properties change so wonderfully, that we still are trying to understand it. This single one-atom-thick sheet of carbon atoms is the so-called graphene or, as some people say, the wonderful material.

The graphene has a high charge carrier mobility, and it is harder than steel but still flexible as a feather. This flexibility leads to the advance of emerging technologies such as rollerball computers and flexible phones. By now, the importance of graphene is evident, but it is still not over. After the graphene’s discovery, other types of two-dimensional materials have emerged, and each one has its physical properties. We can say that we have only seen the tip of the iceberg and, more materials with unusual properties are to be discovered and will revolutionize the world we live in.

Welcome to the flatland!

1 INTRODUCTION AND BACKGROUND

1.1 Introduction

The isolation of graphene by mechanical cleavage in 2004 (Novoselov et al., 2004) sparked research on two-dimensional (2D) materials that has been growing at a tremendous rate. The possibility of controlled production of different types of 2D systems with a good crystal quality has opened up many exciting routes for the study of the fundamental physics in these systems. The key factor behind all this relatively young field is the mechanical exfoliation of bulk crystals that allowed the preparation of several types of 2D materials (Novoselov et al., 2005). By just a piece of bulk crystal, a roll of tape and an optical microscope several types of 2D atomically thin layers can be isolated and, their physics properties vary from insulators to superconductors depending on their electronic structure. Researchers have realized that by tuning the number of atomic layers of any layered material, it is possible to achieve unusual properties, including the enhancement of quantum confinement and the reduction in dielectric screening, both of which enhance interactions between charged particles in the material.

One family of these 2D systems is the transition-metal dichalcogenides (TMDs). Unlike graphene's single carbon atomic-thick layer, TMDs (*e.g.* MoS₂, WS₂, WSe₂, etc.) are formed by an atomic trilayer which consists of two adjacent layers of chalcogen atoms (X) covalently bonded to a layer of transition metal atoms (M) forming an X – M – X layer configuration (see Figure 1.1). The electronic structure of these compounds depends on the transition metal species. The TMDs composed of a metal from groups IV and VI are semiconductors or insulators, and those composed of a metal from group V atoms are metallic (Wilson and Yoffe, 1969). Although the bulk form of TMDs has been extensively studied in the past (Wilson and

Yoffe, 1969), only recently monolayer and few-layer TMDs were obtained. In the case of semiconducting TMDs, such as MoS_2 , WS_2 , WSe_2 , etc. they show a transition from an indirect band gap in the bulk to a direct gap for a monolayer (Mak et al., 2010; Splendiani et al., 2010). This fact together with the rich physics of strong spin-orbit coupling in these materials has opened up several opportunities in both basic research and optoelectronic applications (Xu et al., 2014).

Two possible structural polytypes have been reported for a monolayer MX_2 : the semiconducting trigonal prismatic phase (the notation 1H is adopted for monolayers; see Figure 1.1(a)); the 2H phase refers to few-layers and bulk crystals), and the metallic octahedral prismatic phase (the 1T phase; see Figure 1.1(b)) (Wilson and Yoffe, 1969). In certain cases, the 1T phase is not thermodynamically stable, and its structurally distorted derivative, denominated as 1T' can be observed instead (see Figure 1.1(c)). When TMD crystals have more than one atomic chalcogen-metal-chalcogen ($X - M - X$) layer of the 1H phase bonded by van der Waals (vdW) forces, additional polytypes appear in account for variations in stacking orders. A Bernal stacking (AbA BaB) yields the 2H phase (see Figure 1.1(d)), while an AbA CaC BcB stacking yields a rhombohedral phase denominated as the 3R phase (see Figure 1.1(e)). All above structural polytypes have attracted considerable attention and have found themselves suitable for certain applications (Voiry et al., 2015). This thesis does not attempt to cover all those polytypes. We focus primarily on the semiconducting 1H and 2H phases, more specifically the MoS_2 -type transition metal dichalcogenide.

In the following, the most relevant properties of 2D MoS_2 semiconductor will be introduced, highlighting the aspects that make it especially attractive.

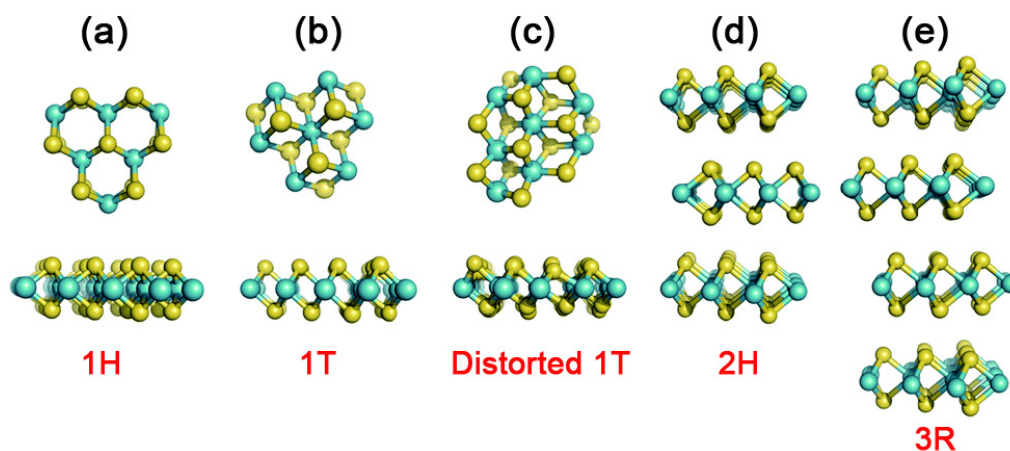


Figure 1.1: **Structural polytypes of pristine TMD layers.** Chalcogen atoms are shown in yellow, and transition metal atoms are shown in blue. (a) The 1H phase, (b) the 1T phase, (c) the distorted 1T, or 1T' phase, (d) the 2H phase, (e) the 3R phase. Taken and adapted from (Lin et al., 2016; Voiry et al., 2015).

1.2 Raman active-modes in transition metal dichalcogenides

Group theory is a well-known method to analyze the lattice dynamics of crystals. Information about properties of a crystal (and its atomic structure) such as symmetry, degeneracy and Raman activity of the normal modes of vibration can be obtained from group theory (Tinkham, 1992). Figure 1.2(a) shows the phonon dispersion relations of monolayer MoS_2 . The symmetries of the zone-center and Raman active modes are represented (Molina-Sánchez and Wirtz, 2011). A single layer of 1H- MX_2 has three zone-center first-order Raman active modes belonging to the A'_1 , E' and E'' irreducible representations of the D_{3h} group. For the A'_1 mode, the metal atoms do not move and the chalcogen X atoms vibrate in the out-of-plane direction with the X atoms of the upper layer vibrating in-phase and against the lower layer of X atoms, as shown in Figure 1.2(b). In the

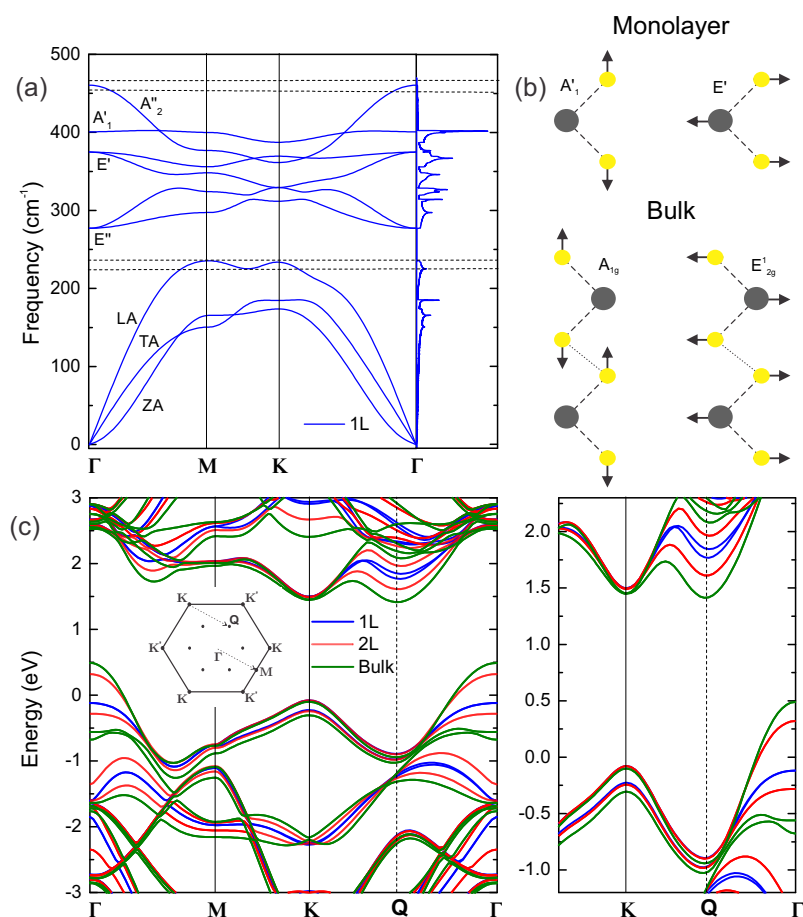


Figure 1.2: **The phonon and electronic dispersion of MoS₂.** (a) Phonon dispersion relations of monolayer MoS₂. (b) Atomic displacements in two Raman active modes of monolayer and bulk TMDs. (c) Electronic structure of MoS₂. Adapted from (Carvalho et al., 2017; Pimenta et al., 2015).

case of the E' and E'' modes, the atomic displacements are in-plane. For the E' mode, all X atoms move in-phase, and all M atoms move in-phase and in opposite directions. This mode, also shown in Figure 1.2(b), is somewhat similar to the graphene Raman active mode (G band), where the A carbon atom sublattice vibrates against the B atom sublattice. For

the E'' mode, the non-null elements of the Raman tensor correspond to the quadratic functions xz and yz . Therefore, this mode does not appear in the commonly used Raman backscattering configuration where the direction of the laser beam is perpendicular to the layer xy -plane. Therefore, the Raman spectra of 1H-MX₂ in this special back-scattering configuration exhibit only two first-order Raman modes, with A'_1 and E' symmetries (Pimenta et al., 2015; Terrones et al., 2014; Ribeiro-Soares et al., 2014).

For bulk 2H-MX₂, there are four Raman active modes, which are assigned according to the representations of the D_{6h} group as A_{1g} , E_{1g} , E_{2g}^1 and E_{2g}^2 . The A_{1g} , E_{1g} and E_{2g}^1 modes correspond, respectively, to the A'_1 , E'' and E' modes of monolayer MX₂, where the atoms in adjacent layers move in-phase in respect to inversion symmetry. The E_{2g}^2 mode correspond to the vibration of adjacent rigid-layers with respect to each other, similar to the rigid-layer mode of graphite, and also appear at very low frequencies. Therefore, the Raman spectra of 1H- and 2H-MX₂ crystals using conventional spectrometers and in a backscattering configuration discussed above, also exhibit only two first-order Raman peaks, with A_{1g} symmetry (out-of-plane atomic displacements) and E_{2g}^1 symmetry (in-plane displacements) (Sekine et al., 1980a,b).

1.3 The optical property in transition metal dichalcogenides

The electronic band structure of TMDs materials depends on the transition metal and chalcogen species, thickness and stacking sequence of each layer (Zhao et al., 2015; Pimenta et al., 2015). The band structure of MoS₂, and other TMD materials, such as WS₂, WSe₂ and MoSe₂ presents a distinct behavior from that of graphene which exhibits linear dispersion at low energies (Pimenta et al., 2015). Single layer TMDs has an interband transition at the \mathbf{K} and \mathbf{K}' points of the Brillouin zone (BZ), where a strong

spin-orbit coupling splits the valence band into two sub-bands and give rise to two peaks in the optical absorption spectra identified as A and B (Mak et al., 2010; Splendiani et al., 2010). Different from few-layers and bulk TMDs, single layers present distinct physical properties. For example, Figure 1.2(c) shows the calculated electronic band structure by density functional theory of monolayer, bilayer and bulk MoS₂. Notice that as the number of layer increases, a conduction band state midway along $\overline{K\Gamma}$, labeled **Q**, drops in energy and aligns with the conduction band minimum at the **K** point. Thus, monolayer MoS₂ is a direct bandgap semiconductor, in contrast to the indirect bandgap of the bilayer and bulk MoS₂. This indirect-to-direct bandgap transition was confirmed by photoluminescence (PL) experiments, where the authors observed a shift of the indirect PL peak with the number of layers and an enhancement of the PL signal in monolayer compared to the few-layers and bulk (Mak et al., 2010; Splendiani et al., 2010).

1.4 Excitons in MoS₂

From solid state physics, we know that a usual 2D semiconductor has a parabolic energy dispersion for electron and holes, and its joint density of state near the bandgap is a step function (Yu and Cardona, 2010; Klingshirn, 2012). However, as shown in Figure 1.3(a)–(d), the measured absorption spectra of the monolayer MoS₂ (and other TMDs systems) present peak features at the band edge that are known as excitons. An exciton is a hydrogen-like complex comprising a bounded electron-hole pair, formed by the Coulomb attraction between the two oppositely charged quasi-particles. Therefore, the two peaks in Figure 1.3, commonly called as A and B excitons, are due to a strong excitonic effect in these materials.

The separation of A and B excitons come from the spin-orbit splitting of the top of the valence band at the **K** point from $d_{x^2-y^2}$ and d_{xy} states to

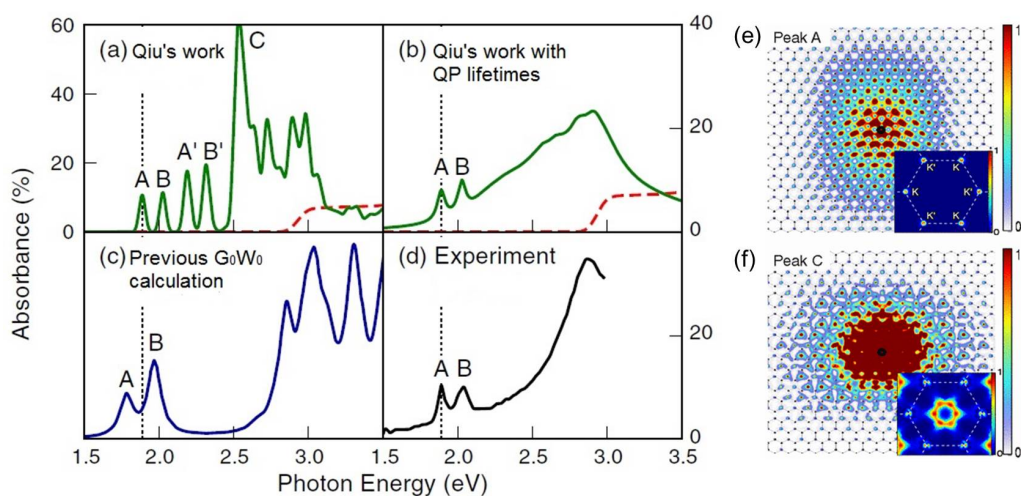


Figure 1.3: The MoS_2 's absorption spectra and exciton wave function. (a) Absorption spectra of MoS_2 without (dashed red curve) and with (solid green curve) electron-hole interactions. (b) Same calculated data as (a), but using an *ab initio* broadening based on the electron-phonon interactions. (c) Previous G_0W_0 calculation (in arbitrary units). Note that the region between 2.2–2.8 eV is completely flat. (d) Experimental absorbance. (e) Exciton corresponding to peak A in real space and in k space (inset). The real-space plot is the modulus squared of the exciton wave function projected onto the plane with the hole (black circle) fixed near a Mo atom. Mo atoms are purple squares, and sulfur atoms are green triangles. (f) Real-space and k -space (inset) modulus squared of excitons forming peak C. Adapted from (Qiu et al., 2013).

d_{z^2} type states (Kozawa et al., 2014; Qiu et al., 2013). In addition, Qiu et al. also predicted that the spectral region near 2–2.8 eV is not featureless but contains many bright and dark excitonic states that are broadened by electron-phonon interactions [Figure 1.3(a)] (Qiu et al., 2013). The authors predicted the existence of a third set of excitonic states that hybridizes with the excitons forming peak C (Qiu et al., 2013). Figure 1.3(b) includes a broadening due to the quasi-particle lifetimes, in which are approximated from the electron-phonon scattering rates at room-temperature. Thus,

the spectrum's broadening in Figure 1.3(b) roughly approximates to the room-temperature case. The position of peak C appears to change because different scattering rates at different energies modify the weight in different parts of the spectrum. However, the excitation energies remain the same when compared with the experimental, as shown in Figures 1.3(b) and 1.3(d). In addition, Figure 1.3(b) does not include all temperature effects, such as thermal expansion of the lattice and renormalization of the quasi-particle band structure occasioned by the real part of the electron-phonon self-energy (Qiu et al., 2013). Therefore, the purpose of this figure is to demonstrate that the energy-dependent scattering rates will smear out higher energy peaks into one large peak, while peaks A and B remain distinct.

In order to unveil which exciton reflects the peaks A and C, Qiu et al. have calculated the modulus squared of the real-space exciton and \mathbf{k} -space of these peaks, as shown in Figure 1.3(e) and 1.3(f) (Qiu et al., 2013). Figure 1.3(e) shows the exciton associated to the peak A in the real space and \mathbf{k} -space (see inset). In the aforementioned work, the authors have considered the hole fixed near the Mo atom (Qiu et al., 2013). In the \mathbf{k} -space of the exciton, we notice that the peak A is originated by two energetically degenerate excitons due to free electron-hole transitions at the \mathbf{K} and \mathbf{K}' points [see Figure 1.3(e) inset]. And with the exciton wave function analogous in the real-space [see Figure 1.3(e)] (Qiu et al., 2013). Thus, the character of the exciton that gives rise to the peak A reflects the Mo dz^2 orbitals of the states in the lowest MoS₂ conduction band (Qiu et al., 2013). This result also applies to peak B since the spinor wave functions of the spin-orbit split are similar at the \mathbf{K} and \mathbf{K}' points (Qiu et al., 2013).

Now, let us take a look at the exciton associated to the peak C. From Figure 1.3(f), we observe a six nearly degenerate exciton states which are formed by transitions between the highest valence band and the first three lowest conduction bands near (but not at) the Γ point. These states reflect

the lowest transitions are degenerate at several points around the Γ point (Qiu et al., 2013). Also, by summing up the modulus squared in \mathbf{k} -space of these exciton states, it results in a ring with six-fold symmetry around the Γ point having a small contribution from near \mathbf{K} and \mathbf{K}' points [see Figure 1.3(f) inset] (Qiu et al., 2013). These six exciton states are from where the peak C comes from. Here, the authors have fixed the hole (in real-space) near the Mo atom with the character of the electron having a contribution from both Mo dz^2 and S p_x and p_y , with more S character around the hole (Qiu et al., 2013). In chapter 4, we will see that these excitons' character play an important role in the exciton-phonon coupling dynamics.

1.5 Outline of the Thesis

In this thesis, we study the dynamics of electron, phonon and their interplay in MoS_2 via resonant Raman spectroscopy. To achieve this, the thesis is organized as follows:

CHAPTER 2, A brief outline of the basics concepts of the Raman scattering theory is briefly discussed.

CHAPTER 3, We discuss the experimental methodology employed in this thesis, in particular, sample preparation and Raman spectroscopy setup.

CHAPTER 4, We discuss in detail meaningful results of the exciton-phonon coupling in MoS_2 .

CHAPTER 5, We exploit the concept of double-resonant Raman scattering in MoS_2 of the acoustic phonons.

CHAPTER 6, We discuss the prospects of the thesis and future works.

In the end, we close this thesis with two appendices highlighting some works developed during the doctoral internship at Pennsylvania State University.

2 BASIC CONCEPTS ON RAMAN SCATTERING THEORY

In this chapter, a brief and simpler description of the Raman scattering theory is discussed. We start with the discussion of the classical followed by the quantum mechanical formalism. A brief literature discussion of Raman spectra in MoS₂ is also presented.

2.1 The macroscopic theory of Raman scattering

When the light interacts with a medium different processes, such as transmission and reflection, can occur but a small fraction of the incoming light is scattered because of the inhomogeneities inside the medium. These scattering processes can be either elastic (where there is no change of wavelength) or inelastic occasioned by the atomic vibrations producing changes in the wavelength. The Raman spectroscopy is the technique used to study the inelastic scattering of the light from a medium, produced by the interaction of the light with same excitation (Yu and Cardona, 2010; Martin and Falicov, 1983). What we measure in the Raman experiment is the shift in energy between the incoming and inelastically scattered light.

The macroscopic theory of the Raman scattering explains these light-matter interactions that induce a polarization vector (Yu and Cardona, 2010). By considering an infinite crystalline medium at finite temperature with the dielectric susceptibility $\overleftrightarrow{\chi}$, which accounts for the polarizability; the induced electric dipole can be written in terms of electric field \mathbf{E} of the incident light on the medium as (Yu and Cardona, 2010; Jackson, 2006):

$$\mathbf{P} = \overleftrightarrow{\chi} \cdot \mathbf{E}, \quad (2.1)$$

where the electric field, related with the incident radiation, is written as a plane wave $\mathbf{E}(\mathbf{r}, t)$ with amplitude $\mathbf{E}_0(\mathbf{k}_i, \omega_i)$:

$$\mathbf{E}(\mathbf{r}, t) = \mathbf{E}_0(\mathbf{k}_i, \omega_i) \cos(\mathbf{k}_i \cdot \mathbf{r} - \omega_i t). \quad (2.2)$$

Here, \mathbf{k}_i and ω_i are, respectively, the wave vector and the frequency of the incident light.

The susceptibility tensor $\overleftrightarrow{\chi}$ of the medium depends on the atomic displacement $\mathbf{Q}(\mathbf{r}, t)$. As the amplitude of $\mathbf{Q}(\mathbf{r}, t)$ is smaller than the lattice constant of the medium at room temperature, the tensor $\overleftrightarrow{\chi}$ can be expanded using a Taylor series in $\mathbf{Q}(\mathbf{r}, t)$ as (Yu and Cardona, 2010),

$$\chi(\mathbf{k}_i, \omega_i, \mathbf{Q}) \approx \chi_0(\mathbf{k}_i, \omega_i) + \left(\frac{\partial \chi}{\partial \mathbf{Q}} \right) \Big|_0 \mathbf{Q}(\mathbf{r}, t) + \dots \quad (2.3)$$

The combination of the three equations yields,

$$\mathbf{P}(\mathbf{r}, t, \mathbf{Q}) \approx \mathbf{P}_0(\mathbf{r}, t) + \mathbf{P}_{\text{ind}}(\mathbf{r}, t, \mathbf{Q}) + \dots, \quad (2.4)$$

where $\mathbf{P}_0(\mathbf{r}, t)$ the polarization vector oscillating with same frequency as that of the incident radiation, giving rise to the so-called Rayleigh scattering (or elastic scattering) and, $\mathbf{P}_{\text{ind}}(\mathbf{r}, t, \mathbf{Q})$ is the polarization induced by the vibration of the atoms. In order to obtain $\mathbf{P}_{\text{ind}}(\mathbf{r}, t, \mathbf{Q})$, a plane wave will be introduced to describe the quantized atomic displacement $\mathbf{Q}(\mathbf{r}, t)$ as, referred to normal mode of vibration (Ashcroft and Mermin, 1976),

$$\mathbf{Q}(\mathbf{r}, t) = \mathbf{Q}(\mathbf{q}, \omega_0) \cos(\mathbf{q} \cdot \mathbf{r} - \omega_0 t). \quad (2.5)$$

Inserting equation (2.5) into $\mathbf{P}_{\text{ind}}(\mathbf{r}, t, \mathbf{Q})$ from equation (2.4) and rearrang-

ing the cosine terms, we find

$$\mathbf{P}_{\text{ind}}(\mathbf{r}, t, \mathbf{Q}) = \frac{1}{2} \left(\frac{\partial \chi}{\partial \mathbf{Q}} \right) \bigg|_0 \mathbf{Q}(\mathbf{q}, \omega_0) \mathbf{E}_0(\mathbf{k}_i, \omega_i) \cdot \cdot \{ \cos((\mathbf{k}_i + \mathbf{q}) \cdot \mathbf{r} - (\omega_i + \omega_0) t) + \cos((\mathbf{k}_i - \mathbf{q}) \cdot \mathbf{r} - (\omega_i - \omega_0) t) \}. \quad (2.6)$$

Thus the induced polarization is composed of two components:

- i. One with wave vector $\mathbf{k}_S = \mathbf{k}_i - \mathbf{q}$ and frequency $\omega_S = \omega_i - \omega_0$ corresponding to the called Stokes scattered light.
- ii. Other with wave vector $\mathbf{k}_{AS} = \mathbf{k}_i + \mathbf{q}$ and frequency $\omega_{AS} = \omega_i + \omega_0$ corresponding to the called anti-Stokes scattered light.

In other words, an incoming light of frequency ω_i is inelastically scattered generating the emission of two waves that appear next to the laser line. One is shifted to lower frequencies with $\mathbf{k}_i - \mathbf{q}$ and $\omega_i - \omega_0$ (Stokes process), whereas the other one is shifted to higher frequencies with $\mathbf{k}_i + \mathbf{q}$ and $\omega_i + \omega_0$ (anti-Stokes process). This process is illustrated in Figure 2.1.

Notice that in every process both momentum and energy must be conserved. As a result, it imposes a condition for the back-scattering process of one-phonon, that the wave vector of the phonon needs to be smaller than twice the photon wave vector. Thus, the wave vector associated with the incoming light and the inelastically scattered light (on the order of $2\pi/\lambda$, where λ is either the wavelength of the incoming light or the scattered light) must be much smaller than the wave vector at the border of the Brillouin zone (on the order of $2\pi/a$, where a is the crystal lattice parameter). For instance, an incoming light in the visible range (*e.g.* 500 nm) has a wave vector in the order of 10^7 m^{-1} , whereas the wave vector of a crystal, within the dimensions of the first Brillouin zone, in the order of 10^{10} m^{-1} (*e.g.* the lattice parameter a of MoS₂ crystal is around 3.16 Å (Molina-Sánchez and

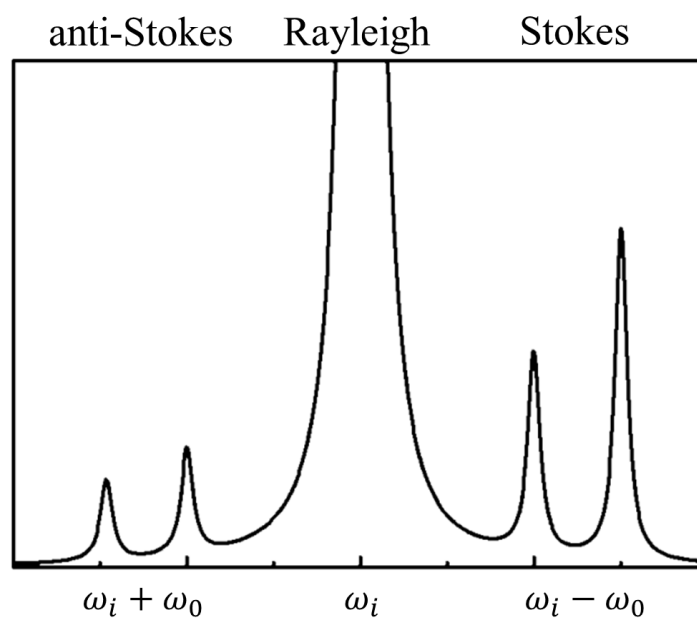


Figure 2.1: **Schematics of the Raman spectrum.** The Rayleigh, Stokes and anti-Stokes spectra; where $\hbar\omega_i$ is the incoming light energy and the $\hbar\omega_0$ is the phonon energy. Adapted from (Jorio et al., 2011).

Wirtz, 2011)). Therefore, the condition $\mathbf{k}_{AS/S} = \mathbf{k}_i \pm \mathbf{q}$ confines phonons to the center of the Brillouin zone around the Γ point. In other words, the wave vector of the phonon is limited to be $\mathbf{q} \sim 0$, which are called as first-order Raman modes. This is the fundamental selection rule of the Raman process.

Now by taking equation (2.6) and neglecting the cosine terms we have,

$$\begin{aligned}
\mathbf{P}_{\text{ind}}(\mathbf{r}, t, \mathbf{Q}) &\propto \left(\frac{\partial \chi}{\partial \mathbf{Q}} \right) \mathbf{Q}(\mathbf{q}, \omega_0) \mathbf{E}_0(\mathbf{k}_i, \omega_i) \\
&= \left(\frac{\partial \chi_{ij}}{\partial Q_l} \right) Q_l(\mathbf{q}, \omega_0) \mathbf{E}_0(\mathbf{k}_i, \omega_i) \\
&= (\chi_{ij,l}) Q_l \cdot (\mathbf{E}_0)_j \\
&= \mathbf{R}_{ij}^l \cdot \mathbf{E}_{0j} \\
&= \overleftrightarrow{\mathbf{R}} \mathbf{E}_0.
\end{aligned} \tag{2.7}$$

Equation (2.7) demonstrates that a polarization is induced when the susceptibility does not vanish for displacements along the direction of the incident wave. Similarly, the scattered wave, $\mathbf{E}_s \cdot \mathbf{P}_{\text{ind}}$ also requires to have non-vanishing components. Thus, the intensity of the Raman scattered light can be written as,

$$I_s \propto \sum_n \left| \mathbf{E}_s \cdot \overleftrightarrow{\mathbf{R}}_n \cdot \mathbf{E}_0 \right|^2. \tag{2.8}$$

Here $\overleftrightarrow{\mathbf{R}}_n$ is the Raman tensor. Equation (2.8) indicates us that only specific polarization combinations ($\mathbf{E}_0; \mathbf{E}_s$) contribute to the Raman intensity, resulting in non-zero vector product in the intensity of the Raman scattered light.

We stress that the Raman tensor $\overleftrightarrow{\mathbf{R}}_n$ depends on the symmetry of the crystal structure under study (cf. equation (2.7)) and, the non-zero elements of the Raman tensor are obtained using group theory and the symmetry characteristic of the normal mode of vibration of the crystal. Therefore, the n -index in equation (2.8) refers to the irreducible representation of the crystal. All phonons are represented by its irreducible representation $\overleftrightarrow{\mathbf{R}}_n$ and, the total Raman intensity is obtained by summing over all phonons (see Appendix A). In appendix A, we have used

the equation above to obtain the Raman intensity behavior of the Γ center phonons in bulk MoS₂.

2.2 The microscopic theory of Raman scattering

The classical formalism of the Raman theory discussed in the previous section only describes the photon-phonon interaction which is weaker than the electron-phonon interaction. For a further elucidation, it is needed to consider the quantum mechanical formalism. The Hamiltonian of a light-matter interaction can be written as (Yu and Cardona, 2010),

$$\mathcal{H} = \overbrace{\mathcal{H}_e + \mathcal{H}_l + \mathcal{H}_R}^{\mathcal{H}_0} + \overbrace{\mathcal{H}_{eR} + \mathcal{H}_{eL}}^{\mathcal{H}_1} \quad (2.9)$$

Here $\mathcal{H}_0 = \mathcal{H}_e + \mathcal{H}_l + \mathcal{H}_R$ corresponds to the unperturbed Hamiltonian, where \mathcal{H}_e , \mathcal{H}_l and \mathcal{H}_R are the Hamiltonian from the electron, lattice vibrations and incoming radiation and $\mathcal{H}_1 = \mathcal{H}_{eR} + \mathcal{H}_{eL}$ corresponds to the Hamiltonian of the perturbation, where \mathcal{H}_{eR} is the Hamiltonian of the electron interacting with incoming radiation and, \mathcal{H}_{eL} is the Hamiltonian that describes the interaction involving the lattice of the crystal, *i.e.* the electron-phonon interaction Hamiltonian.

In other words, the microscopic theory involving one-phonon Raman scattering can be described in the following steps:

- i. An incoming photon is absorbed by the medium creating an electron-hole pair (given by \mathcal{H}_{eR});
- ii. The electron-hole pair is inelastically scattered to another state by emitting (Stokes process) or annihilating (anti-Stokes process) a phonon (given by \mathcal{H}_{eL});

- iii. The electron-hole pair recombines radiatively back to the ground state by emitting a photon (given by \mathcal{H}_{eR});

Here, the electron acts only as an intermediate state and all electronic transitions are virtual ¹ with the initial and final electronic states are taken to be the ground state.

Feynman diagrams

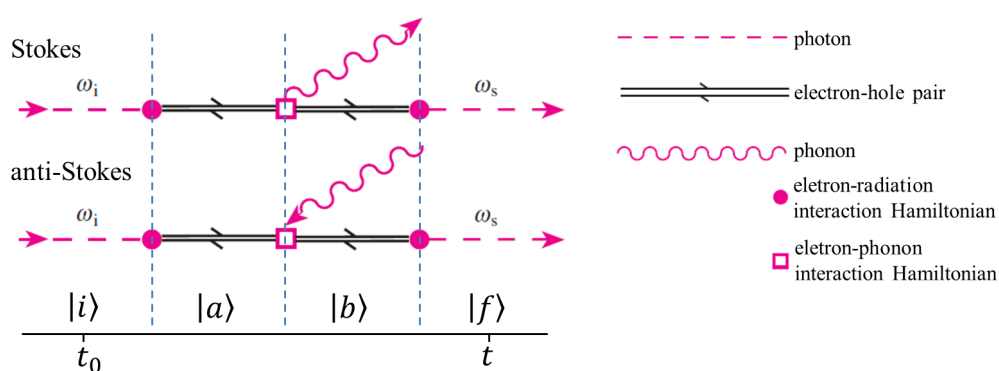


Figure 2.2: **Explanation of the usage of Feynman diagrams.** (Right-side) Feynman diagrams for one-phonon Stokes and anti-Stokes scattering. (Left-side) explanation of the symbols used in drawing Feynman diagrams to represent the Raman scattering. Adapted from (Yu and Cardona, 2010).

In order to describe the microscopic formalism of the Raman scattering, the Feynman diagrams depicted in Figure 2.2 related to both Stokes and anti-Stokes processes are presented. Before the description of these scattering paths, it is important to comment the rules for drawing Feynman diagrams (Yu and Cardona, 2010):

¹It is important to comment here that the virtual states are conserved because it occurs in a finite time.

- Excitations such as photons, phonons and electron-hole pairs are drawn by lines. They are called **propagators** and, are labeled according to the properties of the excitations like their wave vectors, frequencies, and polarizations.
- Interactions between two excitations are represented by intersections of their propagators. They are called **vertices** and, are usually highlighted by a symbol like filled circle or an empty square which specifies the type of the interaction.
- Propagators have an arrow indicating whether their excitations are created or annihilated in an interaction. An arrow pointing towards a vertex means annihilation and an arrow pointing away from a vertex means creation.
- The sequence of the interactions taking place is from left to right.
- Once a diagram of a process has been drawn, other equivalent processes can be derived by permuting the time order of the initial process.

Therefore, considering only the Stokes scattering process from Figure 2.2, the Feynman diagram can be described as follows: The first vertex represents how the incident state $|i\rangle$ interacts with an incoming photon of energy $E_i = \hbar\omega_i$ and creates an electron-hole pair sending the system to the state $|a\rangle$ via \mathcal{H}_{eR} . In the second vertex, this electron-hole pair is scattered via \mathcal{H}_{eL} creating a phonon of energy $\hbar\omega_{ph}$. Then, the system goes to the state $|b\rangle$. Finally, in the third vertex, the electron-phonon recombines and emits a new photon of energy $\hbar\omega_s$ via \mathcal{H}_{eR} . Thus, the system enters the final state $|f\rangle$. Therefore, these four states and their respective energies can be written as,

$$\begin{aligned}
|i\rangle &= |n_i, 0, m, \varphi_0\rangle, E_i = n_i \hbar\omega_i + m\hbar\omega_{ph} + E_e^v \\
|a\rangle &= |n_i - 1, 0, m, \varphi_e^a\rangle, E_a = (n_i - 1) \hbar\omega_i + m\hbar\omega_{ph} + E_e^c \\
|b\rangle &= |n_i - 1, 0, m \pm 1, \varphi_e^b\rangle, E_b = (n_i - 1) \hbar\omega_i + (m \pm 1) \hbar\omega_{ph} + E_e^c \\
|f\rangle &= |n_i - 1, 1, m \pm 1, \varphi_0\rangle, E_f = (n_i - 1) \hbar\omega_i + \hbar\omega_s + (m \pm 1) \hbar\omega_{ph} + E_e^v
\end{aligned} \tag{2.10}$$

In equation (2.10) the terms within the ket $|n_i, n_s, m, \varphi\rangle$ are the number of incident photons (n_i), number of scattered photons (n_s), number of phonons (m) and the electronic state (φ), respectively; E_e^v and E_e^c are the energies of the electron in the valence and conduction bands. The signal (+) corresponds to the Stokes process (phonon creation) and the signal (−) to the anti-Stokes process (phonon annihilation).

Up to now, we have the overall picture of the Raman process depicted in Figure 2.2. Next, we need to translate these scattering paths into their respective contribution to the expansion of the Raman scattering probability. To do this, we consider the Fermi's golden rule which is given by (Yu and Cardona, 2010)

$$W_{i \rightarrow j} = \frac{2\pi}{\hbar} |\langle i | \mathcal{H}_{scatt} | j \rangle|^2 \rho(E_j). \tag{2.11}$$

Equation (2.11) gives the probability of an electron at an initial state i and energy E_i to absorb a photon with energy $\hbar\omega$ going to a final state j with energy E_j .

Thus, using equation (2.11), we can write down the contribution of the Raman process depicted in Figure 2.2 (*i.e.*, one phonon being either created or annihilated), which is given by (Yu and Cardona, 2010)

$$P_{\text{Raman}} = \left(\frac{2\pi}{\hbar} \right) \left| \sum_{a,b} \frac{\langle f | \mathcal{H}_{eR} | b \rangle \langle b | \mathcal{H}_{eL} | a \rangle \langle a | \mathcal{H}_{eR} | i \rangle}{[\hbar\omega_i - (E_a - E_i)] [\hbar\omega_i - \hbar\omega_{ph} - (E_b - E_i)] [\hbar\omega_i - \hbar\omega_{ph} - \hbar\omega_s]} \right|^2 \cdot \delta(\hbar\omega_i - \hbar\omega_{ph} - \hbar\omega_s). \quad (2.12)$$

The $|a\rangle$ and $|b\rangle$ states and their respective energies E_a and E_b are virtual states in the process. The sum considers the transition probability over all possible states in the process. It is important to comment that energy is conserved over all scattering but not for the individual scattering processes (Yu and Cardona, 2010). We comment that equation (2.12) is the Fermi's golden rule for a first-order Raman process, which is obtained by using third order time-dependent perturbation theory. Details about the mathematical approach of the perturbation expansion can be found in (Martin and Falicov, 1983; de Oliveira Lopes Cançado, 2006; Martins, 2015).

Notice that the denominator of equation (2.12) has three terms and they are responsible to reach the resonance condition in the Raman scattering process. The probability transition of the Raman scattering is significantly increased when the incoming (scattered) photon, $\hbar\omega_i$ ($\hbar\omega_s = \hbar\omega_i - \hbar\omega_{ph}$), and the electron-hole energy, $E_a - E_i$ ($E_b - E_i$) becomes zero. In other words, every vertex has a resonance condition creating a singularity when the denominator becomes zero. This process is called resonant Raman scattering (RRS) and has been widely applied in the study of two-dimensional materials, since it provides information about the electron and phonon dispersion of the material (Yu and Cardona, 2010).

The resonance condition is a result of implicitly assuming an infinite lifetime for every state involved in equation (2.12). Thus, in order to avoid an unphysical situation where the denominator vanishes, we make a transition $E_x \rightarrow E_x + i\Gamma_x$. Therefore, a finite lifetime (a damping constant)

for each state $|\chi\rangle$ (defined as $\Gamma_\chi = \hbar/\tau_\chi$) is introduced. Thus, equation (2.12) becomes (Yu and Cardona, 2010),

$$P_{\text{Raman}} \approx \left(\frac{2\pi}{\hbar} \right) \left| \sum_{a,b} \frac{\langle f | \mathcal{H}_{eR} | b \rangle \langle b | \mathcal{H}_{eL} | a \rangle \langle a | \mathcal{H}_{eR} | i \rangle}{(E_i - E_a - i\Gamma_a)(E_i - E_b - i\Gamma_b)} \right|^2. \quad (2.13)$$

We stress that equation (2.12) is not the complete probability transition of the Raman scattering process. There are five more scattering probability of time order terms, as depicted in Figure 2.3, and their complete derivation can be found in (Yu and Cardona, 2010). However, for the sake of completeness, we show below the complete probability transition for one-phonon Stokes scattering process,

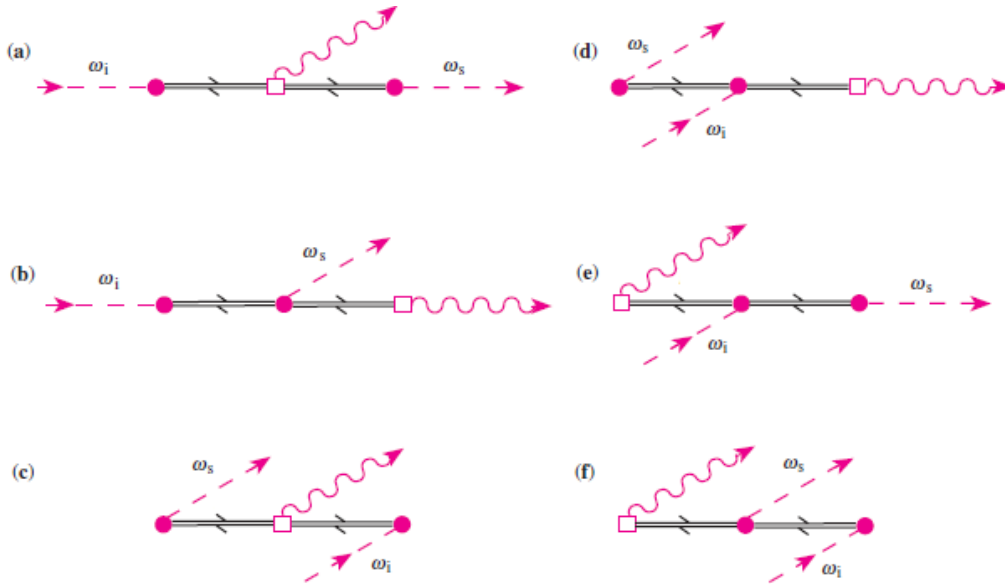


Figure 2.3: **All six Feynman diagrams contributions for one-phonon Stokes process.** Feynman diagrams for the six possible scattering processes for one-phonon stokes scattering (a-f). (b-f) are permutations of (a). Adapted from (Yu and Cardona, 2010).

$$\begin{aligned}
P_{\text{Raman}} = & \left(\frac{2\pi}{\hbar} \right) \left| \sum_{a,b} \frac{\langle i | \mathcal{H}_{eR}(\omega_i) | a \rangle \langle a | \mathcal{H}_{eL} | b \rangle \langle b | \mathcal{H}_{eR}(\omega_s) | i \rangle}{[\hbar\omega_i - (E_a + i\Gamma_a)] [\hbar\omega_i - \hbar\omega_{ph} - (E_b + i\Gamma_b)]} \right. \\
& + \sum_{a,b} \frac{\langle i | \mathcal{H}_{eR}(\omega_i) | a \rangle \langle a | \mathcal{H}_{eR}(\omega_s) | b \rangle \langle b | \mathcal{H}_{eL} | i \rangle}{[\hbar\omega_i - (E_a + i\Gamma_a)] [\hbar\omega_i - \hbar\omega_s - (E_b + i\Gamma_b)]} \\
& + \sum_{a,b} \frac{\langle i | \mathcal{H}_{eR}(\omega_s) | a \rangle \langle a | \mathcal{H}_{eL} | b \rangle \langle b | \mathcal{H}_{eR}(\omega_s) | i \rangle}{[-\hbar\omega_s - (E_a + i\Gamma_a)] [-\hbar\omega_s - \hbar\omega_{ph} - (E_b + i\Gamma_b)]} \\
& + \sum_{a,b} \frac{\langle i | \mathcal{H}_{eR}(\omega_s) | a \rangle \langle a | \mathcal{H}_{eR}(\omega_i) | b \rangle \langle b | \mathcal{H}_{eL} | i \rangle}{[-\hbar\omega_s - (E_a + i\Gamma_a)] [-\hbar\omega_s + \hbar\omega_i - (E_b + i\Gamma_b)]} \\
& + \sum_{a,b} \frac{\langle i | \mathcal{H}_{eL} | a \rangle \langle a | \mathcal{H}_{eR}(\omega_i) | b \rangle \langle b | \mathcal{H}_{eR}(\omega_s) | i \rangle}{[-\hbar\omega_{ph} - (E_a + i\Gamma_a)] [-\hbar\omega_{ph} + \hbar\omega_i - (E_b + i\Gamma_b)]} \\
& + \sum_{a,b} \frac{\langle i | \mathcal{H}_{eL} | a \rangle \langle a | \mathcal{H}_{eR}(\omega_s) | b \rangle \langle b | \mathcal{H}_{eR}(\omega_i) | i \rangle}{[-\hbar\omega_{ph} - (E_a + i\Gamma_a)] [-\hbar\omega_{ph} + \hbar\omega_s - (E_b + i\Gamma_b)]} \Bigg|^2 \\
& \cdot \delta[\hbar\omega_i - \hbar\omega_{ph} - \hbar\omega_s]
\end{aligned} \tag{2.14}$$

In the equation (2.14), the energy E_i was set equal to zero and, the finite lifetime of the $|a\rangle$ and $|b\rangle$ states were considered.

To this end, we comment that for the case where more than one-phonon is involved in the scattering process. The equation (2.13) can be expanded to higher orders of perturbation and new states encompassed. Therefore, in the case where two-phonons or a phonon plus any spreader that assure the momentum conservation (*e.g.* defects) are involved in the scattering process, equation (2.13) is writing down as

$$P_{\text{Raman}}^{\text{two-phonons}} \approx \left(\frac{2\pi}{\hbar} \right) \left| \sum_{a,b} \frac{\langle f | \mathcal{H}_1 | c \rangle \langle c | \mathcal{H}_1 | b \rangle \langle b | \mathcal{H}_1 | a \rangle \langle a | \mathcal{H}_1 | i \rangle}{(E_i - E_a - i\Gamma_a) (E_i - E_b - i\Gamma_b) (E_i - E_c - i\Gamma_c)} \right|^2, \tag{2.15}$$

where $|i\rangle$, $|a\rangle$, $|b\rangle$, $|c\rangle$ and $|f\rangle$ represent the states involved in the scattering process and \mathcal{H}_1 is the perturbed Hamiltonian. Equation (2.15) represents a second-order Raman process and has three terms in the denominator.

In chapters 4 and 5, the equations (2.13) and (2.15) are applied to study mono- and few-layered MoS₂. In chapter 4, the first-order modes are presented and their resonance behavior unveiled by the use of equation (2.13). In chapter 5, we studied the second-order modes, an alternative approach to obtain equation (2.15) is shown by considering a parabolic band to depict it and, the dispersive behavior of some Raman features are explained by the use of equation (2.15). In the following section, the Raman spectrum of MoS₂ TMD is briefly described by making some analogies between graphene and MoS₂ in their Raman spectra.

2.3 Overview of Raman spectroscopy in graphene and MoS₂ transition metal dichalcogenide

Having graphene as the prototype material allow us to gain further insights of a particular 2D system leading to a new route in understanding the fundamental physics. With this in mind, it is essential to compare the Raman spectrum of graphene and TMDs systems.

Figure 2.4(a) shows the Raman spectrum of monolayer graphene. We can observe the so-called G band around 1580 cm⁻¹, which here we will call the E_{2g} band, since it corresponds to the zone-center Raman active mode with E_{2g} symmetry. Around 2700 cm⁻¹, we can observe a very strong peak, which is associated with two phonons of the iTO branch near the **K** point, and that is called in the literature as 2D or G' band. Since both denominations lack a precise physical meaning, we will call this feature here as the 2TO(**K**) band. Notice that, despite the fact that this 2TO(**K**)

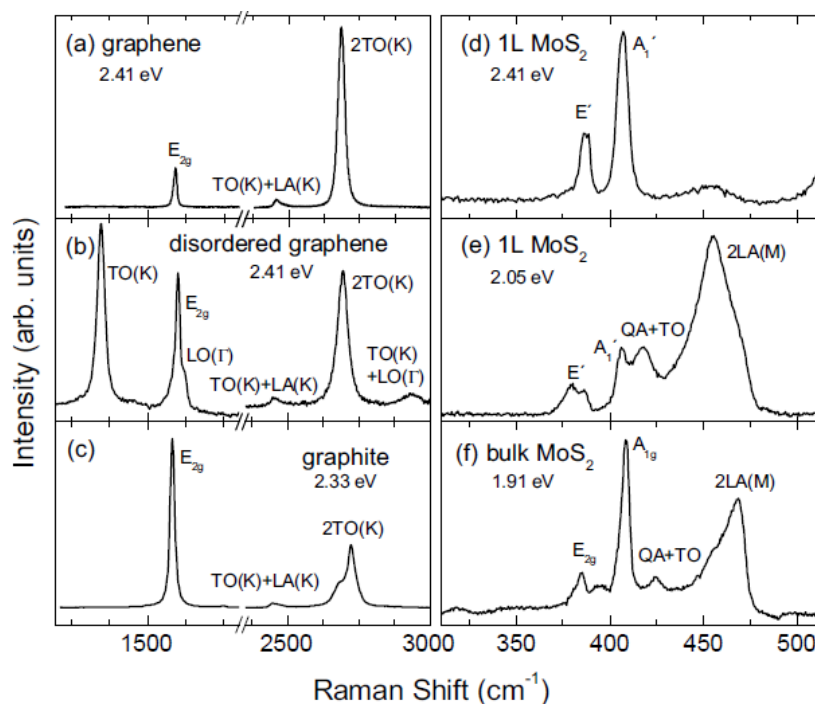


Figure 2.4: **Raman spectra comparison of graphene and TMDs.** Raman spectra of (a) graphene; (b) disordered graphene; (c) graphite; (d) and (e) monolayer MoS₂ excited with different laser lines; (f) bulk MoS₂. The different excitation energies (in eV) are represented. For graphene and graphite, the E_{2g}, TO(K), LO(Γ) and 2TO(K) bands corresponds, respectively, to the so-called G, D, D' and 2D (or G') bands. Taken and adapted from (Pimenta et al., 2015).

band comes from a second-order process, it is usually more intense than the first-order E_{2g} band (G band) in monolayer graphene. Figure 2.4(c) shows the Raman spectrum of crystalline graphite, where we can see both the E_{2g} and 2TO(K) bands. Notice that the 2TO(K) band of graphite is weaker than the E_{2g} band and is clearly asymmetric, different from the case of monolayer graphene (Ferrari et al., 2006; Malard et al., 2009).

It was proposed many years ago that the 2TO(K) band of graphitic systems is originated by a double resonance Raman (DRR) process, where

two intermediate states of the Raman process are in resonance with real electronic states (Baranov et al., 1987; Thomsen and Reich, 2000). In this case, two of the terms in the denominator of the Raman intensity expression are simultaneously resonant (see equation (2.15) above), explaining why this second-order feature can be as intense as the first-order E_{2g} band. The fact that the $2TO(\mathbf{K})$ band can be even more intense than the E_{2g} band in monolayer graphene was ascribed to a triple-resonance (TR) Raman process, where all intermediate states of the Raman process, involving electrons and holes, are resonant (Venezuela et al., 2011).

Figure 2.4(b) shows the Raman spectrum of a sample of disordered graphene. We can observe in this figure a strong feature around 1350 cm^{-1} , that is usually called the D-band, where the letter D stands from disorder (or defect). This band also comes from a DRR process, but involving only one phonon of the iTO branch, near the \mathbf{K} point. In this case, an elastic scattering process involving defects is needed for momentum conservation, and the presence of this band is a signature of defects or disorder in graphene systems. Since other Raman bands are also related to disorder or defects in graphene systems (Pimenta et al., 2007), it is interesting to give a more precise notation for the D band, and we will call it here as the $TO(\mathbf{K})$ band. The origin of the other weak features in the Raman spectra of graphene systems is well discussed in (Pimenta et al., 2007) and (Malard et al., 2009).

Let us now make a comparison between the Raman spectra of graphene and MoS_2 TMD, discussing the similarities, the differences, and how the Raman spectrum of MoS_2 provides useful information for this system. Figure 2.4(d) shows the spectra of monolayer MoS_2 recorded with the 2.41 eV laser line. The two prominent peaks in these figures correspond to the first-order Raman active modes with E' and A'_1 symmetries. The E' mode is somewhat similar to the E_{2g} mode of graphene (G band), since it involves an in-plane vibration of the sublattice formed by metal atoms

against the sublattices formed by the chalcogens. The A'_1 mode of TMDs has no correspondence with graphene, since it corresponds to out-of-plane vibrations of the upper and lower sublattices of chalcogen atoms against each other.

Figure 2.4(e) shows the spectrum of monolayer MoS_2 , but now recorded with 2.05 eV laser energy. Notice that the Raman spectrum of MoS_2 is strongly dependent on laser energies, since the spectrum in Figure 2.4(e) is completely different from that shown in Figure 2.4(d). We can see now a number of features that are associated with second-order processes involving combinations (sums and differences) of phonons within the interior of the Brillouin zone. A detailed study of the second-order bands in MoS_2 can be found in (Sekine et al., 1980a) and (Sourisseau et al., 1991; Golasa et al., 2014; Stacy and Hodul, 1985; Chen and Wang, 1974).

Here we will only focus on the most intense second-order feature, which involves two phonons of the longitudinal acoustic (LA) branch with opposite momenta, at the \mathbf{M} point of the Brillouin zone. This band is, therefore, called the $2\text{LA}(\mathbf{M})$ band (Chen and Wang, 1974). It is interesting to observe that the second order $2\text{LA}(\mathbf{M})$ band is more intense than the first-order A_1 and E' bands in Fig. 2.4(e), and this result is similar to the behavior of graphene, where the $2\text{TO}(\mathbf{K})$ band is more intense than the first order E_{2g} band (see Figure 2.4(a)). The Raman spectrum of bulk MoS_2 is shown in Fig. 2.4(f). The positions and attribution of the Raman features is the same as monolayer MoS_2 but now the $2\text{LA}(\mathbf{M})$ band is less intense than the first-order A_{1g} band. Notice that this behavior is similar to crystalline graphite, where the $2\text{TO}(\mathbf{M})$ band is less intense than the E_{2g} (see Figure 2.4(c)).

The fact of the $2\text{LA}(\mathbf{M})$ band be stronger than the first-order bands in monolayer suggests that the second-order spectra in MoS_2 also involve a double or triple resonance processes, as in the case of graphene. It has been demonstrated, the double resonance process in TMDs was calculated

using a fourth-order Fermi golden rule, and it was demonstrated that the intensity of the 2LA(**M**) band comes from a DRR Raman process involving phonons at the **M** point of the Brillouin zone (Berkdemir et al., 2013). Many other weak peaks also comes from a combination of phonons at the **M** point (Golasa et al., 2014).

Thus, how is the DRR mechanism of this band? Well, the essential check for the DRR mechanism is a resonance Raman experiment, where the Raman spectra is studied as a function of the laser excitation energy. Once again let us compare with graphene. Figure 2.5 shows the spectra of graphene and MoS₂, respectively, recorded with different laser lines. In the graphene spectra, we only show the spectral region of the 2TO(**K**) band. Notice in Figure 2.5a that the 2TO(**K**) band is dispersive, its position depending linearly on the laser energy in the visible range. This behavior can be explained by the DRR process in graphene (Malard et al., 2009; Ferrari et al., 2006). Due to the linear dispersion of electrons in graphene, the Raman process is always resonant, because the energy of the incident photon will always correspond to the separation between the conduction and valence band in a specific point in the Brillouin zone near the Dirac (or **K**) point. The 2TO(**K**) band is associated with an intervalley process, involving resonances with valleys around the **K** and **K'** points. Thus, the wave vector of the phonon connecting points around **K** and **K'** is, in fact, close to the **K** point. Therefore, when the double- and triple-resonance processes that originate the 2TO(**K**) band are probed with different laser lines, phonons with different wave vectors around **K** are involved, and consequently the position of the 2TO(**K**) band changes and provides information about the dispersion of electrons and phonons in graphene systems (Malard et al., 2009).

Figure 2.5b shows the Raman spectra of monolayer MoS₂ recorded with different laser lines. Now we can observe that the 2LA(**M**) band is not dispersive, and only its intensity changes with varying laser energy.

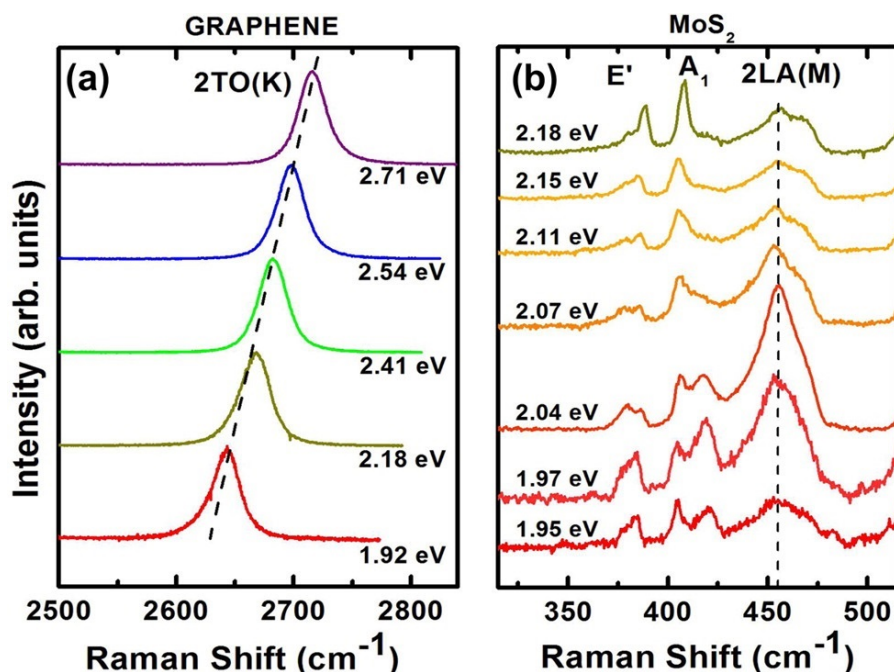


Figure 2.5: **The Double-resonance Raman spectra.** Dependence of the double-resonance bands of (a) graphene and (b) monolayer MoS₂ on the laser energies. Taken and adapted from (Pimenta et al., 2015).

In particular, the 2LA(M) band is more intense for laser energies around 2 eV, which corresponds to the B exciton energy in monolayer MoS₂ (Qiu et al., 2013; Mak et al., 2010), suggesting that it is really associated with a double-resonance process. Resonance Raman scattering can provide useful information about the electronic states of these materials.

The DRR mechanism for TMDs has been proposed by Berkdemir et al., where it now involves resonances at valleys at the **K** and **Q** points (the **Q** point is the intermediate point between Γ and **K**, see Figure 1.2(c)) (Berkdemir et al., 2013). The authors have shown that the phonon that connects these two valleys has a wave vector at the **M** point. The optical spectrum of TMD systems of the MoS₂ family is dominated by excitonic transitions involving electronic states at the **K** point (see chapter 1) (Qiu

et al., 2013). A resonant process with excitonic states will be proposed in chapter 5. Figure 2.5b shows that the double-resonance mechanism will enhance the intensity of 2(LA) bands only in a small range of energies that are in close resonance with the exciton states at the **K** point and the intermediate state at the **Q** point. Therefore, the process involving resonances with excitonic transitions in TMDs explains the observed results shown in Figure 2.5b, where the intensity of the 2LA(**M**) band, and not its frequency, depends on the laser energy. Although this proposed DRR model seems reasonable, the lineshape of the 2LA band compared to the 2TO of the graphene is completely different and, may involve several another process that has not been considered. Therefore, we can say that a systematic deconvolution study of this 2LA band is needed to unveil the DRR process that occurs in this material and, it has not been reported thus far, remaining an open question for more three decades (Chen and Wang, 1974; Sekine et al., 1984).

By summarizing, we notice that the Raman spectrum of MoS₂ strongly depends on the laser excitation energy and, especially when collected under resonance condition, *i.e.* when the excitation energy matches the excitonic transition, a new Raman feature appears. The goal of this thesis is to unveil such behave. We first start by analyzing the first-order modes (E_{2g}^1 and A_{1g}) and their dependence at higher energies to understanding the exciton-phonon interaction dynamics. Next, we systematically study the double-resonance process in MoS₂ and, we proposed a model to explain the origin of the 2LA band and identify all its contributions.

3 EXPERIMENTAL METHODOLOGY

In this chapter, a brief description of the experimental techniques employed in this thesis is discussed. Firstly, we present the methodologies for sample preparation followed by the Raman instrumentation used to collect the data.

3.1 Sample preparation

Different techniques can be utilized for the preparation of mono- and few-layered TMDs. However, two of them have been extensively used in past years, and both have their advantage and disadvantage, depending on the targeted application. Below, the basic concept of each technique is discussed.

Mechanical exfoliation

The mechanical exfoliation (also known as “Scotch-tape method” or “mechanical cleavage”) is the most common technique used for obtaining 2D layered materials (Novoselov et al., 2004); its advantage holds on the sample quality having almost no defects and high crystallinity. However, the sample size is relatively small what makes it unable to have a large-scale production. It was first employed to prepare monolayer graphene sheets by repeatedly peeling bulk graphite with adhesive tape (Novoselov et al., 2004). For the MoS₂'s case, the first exfoliated sample was obtained by Frindt using this “scotch-tape technique” and, by peeling bulk MoS₂ in thin layer, he was able to obtain a thin layer of around 3.5 nm thickness (Frindt, 1966). Novoselov et al. reported that was also possible to extract monolayer TMDs by just rubbing a fresh surface of layered crystals against another solid surface (*e.g.* a SiO₂/Si wafer), similar to “drawing by chalk

on a blackboard” (Novoselov et al., 2005). The possibility in peeling out a bulk crystal is due to the weak van der Waals interaction between layers. Figure 3.1 shows a step-by-step procedure of this technique, where a thick layer of MoS₂ has adhered onto a piece of Scotch tape. After that, the tape with the MoS₂ flake is repetitively cleaved by folding and separating the tape for many times to obtain 2D few-layered sheets and, then placed onto a SiO₂/Si substrate. After obtaining the few-layers sample, the number of layers is identified by an optical microscope and confirmed by Raman measurements (Novoselov et al., 2005; Lee et al., 2010).

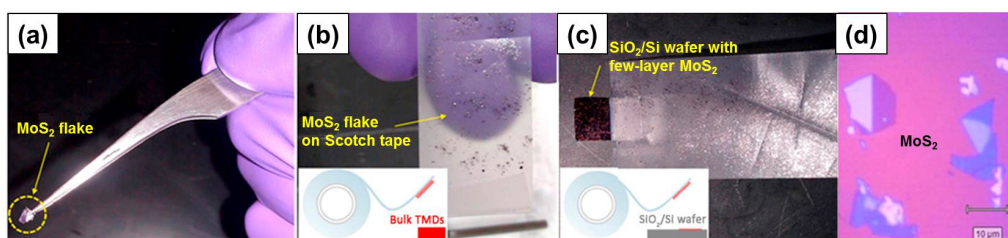


Figure 3.1: **The Scotch-tape method.** (a-c) mechanical exfoliation method used for obtaining mono- and few-layered 2D TMD sheets. The insets in (b) and (c) correspond to schemes for “Scotch tape” peeling steps. (d) Optical image of as-exfoliated MoS₂ flakes. Adapted from (Lv et al., 2015).

The high-transparency of atomically thin TMD materials makes the choice of the substrate used for supporting the samples extremely necessary to be visible under an optical microscope (Novoselov et al., 2005; Castellanos-Gomez et al., 2010). Similar to graphene, oxidized Si wafer (*i.e.* SiO₂/Si) has been found to be the best substrate material due to its high phase contrast between the TMD-covered area and the empty part onto SiO₂/Si substrate. In this thesis, the MoS₂ samples were obtained by mechanical exfoliation of natural 2H-MoS₂ crystals transferred onto Si substrates with 298 and 300 nm thick SiO₂ coating, which assure the optical contrast of the MoS₂ and the SiO₂/Si wafer.

Chemical vapor deposition

Beyond mechanical exfoliation, chemical vapor deposition (CVD) is the second most common technique used to prepare 2D materials. By using CVD methodology, several inorganic materials, such as carbon-based material (Zhu et al., 2002; Li et al., 2009), and Boron Nitride nanostructures (Golberg et al., 2007; Song et al., 2010) can be synthesized. Here, the growth process occurs by chemical reactions at relatively high temperatures.

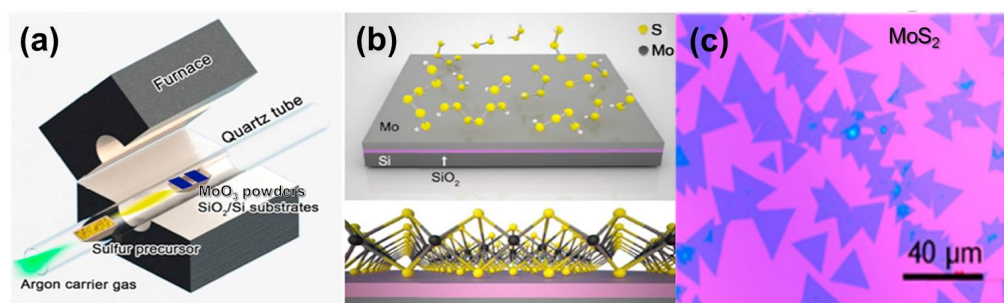


Figure 3.2: **The CVD method.** (a) Schematics showing the experimental set-up used for growing MoS₂ atomic layers. (b) Schematics showing the growth of MoS₂ atomic layers onto the SiO₂/Si substrate. (c) Optical image of as-synthesized triangular monolayers of MoS₂. Adapted from (Lv et al., 2015; Li and Östling, 2015).

For graphene synthesis, for example, it requires a metallic catalytic substrate, such as Cu and Ni with a growth process occurring at a temperature of ~ 1100 °C (Li et al., 2009; Chae et al., 2009). But, for the synthesis of atomically thin TMDs, it can be growth on SiO₂/Si or a sapphire substrate, and it can be growth at a temperature below 1000 °C (Lee et al., 2012; Liu et al., 2012; Zhan et al., 2012). Figure 3.2 shows a typical MoS₂ CVD process, which usually occurs at atmosphere-temperature (APCVD) and, it is as follow: An alumina boat containing 400 mg of sulfur (Alfa Aesar, 99.5%) is located upstream and independently heated using a heating belt. Then, 5 mg of MoO₃ powder (Alfa Aesar, 99.998%) is placed directly on a 300 nm SiO₂/Si substrate and, then placed inside of quartz tube with

2 cm diameter. After that, the furnace is heated to 500 °C over 15 min, then heated to 750 °C over 15 min, held at that temperature for 15 min, and subsequently was allowed to cool to room temperature. The sulfur powder is heated separately. First, it is heated to 70 °C over 10 min with a subsequent 15 min dwell time, then ramped up to 250 °C over 5 min with a 15 min dwell time followed by naturally cooling down to room temperature. The quartz reaction tube is flushed with 300 sccm high-purity argon for 10 min to remove oxygen before the growth process started. The argon flow rate is usually set to 200 sccm during the growth. By this procedure, monolayer MoS₂ triangles are grown on the top of the substrate (Lin et al., 2014).

We stress that depending on the target TMD material (*e.g.* WS₂, MoSe₂, etc.) the precursor and the synthesis conditions need to be altered. This technique usually yields large flakes of the deposited material, but the sample quality is lower than the ones prepared by mechanical cleavage. In this thesis, as previously mentioned, the MoS₂ samples were prepared by mechanical cleavage, however, during the doctoral internship held at the Pennsylvania State University, several 2D samples were prepared by CVD technique and, some results involving these samples are presented in the appendix of this thesis.

To ensure an adhesion of the deposited material onto the substrates' surface, a cleaning procedure needs to be carried out. Therefore, before sample deposition, in both procedures, the SiO₂/Si substrates need to be cleaned. Firstly, the bare substrates were submerged in acetone and isopropyl alcohol solutions, about 25 ml of each, with the SiO₂ side up. Then, they were placed in an ultrasonic bath by 20 min each. After that, they are left to naturally dry and, then washed in a piranha bath, prepared using two-thirds of sulphuric acid and one-third of hydrogen peroxide, for about 60 min in a hot plate at a temperature of 80 °C. In some cases,

before the above cleaning procedure, the silicon substrate was previously placed in oxygen plasma around 25 min.

3.2 The Raman spectrometer

The Raman spectra presented in this thesis were collected on either a *DILOR XY* or *Horiba Jobin Yvon T64000*. Both systems have two operations mode, called single- and triple-monochromator modes, respectively. In this thesis, most of the Raman data was obtained in the *DILOR XY* system using the triple-monochromator mode. These spectrometers allow multi-wavelength measurements and, a full list of the lasers sources available on both spectrometers are shown in Table 3.1. In this thesis, we used multiple laser excitation wavelengths to study the Raman scattering process in MoS_2 . The primary laser sources were the Innova 70C Ar-Kr, 899-01 Dye Ring (which is a continuous laser) and the He-Cd. Their wavelengths are shown in Table 3.1.

Table 3.1: **Laser sources of the Raman laboratory.** List of laser sources equipping the two spectrometers of the Raman Laboratory. The excitation wavelength of the 899-01 Dye Ring laser depends on the type of dye used.

Spectrometer	Laser Source	Excitation Wavelength
DILOR XY	Innova 70C Ar-Kr	457.9, 465.8, 472.7, 476.5, 488.0, 501.7, 514.5, 520.8, 531.8, 568.2 and 647.1 nm
	899-01 Dye Ring	530–660 nm (continuous)
Horiba T64000	Innova 70C Ar-Kr	457.9, 465.8, 472.7, 476.5, 488.0, 501.07, 514.5, 520.8, 531.8, 568.2 and 647.1 nm
	He-Cd	325 and 441 nm
	Ti:Sapphire	730–900 nm (continuous)
	He-Ne	633 nm

Figure 3.3 briefly describes the basic setup of a typical Raman spectrometer, in which is mainly composed of four major parts: diffraction gratings, a detector, mirrors, and slits. The configuration of the single-

monochromator mode is shown in Fig. 3.3a and, is formed by a diffraction grating (G1), a slit (S1), and a detector (D). The scattered light is directed by a microscope (not shown) from the sample to the detector that measures the energy spectrum of the scattered light. More specifically, the back-scattered light from the sample is focused on S1, dispersed in G1 and, thus detected by D.

The resolution of a good Raman spectrum depends on several factors. First is the spatial resolution given by minimum spot size diameter of the laser beam (with a Gaussian shape) on the sample surface after the objective, which is defined as $d = \lambda \sqrt{\frac{1}{(\text{N.A.})^2} - 1}$; where N.A. is the numerical aperture of the objective lens and λ is the excitation laser wavelength. In this thesis, the Raman data were collected using a 100× objective lens with N.A. = 0.95. Whilst the diffraction limit permit laser beams of diameters similar or even smaller than the excitation wavelength, a real experiment has a spot size diameter in the order of 1 μm . Secondly is the spectral resolution determined by the capacity of the spectrograph to resolve small changes in photon energy. Therefore, it depends on the grooves density of the diffraction grating, the slit size and optical path along the grating to the detector. Thus, to achieve a high resolution just need to increase the grooves density, reduce the size of the slit, and enlarge the optical path of Raman beam. Both, *DILOR XY* and *Horiba T64000* has a grating of 1800 grooves/mm given a spectral resolution in order of 1 cm^{-1} . The *Horiba T64000* has an additional grating of 600 grooves/mm only used in the single-monochromator mode.

Also, the single-monochromator mode works only at a specific wavelength since it requires the use of an edge or notch filter to each laser wavelength. However, another approach consists of replacing the edge filter by adding other two grating to select a particular wavelength by just rotating the grating, whereby called triple-monochromator mode, shown in Fig. 3.3b.

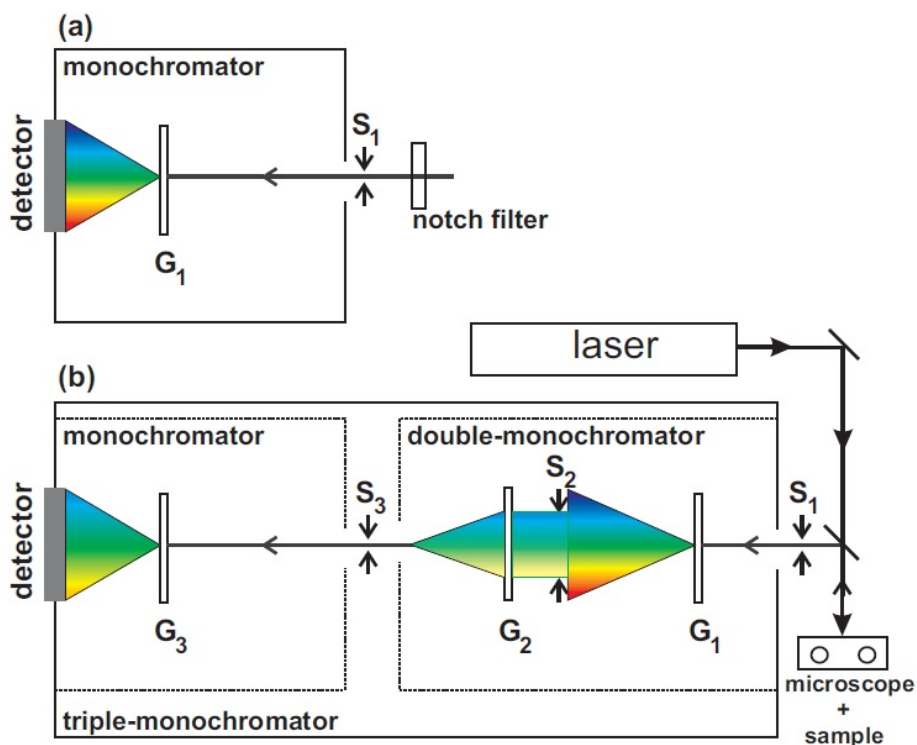


Figure 3.3: **Basic set-up of a Raman spectrometer.** Schematic view of a (a) monochromator and (b) triple-monochromator showing the basic set-up of the Raman spectrometer in our laboratory. Taken from (Moreira, 2009).

Different from the single-monochromator mode, the triple monochromator mode consist of three gratings (G_1 , G_2 , and G_3), three slits (S_1 , S_2 , and S_3) and a detector (D). Here, the G_1 grating disperses the inelastic light onto a slit S_2 filtering the desired energy range. Then, G_2 grating recombines what remains of the dispersed light and directs it onto the G_3 grating, that by dispersing the light once again, analyses the Raman signal. After that, the analyzed signal is sent to the detector. The first two steps, performed by G_1 and G_2 grating, is called subtractive mode since it rejects the Rayleigh signal of the laser source.

As mentioned, the main advantage of the triple-monochromator mode

lies on the use of several laser wavelengths (and even continuously tuning it) without the utilization of the edge filter. It even allows the measurement of low-frequency Raman modes close to the Rayleigh light. Although the triple-monochromator mode increases the spectral resolution, its Raman signal is significantly reduced compared to the signal collected in the single-monochromator mode.

3.3 Enhancement factor due to optical interference in the SiO₂ layer

The optical paths for both incoming and scattered light in the MoS₂ are complicated considering that they undergo an infinite number of reflections and refractions at the boundaries of the MoS₂ and the SiO₂. This optical interference can create enhancements for certain MoS₂ wavelengths and thus needs to be considered. The Raman spectra were collected in a system involving four media: air, MoS₂ layer, SiO₂ layer and silicon substrate and designated by the index $i = 0, 1, 2,$ and $3,$ respectively, as shown in Fig. 3.4a. It is well known that the scattered Raman light from MoS₂ and silicon will be modified due to interference in the light absorption and light scattering processes (Li et al., 2012b; Yoon et al., 2009). Therefore, we need to calculate the enhancement factor ($f_{\text{MoS}_2;\text{Si}}$) for the Raman scattered light from MoS₂ and silicon coming from the multiple interference phenomena (Li et al., 2012b). The corresponding complex index of refractions is given by $n_i = n - ik$ while the thickness of each layer is given by d_i .

The measured Raman intensity for MoS₂ on SiO₂/Si ($I_{\text{MoS}_2;\text{SiO}_2/\text{Si}}^m(\lambda)$) is given by,

$$I_{\text{MoS}_2;\text{SiO}_2/\text{Si}}^m(\lambda) = f_{\text{MoS}_2;\text{SiO}_2/\text{Si}} \times I_{\text{MoS}_2;\text{SiO}_2/\text{Si}}^i(\lambda), \quad (3.1)$$

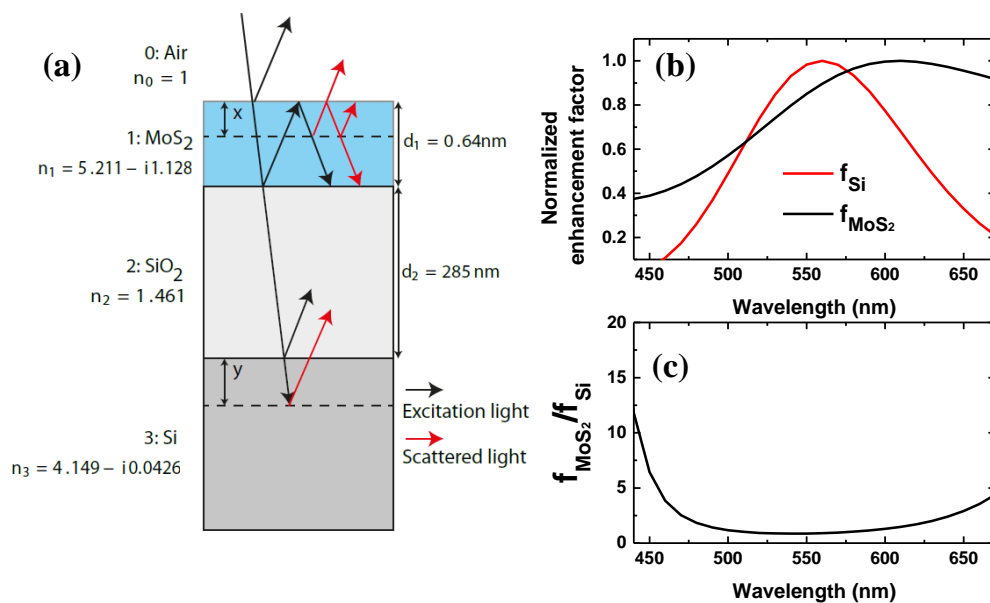


Figure 3.4: **Optical interference.** (a) Schematic diagram of the multiple reflections interference in the Raman scattering process; (b) Calculated Raman intensities as a function of the wavelength of the MoS₂ and Si; (c) Intensity ratio of the MoS₂ and Si enhancement factor.

where the intrinsic Raman intensity ($I_{MoS_2;Si}^i(\lambda)$) and the enhancement factor ($f_{MoS_2;SiO_2/Si}$), comes from the multiple interference pattern in the SiO₂ layer. Including multiple reflections at the top of the MoS₂ layer (total thickness d_1) is (Li et al., 2012b):

$$f_{MoS_2} = \int_0^{d_1} |F(x)G(x)|^2 dx, \quad (3.2)$$

where $F(x)$ and $G(x)$ are the electrical field amplitude for the excitation

and scattering light at a depth x in MoS_2 [see figure 3.4a]. The functions $F(x)$ and $G(x)$ are given by,

$$\begin{aligned} F(x, \lambda_{ex}) &= t_{01} \frac{e^{-i\beta_x} + r' e^{-i(2\beta_1 - \beta_x)}}{1 + r' r_{01} e^{-2i\beta_1}}, \\ G(x, \lambda_{sc}) &= t_{10} \frac{e^{-i\beta_x} + r' e^{-i(2\beta_1 - \beta_x)}}{1 + r' r_{01} e^{-2i\beta_1}}, \end{aligned} \quad (3.3)$$

where t_{ij} and r_{ij} are the transmission and reflection Fresnel coefficients at the interfaces and are given by $t_{ij} = 2n_i/(n_i + n_j)$ and $r_{ij} = (n_i - n_j)/(n_i + n_j)$ when a beam reaches the interface ij going from medium i (index of refraction n_i) to medium j (index of refraction n_j) [see figure 3.4a]. There are also phase factors, given by $\beta_x = 2\pi n_1 x/\lambda$ and $\beta_j = 2\pi n_j d_j/\lambda$, that represent the phase differences through path x in MoS_2 and the entire medium j , where d_j is the thickness of a given layer and λ is the wavelength of light. The effective reflection coefficient r' is due to interference at the $\text{MoS}_2/\text{SiO}_2$ interface, including the lower SiO_2/Si layer, and is given by:

$$r' = \frac{r_{12} + r_{23} e^{-2i\beta_2}}{1 + r_{12} r_{23} e^{-2i\beta_2}}. \quad (3.4)$$

It is important to note that, while the absorbed light is calculated for a given laser excitation wavelength (λ_{ex}), the scattered light is calculated for the wavelength corresponding to the scattered Raman wavelength (λ_{sc}). Besides, note that although the expressions for $F(x)$ and $G(x)$ are the same, the n_i and wavelength differences would lead to different results. Thus, we have used previously reported values for the complex index of refraction (given at 532 nm) for each layer (MoS_2 , SiO_2 , and Si which are calculated from the real and imaginary parts of the dielectric function for MoS_2 , as shown in Fig. 3.4a), 285 nm for SiO_2 thickness, and assumed a

Raman Shift of 400 cm^{-1} to calculate the enhancement factor for MoS_2 , as shown in Fig. 3.4b, as a function of the excitation wavelength.

Next, we need to consider the intensity of the Raman light from the silicon substrate (usually 0.3 mm thick) which is given by:

$$I_{\text{Si}}^m(\lambda) = f_{\text{Si}} \times I_{\text{Si}}^i(\lambda), \quad (3.5)$$

where $I_{\text{Si}}^m(\lambda)$ is the intrinsic intensity and f_{Si} the enhancement factor from the silicon substrate that is given by,

$$f_{\text{Si}} = \int_0^\infty |H(y) K(y)|^2 dy, \quad (3.6)$$

where $H(y)$ and $K(y)$ are the electrical field amplitude of the total absorbed light and scattered light at a depth y into the Si [see figure 3.4a]. Both quantities are given by:

$$\begin{aligned} H(y, \lambda_{\text{ex}}) &= \frac{t_{01} t_{12} t_{23} e^{-i(\beta_1 + \beta_2)} e^{-i\beta_y}}{1 + r_{01} r_{12} e^{-2i\beta_1} + r_{12} r_{23} e^{-2i\beta_2} + r_{01} r_{23} e^{-2i(\beta_1 + \beta_2)}}, \\ K(y, \lambda_{\text{sc}}) &= \frac{t_{32} t_{21} t_{10} e^{-i(\beta_1 + \beta_2)} e^{-i\beta_y}}{1 + r_{21} r_{32} e^{-2i\beta_2} + r_{21} r_{10} e^{-2i\beta_1} + r_{10} r_{32} e^{-2i(\beta_1 + \beta_2)}}. \end{aligned} \quad (3.7)$$

Again, a new phase factor $\beta_y = 2\pi n_3 y / \lambda$ need to be defined here, for both transmittance coefficients, to consider the depth in the Si.

Assuming the same values for the thickness and index of refraction for each layer as before and a Raman shift of 520 cm^{-1} , we have calculated the f_{Si} as a function of the excitation wavelength in Fig. 3.4b. It is well known that the index of refraction depends on wavelength. Therefore, we have also tested the same calculation for an index of refraction of MoS_2 near 400 nm: $n_1 = 4.2 - i3.1$. The results are similar, although the f_{MoS_2} does

not go to zero at destructive interference points.

In order to correct our data, it is needed to multiply the measured data after the normalization with the silicon substrate by the ratio $f_{\text{MoS}_2}/f_{\text{Si}}$ that is shown in Fig. 3.4c. We have tested this calibration scheme to our data and, it does not changes strongly the peak heights and widths, and the position of the resonant Raman profiles to be shown in the next chapter. However, for a quantitative analysis of the Raman cross section in MoS₂ the above analysis should be taken into account. Microscopic methods can be more accurate and do not rely on this phenomenological model in order to extract the Raman cross section in 2D materials as shown in (Klar et al., 2013).

It is important to comment that equation (3.6) is only valid because we are assuming a uni-dimensional problem. In this case, the Si is considered as a half-infinite medium (Soubelet et al., 2016; Delhaye et al., 1996). Otherwise, for a large numerical aperture objective with a small focal depth, it is necessary to consider the divergence effect of the focused Gaussian beam with respect to the numerical aperture of an objective lens and, then calculate the integral in a probed volume defined by the depth of focus. According to (Delhaye et al., 1996), it is given by:

$$\Delta f = \frac{\pi w_0^2}{2\lambda_n} \quad (3.8)$$

where Δf is the depth focus, w_0 is the beam radius at the waist (smallest spot size in the focus) and λ_n is the wavelength within the material ($\lambda_n = \lambda/n$). By taking that into account, the upper integral limit (until infinity) must be modified to $\Delta f/2$. The equation (3.8) is mainly useful for infrared wavelengths where the penetration depth of focus increases for Si (Soubelet et al., 2016).

We stress that the equation (3.7) has been corrected in this thesis. The

previous terms r_{23} and r_{10} in (Li et al., 2012b) has been replaced by t_{23} and t_{10} for $H(y)$ and $K(y)$, respectively. This error was found after recalculating the expressions in (Li et al., 2012b). Although this change has been made, it does not affect our conclusion above. Besides, the transmittance coefficients now are in agreement with those reported in (Heavens, 1991).

3.4 Resonant Raman behavior of silicon

Another procedure to be considered in the normalization of the Raman data is the Raman cross-section of the Si in respect to the laser excitation wavelength. Here, we normalized the intensity of the MoS_2 first-order modes by the intensity of the Si peak at 521.6 cm^{-1} , by considering the behavior of this Si peak as a function of the laser excitation wavelength (Renucci et al., 1975), as shown in Figure 3.5. As can be seen, the Raman scattering cross section for this Si peak increases for excitation energies in the UV range. In order to make sure of the values for the scattering cross section, we have measured the Raman spectra of Si for some laser wavelengths (black squares) in our laboratory and compared to the Renucci et al. (green dots), which shows an excellent agreement. Therefore, we used the values in Fig. 3.5 to normalized the Raman spectra of MoS_2 .

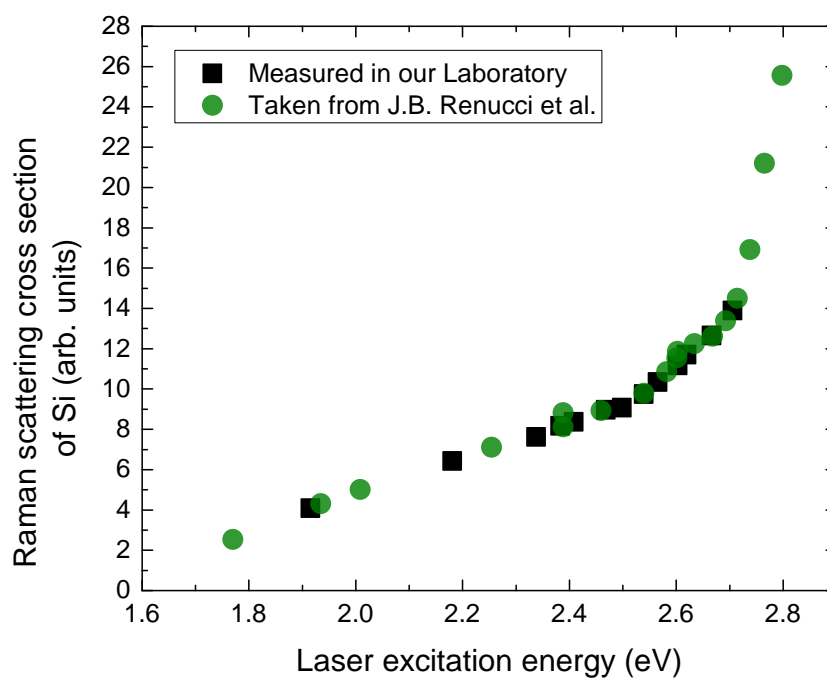


Figure 3.5: **Raman cross section of Si.** Raman scattering cross section of first-order phonon in silicon as a function of the laser excitation energy. The green circles were taken from (Renucci et al., 1975) and the black squares were measured in the Raman laboratory at UFMG. Here, the both data were normalized with respect to CaF_2 and considering $\delta = 0$, see (Renucci et al., 1975) for details.

4 SYMMETRY-DEPENDENT EXCITON-PHONON COUPLING IN 2D AND BULK MoS₂ OBSERVED BY RESONANCE RAMAN SCATTERING

In this chapter, the coupling between the excitons and first-order phonon modes in MoS₂ is discussed. The Raman excitation profiles of these bands were obtained experimentally, and it is found that the totally symmetric A_{1g} phonon mode is enhanced at any excitonic transition of MoS₂, while the E_{2g}¹ feature is shown to be enhanced when the only at high excitation laser. We show that the exciton-phonon coupling in this materials depend on the symmetry of the exciton orbitals and phonons. This work was developed in the Raman laboratory at UFMG, and published in the journal **PHYSICAL REVIEW LETTERS** 114 (13), 136403 (2015).

4.1 Introduction

Excitonic effects are expected to be very strong and influence the optical properties of 2D materials, such as the MoS₂-type transition metal dichalcogenides (TMDs), giving rise to the rich physics reported in the literature (Qiu et al., 2013; Xu et al., 2014; Mak et al., 2014). Resonance Raman spectroscopy is a very useful tool to study excitonic transitions and exciton-phonon interactions in semiconductors (Yu and Cardona, 2010) and, in this chapter, we present a resonance Raman study of 1L, 2L, 3L and bulk MoS₂ samples. Our results show that A_{1g} feature is enhanced when the excitation laser is in resonance with all excitons of MoS₂, while E_{2g}¹ feature is shown to be enhanced when the excitation laser is close to 2.7 eV, in a region of the optical spectrum of MoS₂ that possesses a diversity of excitonic states that cannot be distinguished at room temperature (Qiu et al., 2013). We present a symmetry analysis that shows that the

in-plane E_{2g}^1 phonon couples preferentially with the predicted high energy excitonic state near the Γ point, called the C exciton (Qiu et al., 2013). Our results show that phonons of MoS₂ with different symmetries are enhanced by different types of excitons, and provide experimental values for the dependence of the exciton energies and lifetimes on the number of layers.

Sekine et al. were the first to report a resonance Raman study of TMD compounds and measured the Raman excitation profile (REP) of the A_{1g} and E_{2g}^1 modes of bulk 2H- MoS₂, -WS₂, -MoSe₂ and -WSe₂, using many different laser lines in the energy range of 1.6–2.8 eV (Sekine et al., 1980b). In the case of MoS₂ and WS₂, only the A_{1g} mode was observed to resonate with the A and B excitons, but both A_{1g} and E_{2g}^1 peaks were enhanced at higher energies. This high energy resonance was observed to be broad and it was attributed to transition between high density of states in the valence and conduction bands. Sourisseau et al. have also measured the REP of the A_{1g} and E_{2g}^1 bands for bulk WS₂ in the range of the A and B excitons (Sourisseau et al., 1991) and similar results to those reported in (Sekine et al., 1980b) were obtained. Frey et al. showed using dynamics calculation that the electronic structure is modulated when applying the A_{1g} -mode displacement for the material, but not significantly affected by the E_{2g}^1 -mode displacements (Frey et al., 1999). These previous works show that the A_{1g} phonon couples preferentially with the A and B excitons, but report similar behavior for the A_{1g} and E_{2g}^1 modes at higher laser excitation energies.

With the recent possibility of producing two-dimensional TMD samples, a number of Raman studies of few-layer MoS₂ have been reported. It has been observed that the Raman spectrum is significantly dependent on the laser excitation energy (Terrones et al., 2014; Golasa et al., 2014; Fan et al., 2014; Sun et al., 2013; del Corro et al., 2014; Pimenta et al., 2015). Scheuschner et al. measured the REP of the A_{1g} phonon mode of 1L and

2L MoS₂ in the range of laser energies of the A and B excitons (1.75–2.05 eV) (Scheuschner et al., 2012), and observed that the amplitude of the REP associated with the B transition is larger than the A transition REP. It was also reported in this work (Scheuschner et al., 2012) that the amplitudes of the REPs are larger in bilayer than in monolayer MoS₂, suggesting that the electron-phonon coupling decreases with decreasing number of atomic layers. The enhancement of the A_{1g} mode under resonance with the A and B excitons was also observed in recent Raman studies of 1L and few-layer MoS₂ (Li et al., 2012a; Chakraborty et al., 2012), but detailed results using many different laser lines of higher energies were not reported in the previous resonance Raman studies of 2D MoS₂.

In this chapter, we present a resonant Raman spectroscopy study of MoS₂ samples of 1L, 2L, 3L and bulk using up to thirty excitation energies in the visible range. Our measurements allowed us to obtain separately the Raman excitation profile (REP) of the A_{1g} and E_{2g}¹ Raman bands. Our results confirm previous conclusions that the A_{1g} band resonates preferentially with the A and B excitons, but shows that the E_{2g}¹ band exhibits only resonance around 2.7 eV, which is ascribed to the coupling of this specific phonon with an exciton with different **k**-space characteristics (C exciton), recently predicted (Qiu et al., 2013).

Figure 4.1a–c show the optical image of 1L, 2L, 3L and bulk MoS₂ samples, obtained by mechanical cleavage (see chapter 3), studied in this thesis. The number of layers were identified by the frequency difference of the out-of-plane vibrational (A_{1g}) and the in-plane (E_{2g}¹) Raman modes collected at 514.5 nm, as reported by (Lee et al., 2010). For 1L-MoS₂ the $\Delta\omega$ is around 19 cm⁻¹ while its values increases to 21 cm⁻¹ for 2L-MoS₂, showing a strong thickness dependence as shown in Figure 4.1d,e.

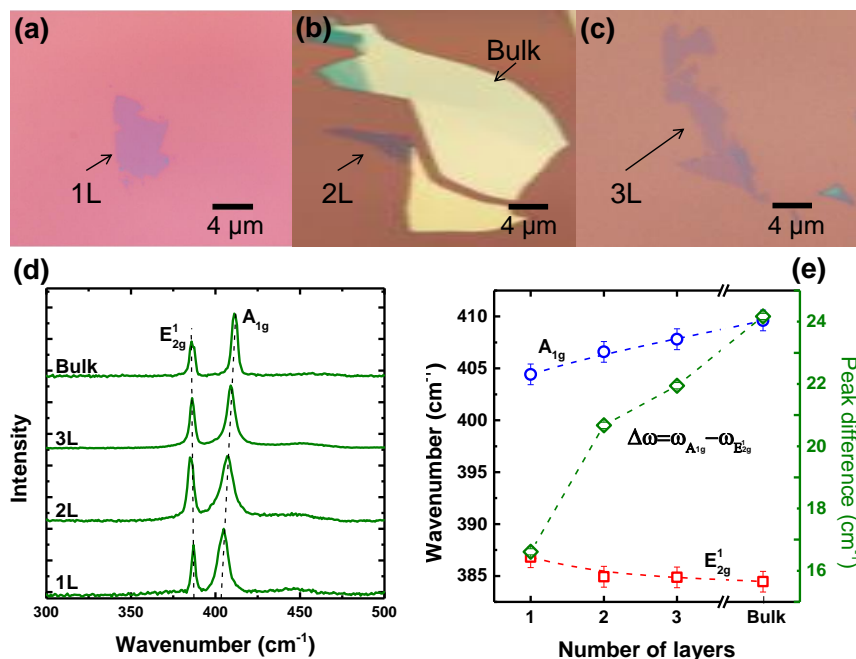


Figure 4.1: Exfoliated 1L-, 2L- 3L-MoS₂ and bulk samples studied in **this thesis**. (a–c) Optical images of mono-, bi- tri-layers and bulk MoS₂. (d) Raman spectrum of each samples shown in (a–c) recorded at 514.5 nm. (e) Identification of the number of layers by the frequency difference.

4.2 The first-order Raman modes in MoS₂: the exciton-phonon coupling

Figure 4.2 shows the Raman spectra of 1L, 2L, 3L and bulk MoS₂ obtained with many different laser excitation energies, in the 300–500 cm⁻¹ spectral range. The peaks around 387 cm⁻¹ and 410 cm⁻¹ correspond, respectively, to the in-plane E_{2g}¹ and the out-of-plane A_{1g} phonons (for notation simplicity, we will use the irreducible representations of bulk MoS₂) (Wilson and Yoffe, 1969; Molina-Sánchez and Wirtz, 2011). We can see in Fig. 4.2

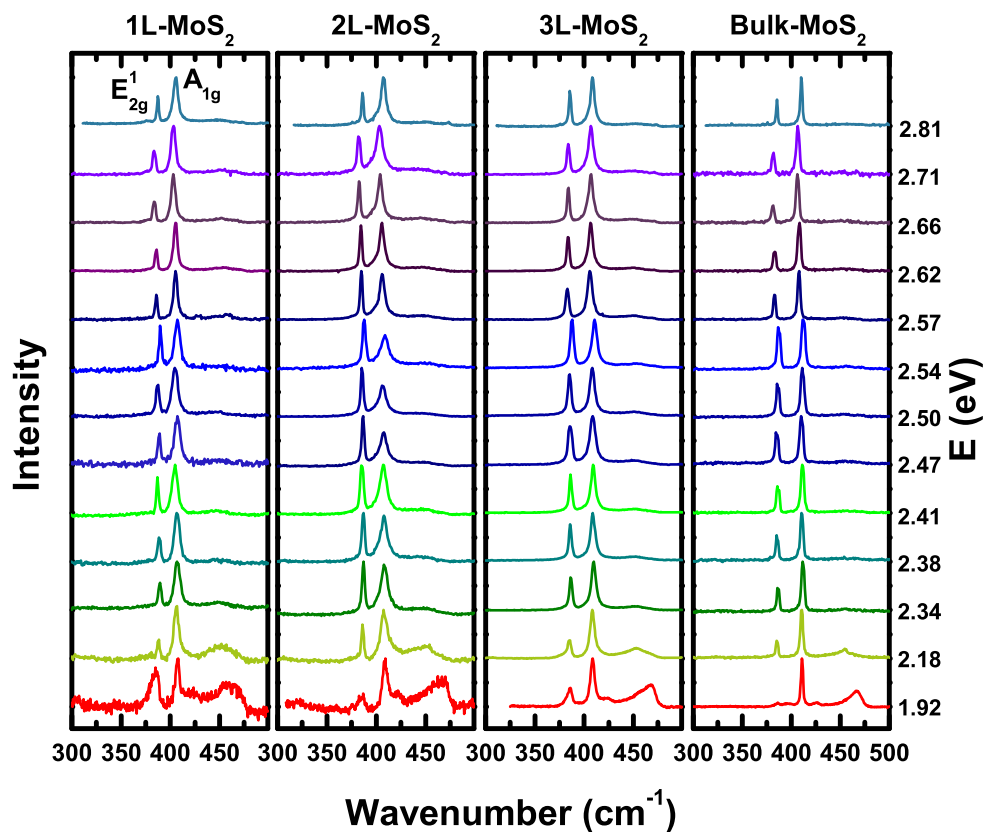


Figure 4.2: **Resonance Raman spectra of MoS₂**. Raman spectra of MoS₂ samples with different number of layers, and recorded with the different laser excitation energies shown in the right side. Panels from left to right correspond, respectively, to 1, 2 and 3 layers, and bulk samples. The Raman spectra have been normalized by the A_{1g} mode.

that the relative intensities of these modes are strongly dependent on the excitation energy. Both A_{1g} and E_{2g}^1 modes enhance for these laser energies. But, note that for some number of layers and laser excitation energy, the E_{2g}^1 mode is more intense than A_{1g} mode.

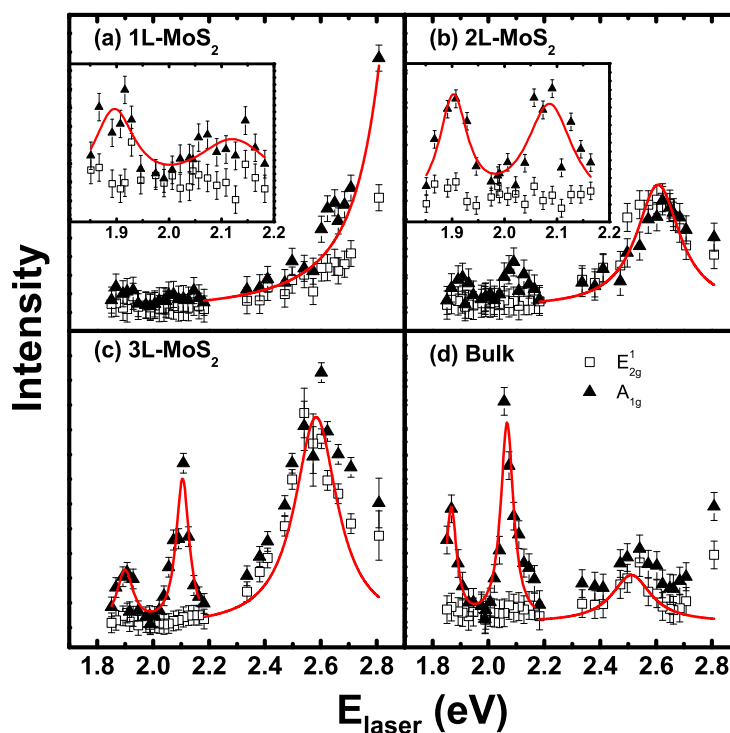


Figure 4.3: **The Raman excitation profile.** Raman excitation profiles of the E_{2g}^1 (open squares) and A_{1g} (solid triangles) Raman peaks in (a) monolayer, (b) bilayer, (c) trilayer and (d) bulk MoS_2 samples. The insets show a zoom-in of the data in the range 1.8-2.2 eV. The red curves represent the fitting of the experimental data by the expression given in Eq. (1). Here the data were properly normalized by the Si peak at 521.6 cm^{-1} and its cross-section.

In order to understand this effect in more details, Figure 4.3 shows the Raman excitation profile (REP) of the A_{1g} and E_{2g}^1 phonon modes for (a) 1L, (b) 2L, (c) 3L and (d) bulk MoS_2 samples. The intensities of the MoS_2

Raman peaks were normalized by the intensity of the Si Raman peak of the substrate, considering its excitation energy dependence as reported (Renucci et al., 1975), as described in the previous chapter.

The REP of the bulk sample, presented in Fig. 4.3(d) shows two maxima for the A_{1g} phonon mode (black triangles) around 1.9 and 2.1 eV, which are associated with the A and B excitonic transitions. The intensities of these two maxima decrease in the case of few-layer MoS_2 , and are very weak for the monolayer sample, as shown in Fig. 4.3(a). This result is in agreement with a previous resonance Raman study of this phonon in the region of the A and B excitons (Scheuschner et al., 2012). We can also see in Fig. 4.3 that the A_{1g} and E_{2g}^1 phonon modes are enhanced for all samples at higher laser excitation energies, around 2.7 eV.

The REP of the A_{1g} and E_{2g}^1 modes shown in Fig. 4.3 were fitted by the expression for the Raman intensity as a function of the laser energy E_L derived by a third-order time dependent perturbation theory (see equation (2.13) in chapter 2), and given by (Yu and Cardona, 2010):

$$I(E_L) = K \left| \frac{\langle f | H_{e-r} | b \rangle \langle b | H_{e-ph} | a \rangle \langle a | H_{e-r} | i \rangle}{(E_L - E_{ex} - i\gamma)(E_L - E_{ph} - E_{ex} - i\gamma)} \right|^2 \quad (4.1)$$

where $\langle f | H_{e-r} | b \rangle$, $\langle b | H_{e-ph} | a \rangle$, and $\langle a | H_{e-r} | i \rangle$ are the matrix elements associated with the electron-radiation, exciton-phonon and electron-radiation interactions, respectively, and E_{ex} is the energy of the intermediate excitonic state (A, B or C). The damping constant γ is related to the finite lifetime τ of the intermediate states, and E_{ph} is the corresponding phonon energy. The red curves in Fig. 4.3 correspond to the best fit of the experimental data, and Figures 4.4(a) and 4.4(b) show, respectively, the energy and damping constant values, as a function of the number of layers, obtained from the fitting of Fig. 4.3 by equation (4.1).

Let us now discuss the observed enhancement of the A_{1g} and E_{2g}^1

modes at 2.7 eV. The optical spectrum of bulk 2H-MoS₂ was measured more than forty years ago (Bromley et al., 1972; Beal et al., 1972) and, besides the sharp peaks ascribed to the A and B excitons, a broad band was also observed between 2.5 and 3.3 eV. This band was shown to exhibit two maxima around 2.76 and 3.18 eV, denominated respectively as C and D peaks. In these pioneer works, the C and D peaks were interpreted as optical transitions between high density of states regions at the **K** and **M** points of the 2D Brillouin zone. This high energy broad band was also observed in the optical spectra of atomically thin MoS₂ samples (Mak et al., 2010), and it was observed that its position blue shifts with decreasing number of layers.

In a resonance Raman study of bulk 2H-MoS₂ crystal, Sekine et al. showed that the A_{1g} mode REP exhibits two sharp peaks at 1.93 and 2.15 eV, and a broad peak at 2.61 eV (Sekine et al., 1980b). The sharp peaks were attributed to the A and B excitons and the broad peak to the direct band-to-band transition (Beal et al., 1972). The E_{2g}^1 peak was also observed to be enhanced in the region of the broad peak at 2.61 eV. Our results presented in Fig. 4.3 agrees with previous resonance Raman studies of MoS₂ in the range of the A and B excitons, but clearly shows that not only the A_{1g} , but the E_{2g}^1 mode is specially enhanced at higher laser energies. In order to show this effect more clearly, Fig. 4.5(a) plots the ratio between the intensities of the A_{1g} and E_{2g}^1 bands in a logarithmic scale, as a function of the laser excitation energy, for the different samples studied in this thesis. Points below (above) the horizontal red line correspond to enhancements of the A_{1g} (E_{2g}^1) modes.

In a recent first-principle calculation of the optical response of monolayer MoS₂ (Qiu et al., 2013), Qiu et al. showed that the broad band in the optical spectra between 2.5 and 3.3 eV has contributions of different types of excitons and excitonic states, which cannot be spectrally resolved at room-temperature. Besides the excited states of the A and B excitons

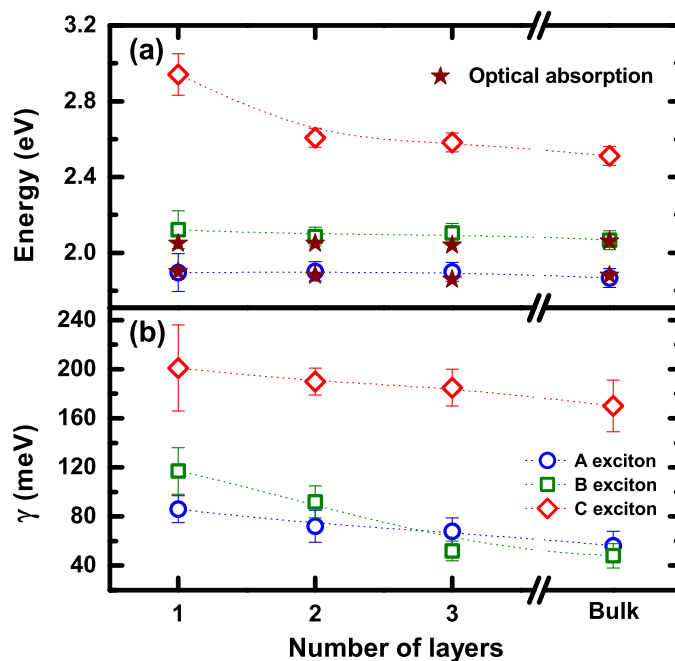


Figure 4.4: **Extracted phonon and finite lifetime of the exciton-phonon coupling in MoS₂.** (a) Energies and (b) damping constants of the A, B and C excitons for the samples with different number of layers. Red stars represent optical absorption values from (Mak et al., 2010) for 1L, 2L and 3L and from (Beal and Hughes, 1979) for bulk.

(A' and B'), it was also predicted the existence of a bound excitonic state with novel \mathbf{k} -space characteristics, called C exciton state.

Let us discuss if the enhancement of the A_{1g} and E_{2g}^1 phonon mode is due to the band-to-band transition, as proposed many years ago by Sekine et al. (Sekine et al., 1980b), or by a high energy excitonic transition predicted recently by Qiu et al. (Qiu et al., 2013). First, notice in Fig. 4.3 that the enhancement of both A_{1g} and E_{2g}^1 mode around 2.7 eV is stronger than the enhancement of them around 1.9 and 2.1 eV for monolayer MoS₂,

which are demonstrated to be associated with the A and B exciton states. When the intermediate state in a Raman process is excitonic, the Raman cross-section is enhanced more strongly than when the intermediate states correspond to band-to-band transitions (Kauschke et al., 1987; Limmer et al., 1990; Cardona and Güntherodt, 1982). Moreover, the Raman excitation profile of A_{1g} and E_{2g}^1 phonons around 2.7 eV for monolayer (see Fig. 4.3) is much sharper than the broad band in the optical spectra of MoS_2 . This result suggests that, among many excitonic states that contribute to the broad band in the optical spectra in the range 2.5-3.3 eV, both modes are selectively enhanced by a specific excitonic state. This selective enhancement is related by the exciton-phonon matrix element, given by the middle term in the numerator of equation (2.13), which depends on the phonon and the exciton symmetries.

This distinct exciton-phonon coupling can be explained considering the symmetries of the A_{1g} and E_{2g}^1 phonons and of the orbitals associated with the A, B and C excitons. According to (Qiu et al., 2013), the A and B excitons reflect the Mo d_{z^2} orbitals of the states in the lowest MoS_2 conduction band, and the exciton wave function is azimuthally symmetric, with the orbitals pointing along the z -direction [see Fig. 4.5(b)]. On the other hand, the C exciton is originated from a six-fold degenerate state made from transitions between the highest valence band and the first three lowest conduction bands near, but not directly at, the Γ point of the Brillouin zone (Qiu et al., 2013). When this exciton is plotted in real space, the electron has both Mo d_{z^2} and S p_x and p_y , with more S character near the hole. The representation of the orbitals the C exciton is shown in Fig. 4.5(c). The A_{1g} mode involves out-of-plane vibration of S atoms and, therefore, it is expected to modulate the d_{z^2} orbitals more strongly than the E_{2g}^1 in-plane mode. The situation is the opposite for the C exciton due to the presence of the in-plane p_x and p_y orbitals shown in Fig. 4.5(c). In this case, the in-plane movements of the S atoms modulate the electronic

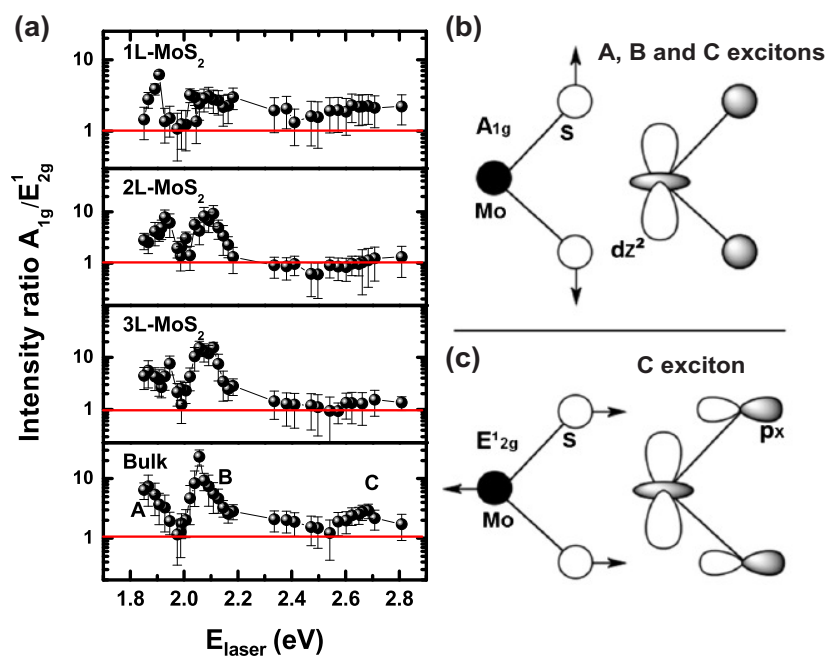


Figure 4.5: **Intensity ratio of the first-order modes.** (a) Ratio of the intensities of the A_{1g} and E_{2g}^1 Raman bands, plotted in a logarithmic scale. (b) Atomic displacements of the A_{1g} phonon mode and electronic orbitals of the A and B excitons. (c) Atomic displacements of the E_{2g}^1 phonon mode and electronic orbitals of the C exciton.

cloud and, therefore, one can expect a stronger exciton-phonon coupling for the E_{2g}^1 mode with the C exciton. Also, since the A_{1g} mode involves a totally symmetric vibration, it can also couple with the C exciton.

The symmetry-dependent exciton-phonon coupling can be also discussed using group theory arguments. For both few-layer and bulk MoS_2 , the d_{z^2} orbitals belongs the totally symmetric irreducible representation (A_1' , A_{1g} and A_{1g} for odd few-layer, even few-layer and bulk, respectively), whereas the p_x and p_y orbitals belong to a two-dimensional irreducible representation (E' , E_g and E_{2g} for odd few layer, even few layer and bulk, respectively). Therefore, the d_{z^2} orbitals couple mainly with the totally symmetric out-of-plane phonon (Wilson and Yoffe, 1969; Molina-Sánchez

and Wirtz, 2011), and the A_{1g} mode is enhanced by the A and B excitons. On the other hand, the two dimensional $p_{x,y}$ orbitals of the C excitonic state couple with the both two-dimensional out-of-plane and in-plane A_{1g} and E_{2g}^1 phonon (Wilson and Yoffe, 1969; Molina-Sánchez and Wirtz, 2011), explaining why it is enhanced by resonance with the C exciton. This is due to the fact that the C exciton is not exactly at the Γ point, but at six-fold points within the interior of the BZ [see section 1.4 and Figure 1.3(e)] (Qiu et al., 2013). Therefore, the exciton-phonon coupling between the C exciton with both first-order modes is indeed allowed by group theory. If the C exciton were located exactly at the Γ point, it would exhibit inversion symmetry and, as a consequence, such interplay would not be allowed.

Figure 4.4(a) shows that the values of the exciton energies obtained from our resonance Raman results do not depend significantly on the number of layers, within our experimental uncertainty. However, note that the C exciton energy which increases for the monolayer case, possibly due to the strong exciton-phonon coupling. Figure 4.4(a) also shows the A and B exciton energy values obtained from optical absorption experiments (Beal and Hughes, 1979; Mak et al., 2010), which are in a good accordance with our resonance Raman results. It is interesting to observe that the difference between the A and B exciton energies, which is related to the spin-orbit splitting (Coehoorn et al., 1987), is practically the same for few-layer and bulk MoS_2 (0.23, 0.18, 0.21, and 0.20 eV for 1L, 2L, 3L and bulk MoS_2 , respectively). The value for the bulk is in good agreement with that reported in (Coehoorn et al., 1987). Figure 4.4(b) shows that the damping constant γ of the A exciton increases significantly with decreasing number of layers. The γ constant of the B and C excitons increase slightly with decreasing number of layers. These results explain why the REP of the A_{1g} mode is smeared-out in the case of few-layer MoS_2 and why the A exciton REP is weaker than the B exciton REP (Scheuschner et al., 2012).

According to the theoretical calculation by Qiu et al. (Qiu et al., 2013),

the broad band observed by optical absorption has the contribution of different excitonic transitions. By symmetry arguments based on group theory, we show that the in- and out-of-plane E_{2g}^1 and A_{1g} modes couple with the C exciton. The slightly difference between the width of the resonance Raman profile and the broad band observed by other experimental techniques (Molina-Sánchez et al., 2013; Klots et al., 2014; Mertens et al., 2014; Liu et al., 2014), is due to the fact that, differently from Raman scattering, these techniques do not involve exciton-phonon interactions. Therefore our results allow distinction of the contribution of the C exciton from all other excitonic states.

4.3 Conclusion

To summarize, we have presented a resonance Raman study of 2D and bulk MoS₂ using thirty different laser lines in the range 1.85 to 2.81 eV, that allowed us to obtain the resonance Raman profile (REP) of the first-order A_{1g} and E_{2g}^1 phonon modes. We have shown that only the A_{1g} phonon mode is enhanced by the A and B excitons, but the enhancement decreases with decreasing number of layers, due to the dependence of the lifetime of the intermediate excitonic states on the number of layers. We also observed that the E_{2g}^1 phonon mode only enhances around 2.7 eV, in a region of the optical spectrum that exhibit a broad band associated with a diversity of excitons (Qiu et al., 2013). A group theory analysis shows that the high energy C exciton is the responsible for the enhancement of the E_{2g}^1 phonon mode, due to the symmetry-dependent exciton-phonon interaction in MoS₂. We comment that our findings have been confirmed by density functional theory by considering the Eliashberg functions (Molina-Sánchez et al., 2016), where the authors calculated the temperature-dependent excitons effects on the optical properties (Molina-Sánchez et al., 2016).

5 INTERVALLEY SCATTERING BY ACOUSTIC PHONONS IN 2D MoS₂ REVEALED BY DOUBLE-RESONANCE RAMAN SPECTROSCOPY

In this chapter, we exploit the concept of double-resonance process in monolayer and bulk MoS₂ through a multiple energy excitations Raman study in conjunction with density functional theory calculations. All the experimental data were collected in our Raman Laboratory at UFMG. The theoretical calculation was performed by the group at Pennsylvania State University. The defective sample was obtained through collaboration with a team at National Physical Laboratory. The results presented in this chapter was published in the journal **NATURE COMMUNICATIONS** 8, 14670 (2017).

5.1 Introduction

The second-order Raman spectrum of MoS₂ and other semiconducting transition-metal dichalcogenides (TMDs) hosts a rich variety of features, which are strongly dependent on the number of layers and the excitation laser energy (Chen and Wang, 1974; Stacy and Hodul, 1985; Frey et al., 1999; Golasa et al., 2014; Liu et al., 2015; Verble and Wieting, 1970; Lee et al., 2010; Chakraborty et al., 2013; Pimenta et al., 2015; Carvalho et al., 2015b). In the published works on two-dimensional (2D) MoS₂, the second-order Raman bands were probed using only few laser excitation lines, and results were interpreted based on phonon dispersion relations calculated from empirical force field models (Golasa et al., 2014). However, the use of multiple excitation energies is pivotal to unveiling the rich physical phenomena underlying the complex second-order Raman spectrum and the intervalley scattering processes in MoS₂.

Double-resonance Raman (DRR) is a special kind of second-order process that involves the resonant scattering of excited electrons by phonons, and can be used to study electrons, phonons, and their interplay (Martin and Falicov, 1983). By varying the incoming photon energy, the DRR condition selects different electronic states and different pairs of phonons with opposite finite momenta within the interior of the Brillouin zone (BZ) (Malard et al., 2009; Maultzsch et al., 2004; Carvalho et al., 2015a; Mohr et al., 2006; M. L. Bansal, 1991; Renucci et al., 1974; Cerdeira et al., 1972). For graphene, the most important DRR features, the D and 2D bands, provide rich physical information about the sample (Pimenta et al., 2007; Malard et al., 2009).

In this chapter, we unravel the origin of the DRR processes occurring in MoS₂ by investigating both experimentally and theoretically the Raman spectra as a function of the laser excitation. We measure the second-order bands using more than twenty different laser excitations ranging from 1.85 to 2.18 eV that densely cover the range of the A and B excitonic levels. Notably, we observe that the spectral positions of some specific second-order peaks depend on the laser excitation energy, which is characteristic of DRR processes. The experimental results are explained by accurate first-principles calculations, which are shown to be crucial for identifying of the different contributions to the DRR process. We show that some specific Raman processes are related to phonons near (but not at) the **M** and **K** points of the BZ. Moreover, the different contributions from the **M** phonons in monolayer and bulk reflect the crossover of the indirect-to-direct bandgap transition in the monolayer regime of MoS₂. Our work provides a fundamental explanation of the resonant behavior of the second-order Raman processes in MoS₂, involving different electronic valleys, and may also be applicable to the higher-order Raman spectra and to other semiconducting TMDs.

5.2 Experimental analysis

Figures 5.1a,b show the Raman spectra of monolayer (1L) and bulk MoS₂ in the 350–500 cm⁻¹ spectral range for three different laser energies (1.94, 2.04, and 2.11 eV). The two peaks around 388 cm⁻¹ and 407 cm⁻¹ are associated, respectively, with the first-order in-plane and out-of-plane Raman bands, with E' (E_{2g}¹ for bulk) and A₁' (A_{1g} for bulk) symmetries (Carvalho et al., 2015b; Ribeiro-Soares et al., 2014). All other features are contributions from different second-order processes.

A first-order Raman band can be fitted with a Lorentzian curve, since it arises from a single phonon at the center of the BZ. On the other hand, a second-order Raman band is given by the convolution of multiple two-phonon processes across the whole BZ and, in principle, cannot be fitted by a sum of Lorentzian curves. The determination of the lineshape requires a complete theoretical description of Raman intensities, including electron-phonon and electron-phonon coupling matrix elements. Nevertheless, the fitting of second-order bands in MoS₂ and other TMD compounds by a sum of Lorentzian curves has been widely used in the literature (Frey et al., 1999; Lee et al., 2010; Carvalho et al., 2015b; Golasa et al., 2014; Livneh and Spanier, 2015), because it provides a means to associate a feature in the spectrum with a specific phonon at a high-symmetry point within the BZ. Various works in the literature have fitted the second-order bands of MoS₂ with different numbers of Lorentzians, and given the resulting peaks different assignments (or when unassigned, different names) (Frey et al., 1999; Golasa et al., 2014; Livneh and Spanier, 2015). This fitting procedure can yield different peak numbers, positions, widths, and intensities (Malard et al., 2009; Carvalho et al., 2015b; Livneh and Spanier, 2015; Golasa et al., 2014). Here we also use this procedure, but we stress that it is only intended to provide a reliable estimate of the spectral position of the different contributions to the second-order Raman bands. The central goal of this work is to achieve a quantitative comparison

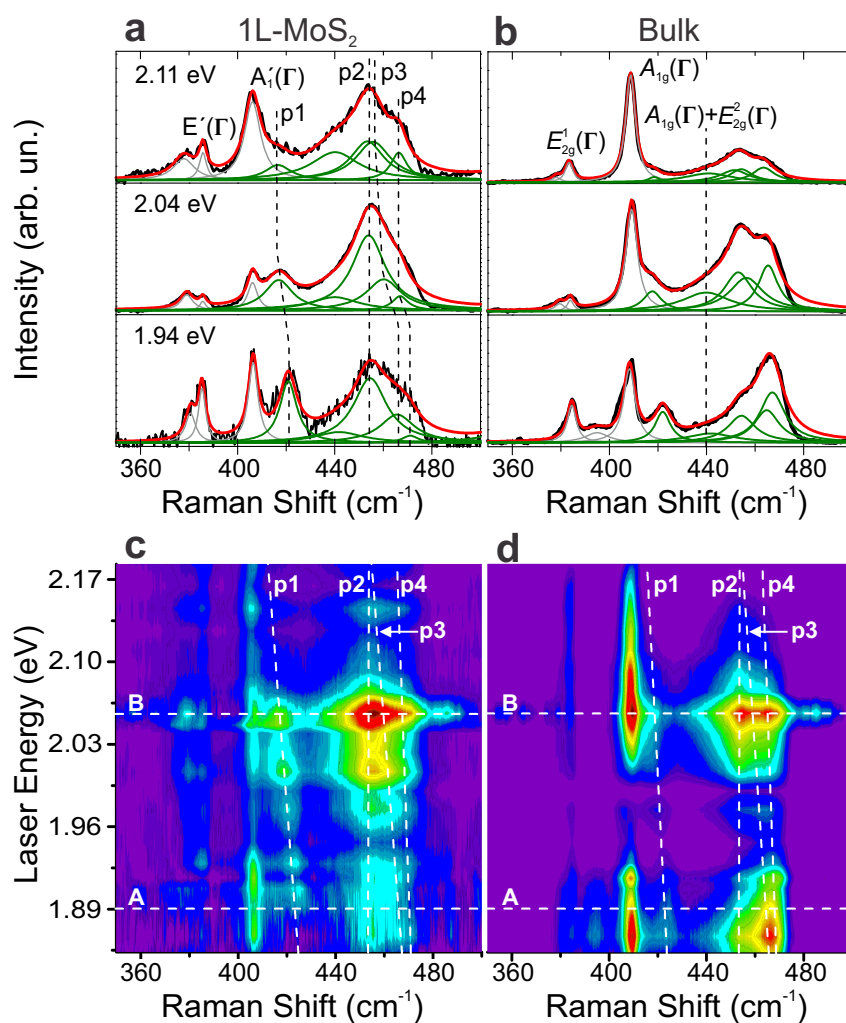


Figure 5.1: **Resonance Raman results on 1L and bulk MoS₂.** (a) and (b) Raman spectra of 1L and bulk MoS₂ measured with three laser excitation energies: 1.94 eV, 2.04 eV and 2.11 eV. The spectra are fit to a sum of Lorentzians (gray and green curves). The second-order bands studied here are denoted p₁, p₂, p₃ and p₄. (c) and (d) Resonant Raman maps with more than twenty different laser lines of 1L and bulk MoS₂ showing the enhancement of the Raman bands across the A and B excitons (horizontal dashed lines). The Raman spectra were normalized by the intensity of the Si peak at each excitation energy and, the Si Raman peak at 521.6 cm⁻¹ was used to calibrate the Raman shift.

between the measured and the calculated spectra within the entire spectral range considered here while making use of a dense sampling in terms of laser energies. We impose constant values for the full width at half maximum (FWHM) as a constraint in our Raman analysis, leaving intensity and position unconstrained. This procedure was adopted to decrease the number of fitting parameters, since the FWHM is not expected to depend significantly on the laser energy within this narrow range of energy (1.85–2.18 eV). The number of Lorentzian peaks is increased until a pre-defined convergence threshold is reached, and the results of this procedure are confirmed by first-principles calculations, as described below.

In Fig. 5.1a one observes a band at ca. 420 cm^{-1} that we call p_1 , and a broad and asymmetric band centered around 460 cm^{-1} , which is commonly called the 2LA band in the literature. In this thesis, this broad band was fitted by four Lorentzian peaks: a first peak around 440 cm^{-1} and the other three denoted by p_2 , p_3 and p_4 , as shown in Fig. 5.1a. The same number of peaks was used to fit the spectra of bulk MoS_2 , since more peaks were not found to be necessary to the fitting (in terms of convergence). This is possibly because the phonon branch splittings induced by interlayer interactions (Livneh and Spanier, 2015) are not larger than $\sim 3\text{ cm}^{-1}$ in MoS_2 (Molina-Sánchez and Wirtz, 2011).

Figure 5.1c,d show the multiple excitation Raman map for 1L and bulk MoS_2 obtained using more than twenty laser lines with energies from 1.85 to 2.18 eV. The horizontal scale represents the Raman shift, while the vertical scale is the laser excitation energy. We can observe the resonances of all Raman bands across the A ($\sim 1.89\text{ eV}$) and B ($\sim 2.06\text{ eV}$) excitonic transitions, which are marked by horizontal dashed lines. An important result is the dispersion of some Raman features as the laser energy changes, as clearly revealed by the dashed lines tracking Raman peak positions (Fig. 5.1a–d).

Each second-order band in the range $400\text{--}480\text{ cm}^{-1}$, measured with

different laser excitation energies, was fitted according to the same procedure used in Fig. 5.1a,b. The positions of p_1 , p_2 , p_3 and p_4 as a function of the laser excitation energy are plotted in Figure 5.2a,b for 1L and bulk MoS_2 , respectively. Notably, the position of the p_2 peak is unchanged for all laser energies, whereas p_1 , p_3 and p_4 red-shift as the laser excitation energy increases.

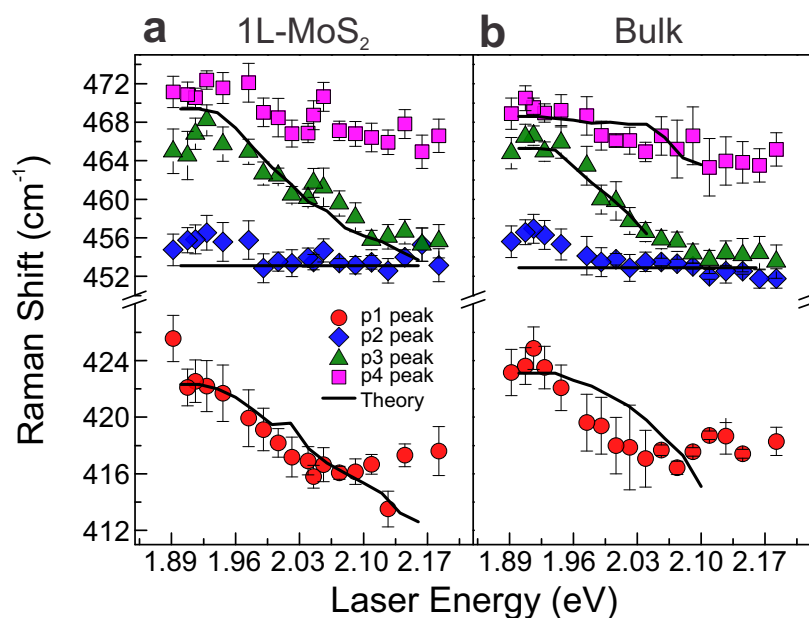


Figure 5.2: **Dispersive behavior of the second-order features on 1L and bulk MoS_2 .** (a) and (b) Laser energy dependence of the experimental values of the positions of the p_1 , p_2 , p_3 and p_4 peaks (symbols) of 1L and bulk MoS_2 , and the calculated dispersion of these peaks using equation 5.1 (solid curves). The absence of the theoretical curve of p_4 peak in (a) is due to its weak intensity not observable in the calculated Raman spectra (see Fig. 5.6). The error bars represent the standard error from the fitting process. The calculated phonon frequencies were shifted by within 1% to allow better comparison with the respective experimental dispersions.

5.3 Theoretical model

To explain the experimental results, we calculated the second-order Raman spectra for 1L and bulk MoS₂ within the single-particle picture, using the electronic structure and phonon dispersion obtained from density functional theory (DFT) (see Fig. 1.2) for different laser excitation energies.

We stress that in chapter 2, the Raman scattering theory was discussed considering the Feynman diagrams only for the one-phonon scattering process and noted that for a two-phonon process, the equation (2.13) needed to be extended to higher orders of the perturbation. In this chapter, we will describe the two-phonon process (*i.e.* DRR process) in a much easier way by considering the parabolic bands of a classical semiconductor (Yu and Cardona, 2010; García-Cristóbal et al., 1994).

Figure 5.3a shows a schematic representation of a DRR process in MoS₂, where the low-energy electronic structure is represented by parabolic bands at the BZ edges. The DRR process begins with an incoming photon creating an electron-hole pair of wave vector \mathbf{k} near the \mathbf{K} valley. The electron is then inelastically scattered by the emission of a phonon with branch index μ , wave vector $-\mathbf{q}$, and energy $\hbar\omega_{-\mathbf{q}}^{\mu}$ to the \mathbf{K}' valley. After that, the electron is inelastically scattered back to the \mathbf{K} valley by the emission of a second phonon with branch index ν , wave vector \mathbf{q} and energy $\hbar\omega_{\mathbf{q}}^{\nu}$, where the electron-hole pair recombines emitting a photon with energy $E_L - \hbar\omega_{-\mathbf{q}}^{\mu} - \hbar\omega_{\mathbf{q}}^{\nu}$ (Stokes scattering). At most two of these steps can be simultaneously resonant for a DRR process (Martin and Falicov, 1983; Malard et al., 2009; Maultzsch et al., 2004; Pimenta et al., 2015).

The intensity of a second-order Raman process is given by following expression:

$$I_{ee}^{PP}(E_L) = \left| \sum_{\mathbf{k}, \mathbf{q}, \mu, \nu} \frac{M_f \mathcal{M}_{cb} \mathcal{M}_{ba} M_0}{(E_L - E_{\mathbf{k}}^c + E_{\mathbf{k}}^v - \hbar\omega_{\mathbf{q}}^{\mu} - \hbar\omega_{\mathbf{q}}^{\nu} - i\frac{\gamma}{2})(E_L - E_{\mathbf{k}+\mathbf{q}}^c + E_{\mathbf{k}}^v - \hbar\omega_{\mathbf{q}}^{\mu} - i\frac{\gamma}{2})(E_L - E_{\mathbf{k}}^c + E_{\mathbf{k}}^v - i\frac{\gamma}{2})} \right|^2, \quad (5.1)$$

where M_0 , M_f are the matrix elements of the exciton-photon interactions for the incoming and outgoing photons, \mathcal{M}_{cb} , \mathcal{M}_{ba} represent the exciton-phonon interactions (García-Cristóbal et al., 1994), \mathbf{q} and \mathbf{k} are the wave vectors of the phonon and the electron, respectively, $E_{\mathbf{k}+\mathbf{q}}^c - E_{\mathbf{k}}^v$ are the energies of the intermediate state, and μ and ν denote the phonon branches involved in the process. The damping constant γ is related to the finite lifetime of the intermediate states, and $\hbar\omega_{\pm\mathbf{q}}^{\mu, \nu}$ is the corresponding phonon energy. In the present study, we only focus on two-electron processes (ee) involving transverse acoustic (TA) and longitudinal acoustic (LA) phonons; processes involving hole scattering (hh , eh and he), as shown in Figure 5.4, (Venezuela et al., 2011) were not taken into account for clarity and will be elaborated in future studies. The matrix elements are taken to be constants in the calculations.

Following the usual analysis for DRR in graphite (Cançado et al., 2002), the calculated DRR intensities are dominated by contributions from phonon wave vectors near $\mathbf{q} \sim 0$ and $\mathbf{q} \sim 2\mathbf{k}$ (distance from the \mathbf{K} point), as shown in Fig. 5.5. From this figure, we notice that, as the laser energy increases, the peak corresponding to $\mathbf{q} \sim 0$ is almost dispersionless and the peak corresponding to $\mathbf{q} \sim 2\mathbf{k}$ is dispersive. It has been reported for graphene (Jin et al., 2014; Li et al., 2013; Kaasbjerg et al., 2012) that the $\mathbf{q} \sim 0$ contribution vanishes due to the symmetry selections rules and quantum interference. We show later that, in the case of MoS_2 , this contribution, which is present in the DFT results, should vanish if excitonic effects are considered. For now, we only focus on the $\mathbf{q} \sim 2\mathbf{k}$ contribution by tracking the most dispersive Raman peaks in the calculated DRR intensities, since

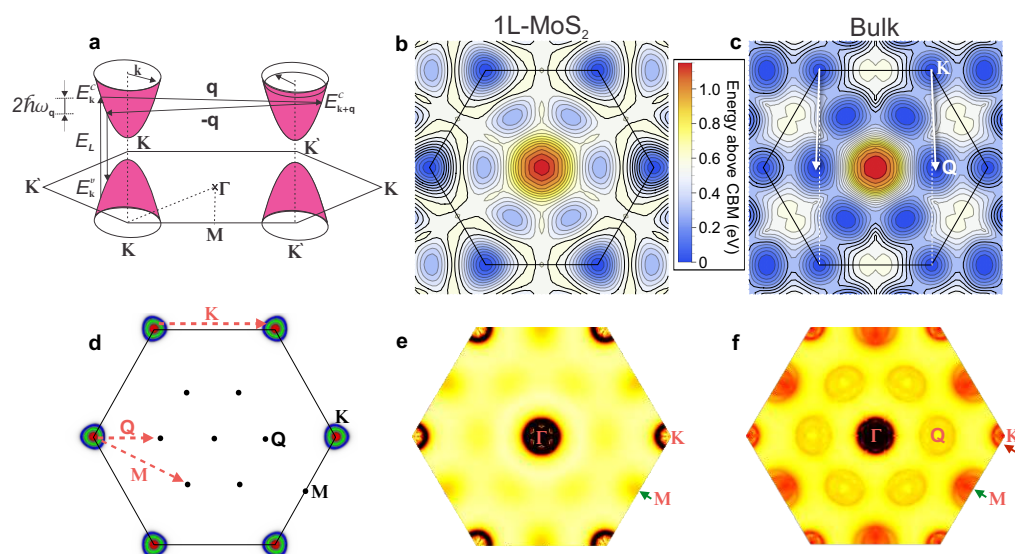


Figure 5.3: **Double-resonance Raman model.** (a) Representation of a DRR process where excited electronic states are connected by two phonons with opposite momenta \mathbf{q} and $-\mathbf{q}$. (b) and (c) Plot of the conduction bands for 1L and bulk MoS_2 , respectively. (d) Locus of electronic states that participate in the DRR Raman process around \mathbf{K} for laser energies of 1.9, 2.0, and 2.1 eV in red, green, and blue. Possible phonon wave vectors that connect these states with each other and with other high-symmetry points (\mathbf{M} and \mathbf{Q}) are shown as red dashed arrows. (e) and (f) Density of states of phonons that satisfy the DRR conditions for 1L and bulk MoS_2 , respectively. The DRR intensity in (e) and (f) is in arbitrary units justifying the use of no color bars.

the $q \sim 0$ contributions are almost dispersionless (other dispersionless features such as van Hove singularities can be identified separately from the phonon density of states, as shown later).

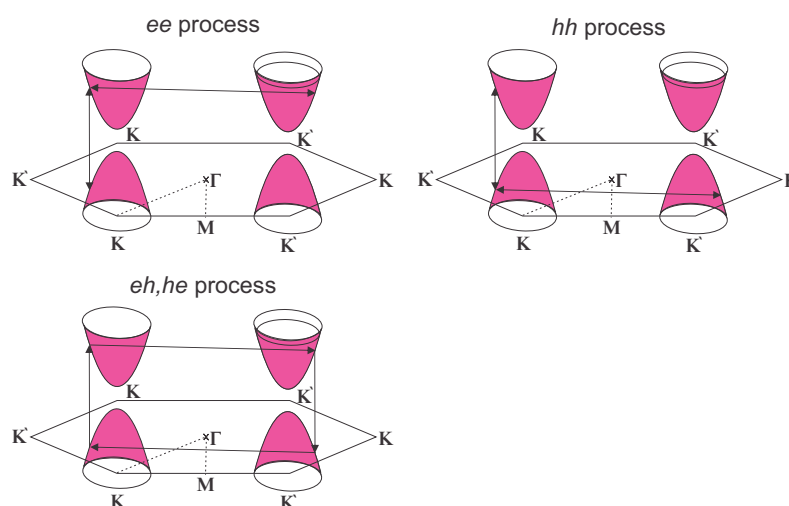


Figure 5.4: **Alternative representations of the DRR process.** Others customary representations of the DRR scattering process in MoS₂. The parabolic dispersion represent the electronic band structure near the **K** point. The vertical arrows represent the electron/hole creation and recombination. The horizontal arrows represent the scattering with a phonon or with a defect. The *ee* process is the same shown in Figure 5.3a. The other processes are referred to hole scattering (*hh*, *eh* and *he*).

Figure 5.3b,c show a contour map of the conduction electron energies for 1L and bulk MoS₂, where the conduction band minimum occurs at **K** for 1L MoS₂. Based on the calculated electronic structure, Fig. 5.3d shows three sets of electronic states that participate in the DRR process in 1L MoS₂, for laser excitation energies of 1.9, 2.0, and 2.1 eV, represented, respectively, in red, green, and blue. Similar to the case of graphene (Pimenta et al., 2007), when the laser excitation energy increases the locus of the on-resonance electronic states expands outward from **K**. Figure 5.3d

also shows that phonons that connect the pockets around \mathbf{K} and \mathbf{K}' valleys have wave vectors near \mathbf{K} , denoted $\mathbf{q}_{\sim\mathbf{K}}$ here (the symbol " \sim " means in the vicinity of the given high-symmetry point). On the other hand, pockets around \mathbf{K} and \mathbf{Q} points are connected by phonons near both the \mathbf{M} and \mathbf{Q} points, with wave vectors $\mathbf{q}_{\sim\mathbf{M}}$ and $\mathbf{q}_{\sim\mathbf{Q}}$, where \mathbf{Q} is another conduction band local minimum half-way between Γ and \mathbf{K} , as shown in Fig. 5.3b,c,d.

Figure 5.3e shows the on-resonance density of states for acoustic phonons that connect two pockets in the electronic structure at 2.0 eV excitation for 1L MoS₂. A high density of $\mathbf{q}_{\sim\mathbf{K}}$ phonons appears around \mathbf{K} and contributes strongly to the DRR scattering. A weaker density of phonons around \mathbf{M} also appears (green arrow in Fig. 5.3e). They originate from scattering between the \mathbf{K} and \mathbf{Q} valleys (see Fig. 5.3d). For 1L MoS₂, the intervalley scattering between \mathbf{K} and \mathbf{Q} only contributes weakly to the DRR process since the two minima are misaligned by 0.2 eV for 1L MoS₂.

The above procedure is also applied to bulk MoS₂, where the conduction band local minimum at \mathbf{Q} drops in energy, rendering the indirect band gap (Mak et al., 2010; Kormányos et al., 2013), as shown in Fig. 5.3c. Now, both $\mathbf{q}_{\sim\mathbf{K}}$ and $\mathbf{q}_{\sim\mathbf{M}}$ phonons in bulk MoS₂ contribute strongly to the on-resonance phonon density of states (red and green arrows in Fig. 5.3f), as well as the additional scattering channel between \mathbf{K} and \mathbf{Q} with phonon wave vector $\mathbf{q}_{\sim\mathbf{Q}}$ (see Fig. 5.3d).

Figures 5.6a–d show the calculated second-order Raman spectra for 1L and bulk MoS₂ for different laser energies, as given by equation (5.1), and using the phonon dispersion relations of the LA and TA phonons (see Fig. 1.2). In the range 405–420 cm⁻¹ (Fig. 5.6a,c), we observe one dispersive and one non-dispersive feature, and in the range 450–470 cm⁻¹ (Fig. 5.6b,d), one non-dispersive and two dispersive features at higher frequency. A normal second-order Raman band is non-dispersive, whereas a dispersive behavior indicates a DRR process. The positions of each feature in Figs. 5.6a–d as a function of the laser energy are also plotted in

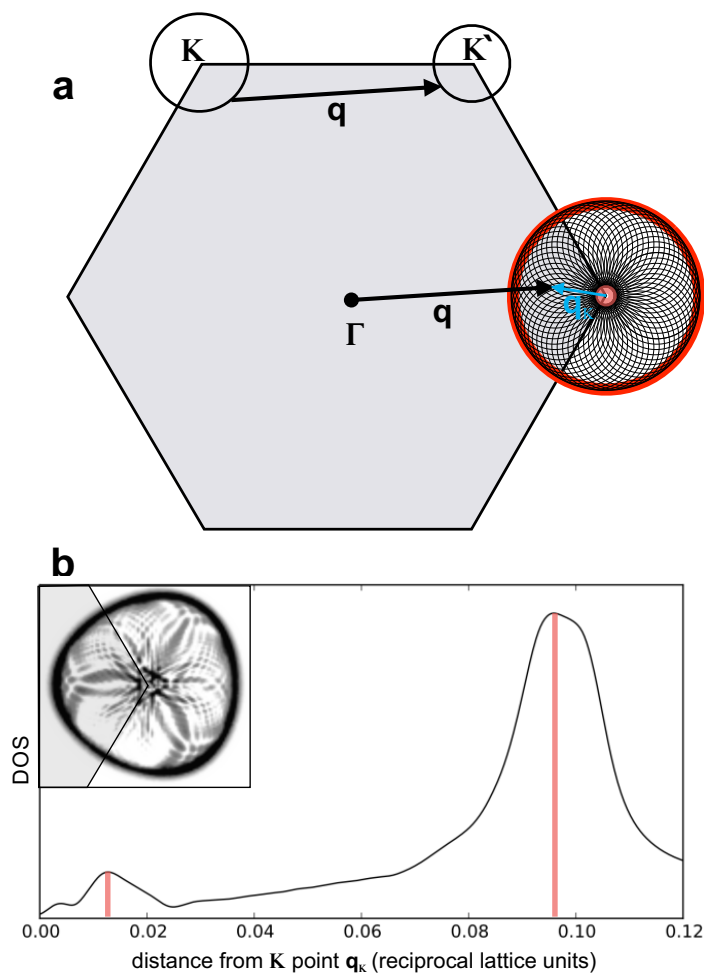


Figure 5.5: **Diagram of possible wave vector in intervalley scattering.** (a) The top diagram illustrates intervalley scattering via a phonon of wave vector q . The same phonon is translated to start from the Γ point (middle diagram) and the rings indicate the end points of all possible phonons connecting the two valleys. (b) The inset show the calculated ring patterns near the K point. The main plot shows the calculated DRR intensity as a function of distance from the K point.

Fig. 5.2a,b, for 1L MoS₂ and bulk, respectively, and represented by the black lines. The comparison between the experimental and calculated results in Fig. 5.2a,b shows an excellent agreement, and will allow for the

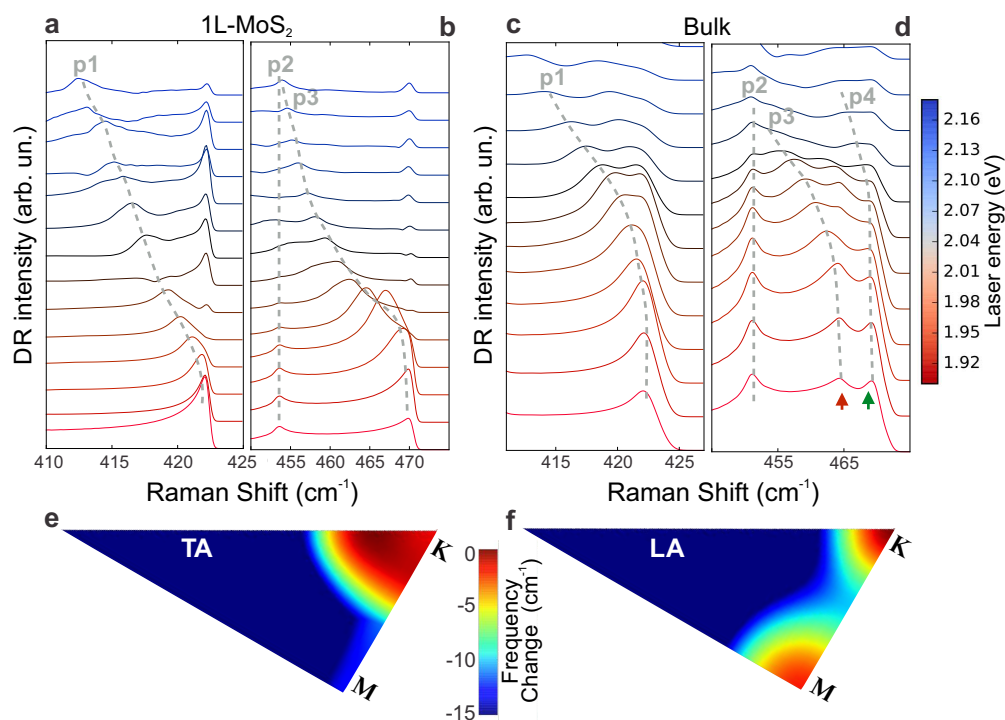


Figure 5.6: **Calculated resonance Raman spectra.** Calculated second-order Raman for (a, b) 1L and (c, d) bulk MoS₂ for different laser energies, using equation (5.1). All spectra are vertically shifted for clarity. (e, f) Calculated phonon frequencies of the TA and LA branches with respect to the frequency maxima of each branch, showing that the LA branch disperses more rapidly away from \mathbf{K} . In (a) and (b) since the absolute Raman shifts are prone to slight (1%) over/under-estimates due to limitations of DFT, the calculated phonon frequencies were shifted by within 1% to allow better comparison with the respective experimental dispersions. This shift leaves the calculated dispersion in the Raman shift with laser energy (which reflects the influence of the phonon and electron band structures on the DRR process) unchanged.

assignment of each second-order feature. As $\mathbf{q}_{\sim\mathbf{K}}$ expands away from \mathbf{K} , the frequency of on-resonance LA phonons would decrease with increasing laser energy due to the negative curvature of the LA branch dispersion near \mathbf{K} . Although p_4 is not clearly observable in the calculated DRR spectra for 1L MoS₂, a small contribution near $\sim\mathbf{M}$ can be seen in the BZ mapping of DRR intensity in Fig. 5.3e (green arrow). The underestimated intensity of this contribution from \mathbf{M} , compared with the experimental results (where the contribution from \mathbf{M} appears larger), might be due to strong electron-phonon coupling matrix elements between $\sim\mathbf{K}$ and $\sim\mathbf{Q}$ conduction valleys by an $\mathbf{q}_{\sim\mathbf{M}}$ phonon (Li et al., 2013) (matrix elements are treated as constants in this study).

5.4 Assignment of the second-order Raman features of MoS₂

The 2LA band

The strongest feature in the second-order spectrum of MoS₂ is the broad and asymmetric band centered around 460 cm⁻¹. In previous Raman studies of bulk MoS₂ (Chen and Wang, 1974), it was initially ascribed to the overtone of the longitudinal acoustic phonon at the \mathbf{M} point in the BZ and assigned to the 2LA(\mathbf{M}) band (Chen and Wang, 1974; Stacy and Hodul, 1985). However, its asymmetric shape led some authors to suggest that it could have contributions from other second-order processes. Verble and Wieting assigned the shoulder of the 2LA band at 466 cm⁻¹ to the Raman-inactive mode with A''_{2u} symmetry (or A_{2u} mode for bulk or even layers) at the Γ point (Verble and Wieting, 1970). Gołasa et al. suggested this band was composed by a combination of the optical E_{1g} phonon with the transverse acoustic (TA) phonon at the \mathbf{M} point (Golasa et al., 2014). Livneh and Spanier proposed different contributions for the 2LA band

in bulk MoS₂, such as the phonon density of states (pDOS), overtones of the **M** edge phonons from the acoustic (LA) and quasi-acoustic (LA') branches, which are very close in energy, and a weak contribution of the LA(**K**) phonons (Livneh and Spanier, 2015).

In this thesis, we assign the different contributions to the 2LA band by comparing the experimental and calculated multiple excitation Raman spectra of both 1L and bulk MoS₂. In our analysis, the 2LA band was fitted by four peaks, a peak around 440 cm⁻¹ and the peaks p₂, p₃, and p₄, as shown in Fig. 5.1a,b. The non-dispersive behavior of p₂ (see Fig. 5.2a,b) shows that it corresponds to a normal second-order Raman process. On the other hand, p₃ and p₄ exhibit a dispersive behavior, a signature of a DRR process (or higher-order resonant process) due to photons with different energies selecting electrons and phonons with different wave vectors in the BZ. Our calculations show that p₂ comes from the van Hove singularity (vHs) in the phonon density of states from a saddle point between **K** and **M**. The frequency of p₂ matches with twice the calculated frequency of the vHs. Our assignment for p₂ agrees with the conclusion reached by Livneh and Spanier (the L₂ peak in their work) (Livneh and Spanier, 2015). The 440 cm⁻¹ peak was recently ascribed to the combination mode A_{1g} + E_{2g}² at the Γ point (Livneh and Spanier, 2015). However, it can also be due to the asymmetric shape of p₂, since the vHs is not necessarily symmetric.

We next discuss the origin of the p₃ and p₄ peaks. Previous works assigned them to 2LA(**M**) and/or 2LA(**K**) processes, but the near-degeneracy of the LA phonon at **M** and **K** prevented a clear distinction between these two contributions (Chen and Wang, 1974; Stacy and Hodul, 1985; Frey et al., 1999; Golasa et al., 2014; Liu et al., 2015; Lee et al., 2015). A comparison of our results for 1L and bulk MoS₂ allows for an unambiguous assignment. As shown in Fig. 5.3f, the DRR process in bulk MoS₂ can support scattering by both $\mathbf{q}_{-\mathbf{M}}$ and $\mathbf{q}_{-\mathbf{K}}$ phonons, whereas DRR in 1L MoS₂ (Fig. 5.3e) is very weak for $\mathbf{q}_{-\mathbf{M}}$ phonons. The different DRR contributions from $\sim\mathbf{M}$

phonons in 1L and bulk MoS₂ allow us to distinguish the contributions of DRR $\sim\mathbf{K}$ and $\sim\mathbf{M}$ phonons to the second-order Raman band, as will be shown below. The calculated results in Figs. 5.6b,d show that p_4 clearly appears in the spectra of bulk MoS₂, but is very weak for 1L MoS₂. Notice that different from the calculated results, the experimental intensity of p_4 for 1L MoS₂ is weak but not negligible, this is possibly ascribed to the effect of a strong electron-phonon coupling of p_4 . However, the most relevant result is that p_4 is more intense than p_2 and p_3 for 2L, 3L and bulk MoS₂, and weaker for 1L MoS₂.

We, therefore, conclude that the p_4 peak is related to the scattering of the excited electron between the \mathbf{K} to the \mathbf{Q} valleys by two LA phonons near $\sim\mathbf{M}$ (see Fig. 5.3d). This leaves p_3 to be assigned to the scattering process between \mathbf{K} and \mathbf{K}' by two LA phonons in the vicinity of the \mathbf{K} point. Thus, a more precise assignment for p_3 and p_4 would be $2\text{LA}(\sim\mathbf{K})$ and $2\text{LA}(\sim\mathbf{M})$, respectively.

Figures 5.2a,b compare the experimental positions of p_3 and p_4 with their calculated dispersion. The excellent agreement between experiment and theory further confirms the assignment of p_3 and p_4 as $2\text{LA}(\sim\mathbf{K})$ and $2\text{LA}(\sim\mathbf{M})$. As the laser energy increases, p_3 and p_4 disperse at rates of -49 and $-21 \text{ cm}^{-1} \text{ eV}^{-1}$, respectively, and this result reflects the different slopes of the LA phonon dispersion near \mathbf{K} and \mathbf{M} of MoS₂. We thus conclude that the broad and asymmetric band centered around 460 cm^{-1} can be explained by contributions from LA phonons, instead of optical phonons (Verble and Wieting, 1970; Golasa et al., 2014). It has contributions from LA phonons near the saddle point between \mathbf{K} and \mathbf{M} (pDOS singularities) and from LA phonons near $\sim\mathbf{K}$ and $\sim\mathbf{M}$, which are enhanced in the spectra by the intervalley DRR process.

The p_1 (or b) peak

In a resonance Raman study of bulk MoS₂ at 7 K, Sekine et al. observed a band around 430 cm⁻¹ with a dispersive behavior near the A and B excitonic resonances, and called it the b band (Sekine et al., 1984). This band was ascribed to a two-phonon process involving a quasi-acoustic interlayer breathing mode and a transverse optical phonon (E_{1u}^2) both along the c-axis (Sekine et al., 1984). However, this band was also observed in more recent Raman studies of monolayer MoS₂ (Livneh and Spanier, 2015), thus ruling out the assignment suggested by these authors (Sekine et al., 1984). In a detailed multi-phonon study of bulk MoS₂, Livneh and Spanier suggested that the b band could involve combinations of the LA (or LA') and TA (or TA') phonons at the \mathbf{K} point (Livneh and Spanier, 2015).

In Fig. 5.2a,b we compare the experimental values of the p_1 positions (red circles) with the dispersion of the calculated peak (black curve) considering an intervalley DRR process involving one LA phonon and one TA phonon, in both time orders, in the vicinity of \mathbf{K} (see Figs. 5.6a,c). The combined energy of the relevant LA + TA phonons near $\sim\mathbf{K}$ red-shifts as the incident laser energy increases, dispersing at a rate of $-43 \text{ cm}^{-1} \text{ eV}^{-1}$. The agreement between the experimental and calculated results in Fig. 5.2a,b allows for the assignment of p_1 to LA($\sim\mathbf{K}$) + TA($\sim\mathbf{K}$).

The larger dispersion of $p_3 = 2\text{LA}(\sim\mathbf{K})$ than $p_1 = \text{LA}(\sim\mathbf{K}) + \text{TA}(\sim\mathbf{K})$ is consistent with TA phonons dispersing more slowly near \mathbf{K} than do LA phonons. This can be seen in Fig. 5.6e,f, which show the phonon dispersion for the TA and LA branches in the irreducible Brillouin zone, where the frequencies are represented by a color map. The LA phonon frequency rapidly decreases away from \mathbf{K} whereas the TA phonon frequency varies slowly near \mathbf{K} .

The 2LA(\sim Q) band

As represented in Fig. 5.3d, there are two different scattering processes between the **K** and **Q** electronic valleys, involving phonons with both wave vectors $\mathbf{q}_{\sim\text{M}}$ and $\mathbf{q}_{\sim\text{Q}}$. Indeed, the theoretical DRR maps in Fig. 5.3f predict the existence of a 2LA(\sim Q) band for bulk MoS₂ (see the red circle labelled \sim Q in Fig. 5.3f) at a frequency of 370 cm⁻¹. This band was not detected in our room-temperature spectra, presumably because the electron-phonon coupling matrix elements for this process are almost vanishing (Li et al., 2013). However, it was possibly observed in previous low-temperature studies in bulk MoS₂ (Sekine et al., 1984; Livneh and Spanier, 2015). Sekine et al. observed a weak feature around 380 cm⁻¹ in the spectra at 7 K, and ascribed it to the zone-center Raman-inactive E_{2u}¹ phonon (Sekine et al., 1984). Livneh and Spanier reported the existence of a band at 386 cm⁻¹, observed at 95 K, which could not be explained by their multi-phonon analysis (Livneh and Spanier, 2015). A multiple excitation Raman study at low temperatures will be necessary to confirm the existence of the double-resonance 2LA(\sim Q) band, and its possible dispersive behavior.

5.5 Disorder-induced DRR bands

As a further verification of our proposed DRR conclusions involving the acoustic phonons, the defect-induced resonant Raman spectra in 1L MoS₂ were measured. Figure 5.7a,b show the spectrum in the range 200–285 cm⁻¹, where we can observe defect-induced Raman features (Mignuzzi et al., 2015) for the excitation energy of 1.92, 2.06 and 2.14 eV. This process is similar to the disorder-induced D band in graphene (Pimenta et al., 2007), which also comes from a DRR process involving just one phonon, where momentum conservation is provided by elastic scattering of the excited electron by a defect (Malard et al., 2009; Pimenta et al., 2007, 2015). Notice that in the defective sample, the 2LA band broadens

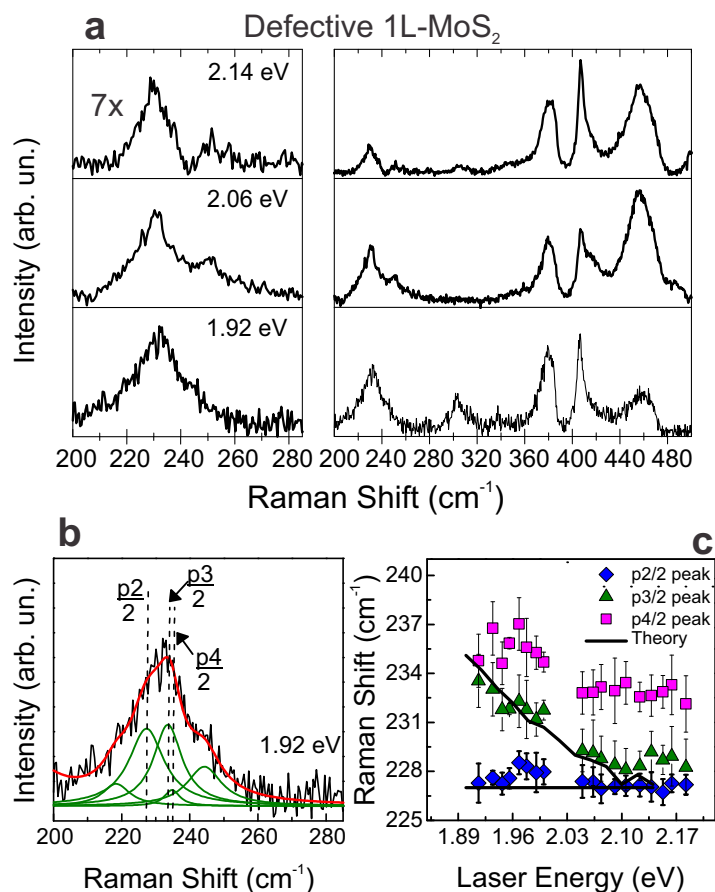


Figure 5.7: **Resonance Raman on defective 1L MoS₂.** (a) Raman spectra of defective 1L MoS₂ for three excitation energies (1.92, 2.06 and 2.14 eV). (b) Raman spectrum of a defective 1L MoS₂ sample, showing the disorder-induced bands associated with acoustic phonons near the edges of the Brillouin zone. Defects were created through bombardment with Mn⁺. The band was fit to a sum of Lorentzians with frequencies half the frequencies of p₂, p₃ and p₄. (c) Laser energy dependence of the experimental values of p₂/2, p₃/2 and p₄/2 (symbols) showed in (b), and the calculated dispersion of these disorder-induced peaks (solid curves) assuming one-phonon-defect DRR scattering. The absence of the theoretical curve of p₄ peak in (c) is due to its weak intensity not observable in the calculated Raman spectra. The error bars in (c) represents the standard error from the fitting process.

and decreases in intensity, which is expected since the disruption of the pristine lattice decreases phonon lifetimes and introduces new defective Raman bands. We have fitted the defect-induced Raman band with four Lorentzian peaks, similar to the procedure used for the 2LA second-order band in 1L pristine MoS₂. The frequencies of the three peaks at 227 cm⁻¹, 234 cm⁻¹ and 235 cm⁻¹ correspond respectively to one-half the frequencies of the p₂, p₃ and p₄ peaks as marked by the vertical dashed lines in Fig. 5.7b. Figure 5.7c shows the frequencies of these three Raman peaks as a function of the laser excitation energy, and the calculated dispersion of the DRR features considering now scattering by a phonon and a defect. The excellent agreement with the theory and experiment further supports the interpretation of the second-order DRR features, and highlights the intervalley elastic scattering by defects.

5.6 Excitonic effects

We now discuss the validity of the single-particle picture in the presence of excitonic effects. Single-particle DFT calculations have been extensively used in studying DRR processes in graphene, where excitonic effects are negligible at low excitation energies (Yang et al., 2009). Therefore, the strong excitonic effects in 1L MoS₂ call for further interrogation of assignments based on single-particle DFT results. Here, based on a simple two-band model, we show that the use of single-particle band structures (Fig. 5.8a,c) and exciton band structures (Fig. 5.8b,d) would yield similar laser-energy dependence of the Raman frequencies, thereby justifying the use of DFT eigenvalues in equation (5.1).

In the single-particle case, we model the low-energy band structure as parabolic bands $E_{\pm} = \pm(E_g/2 + \mathbf{k}^2/2m^*)$, where for convenience we assume that $m_e = m_h \equiv m^*$ is the mass of the electron and hole and that the conduction band has been rigidly shifted to bring the single-particle

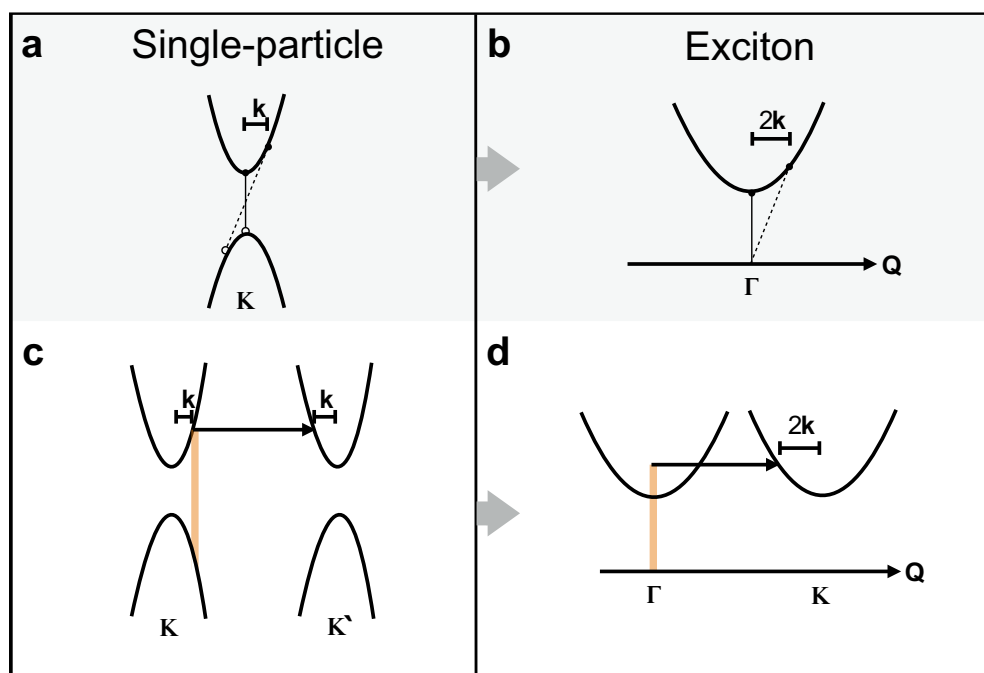


Figure 5.8: **Intervalley scattering as modelled using single-particle and excitonic band structures.** (a) In single-particle bands assuming (for convenience) equal effective masses m^* for electrons and holes, excitons can be represented by pairing electrons and holes with matching group velocities at $\mathbf{k}_e = -\mathbf{k}_h \equiv \mathbf{k}$, yielding an exciton with a center-of-mass momentum of $\mathbf{Q} = 2\mathbf{k}$. (b) The same excitonic states as shown in (a) are represented here in the exciton band structure whose band curvature is half that of the single-particle case, reflecting the exciton mass being $M = 2m^*$. Intervalley scattering can be represented either (c) between single-particle states or (d) between excitonic states. Given the same excitation energy $E_L = E_g + 2k^2/2m^*$, the on-resonance phonons in both systems are away from \mathbf{K} by $2\mathbf{k}$.

band-gap to match with the optical gap E_g . The actual electron-hole mass ratio calculated from different first-principles methods ranges from 0.8 to 1.8 (Qiu et al., 2013; Ramasubramaniam, 2012; Cheiwchanchamnangij and Lambrecht, 2012; Shi et al., 2013a).

From the single-particle bands, excitons can be approximately represented by pairing electrons and holes with matching group velocities at $\mathbf{k}_e = -\mathbf{k}_h \equiv \mathbf{k}$ (where \mathbf{k} is the wave vector measured from \mathbf{K}); such an exciton has a center-of-mass momentum of $\mathcal{Q} = 2\mathbf{k}$ and a total energy of $E_g + 2(\mathbf{k}^2/2m^*) = E_g + \mathcal{Q}^2/2M$. Thus we find $M = 2m^*$, *i.e.* the excitonic dispersion has half the band curvature of the single-particle bands. This is consistent with the semi-classical interpretation that the mass of an exciton is the sum of its constituents' masses. Momentum-resolved electron energy-loss spectroscopy measurements (Habenicht et al., 2015) are consistent with the exciton mass being larger than the constituent hole and electron masses obtained from first-principles calculations: 0.9–1.4 times their sum, depending on the exchange-correlation functional and pseudopotential used (note that the discussion below still applies, semi-quantitatively, for a reasonable range of exciton masses). Finally, we assume that the excitonic dispersion near $\mathcal{Q} = 0$ and $\mathcal{Q} = \mathbf{K}$ can be described by parabolic bands with the same band minimum and same curvature, since they both describe electron-hole pairs near the two degenerate valleys. That is, the energy difference of the two minima calculated by solving the tight-binding-based Bethe-Salpeter equation, 0.015 eV, is neglected here (Wu et al., 2015a).

We now discuss intervalley scattering between single-particle states and between excitonic states within the above assumptions, as depicted in Fig. 5.8c,d. When the laser energy is $E_L = E_g + 2\mathbf{k}^2/2m^*$, the on-resonance phonons in the single-particle bands are $2\mathbf{k}$ away from \mathbf{K} , as previously described. When the excitonic dispersion replaces the single-particle energies in equation (5.1), the resonance condition will be satisfied only if

the incoming photon matches the optical band gap, *i.e.* $E_L = E_g$, where excitons are scattered to $Q = \mathbf{K}$ and back. However, as the laser energy increases beyond the optical gap $E_L > E_g$ (but still within the exciton linewidth), a single and weaker resonance can still be achieved when the exciton is scattered to the other valley near $Q = \mathbf{K}$, and then back. The same laser energy as the one given in the single-particle system can be recast in terms of the exciton mass $E_L = E_g + 2\mathbf{k}^2/2m^* = E_g + (2\mathbf{k})^2/2M$. Hence the on-resonance phonons scattering excitons are also away from \mathbf{K} by $2\mathbf{k}$, the same as the single-particle case. Therefore, the excitation-energy dependence of the Raman frequencies (but not the intensities) can be reasonably well described by a single-particle electronic band structure, as both pictures give the so-called $\mathbf{q} \sim 2\mathbf{k}$ contribution of on-resonance phonons. We note that the $\mathbf{q} \sim 0$ contribution, which appears in the single-particle picture, is lost in the excitonic picture.

The single-particle results may also carry over to the many-body picture due to the presence of trions. Unlike neutral excitons with vanishing momenta, trions of finite momenta can be created where the momentum comes from the extra charge carrier. Thus, the momentum of this many-body state again depends on the laser excitation energy, and a dispersive behavior is expected.

Our conclusion that the LA(\mathbf{K}) phonon dominates the intervalley scattering is consistent with previous reports of valley depolarization in TMDs (Zeng et al., 2012; Mak et al., 2012; Kioseoglou et al., 2016). From the decay of the valley polarization with increasing temperature, Zeng et al. extracted the energy of the phonon mode dominating intervalley scattering to be 240 cm^{-1} , consistent with the LA(\mathbf{K}) phonon energy (Zeng et al., 2012). However, this thermal destruction of valley polarization could also originate from the excitonic levels shifting as a function of temperature, thus detuning the laser excitation energy from the A exciton energy (Mak et al., 2012). To rule out this possibility, Kioseoglou et al. performed depo-

larization measurements as a function of increasing pump laser energy at $T=5$ K, whereby the excess energy enables phonon-assisted intervalley scattering (Kioseoglou et al., 2016). These authors found that the destruction of the valley polarization occurs beyond an excess energy of 60 meV (≈ 480 cm⁻¹), which corresponds to two-LA(**K**) phonons, thus showing that intervalley scattering by LA phonons is responsible for depolarization (Kioseoglou et al., 2016).

5.7 Conclusion

To summarize, this chapter explains the origin of the double-resonance Raman (DRR) process in monolayer and bulk MoS₂, as involving different intervalley scattering processes. The resonant Raman spectra of the most intense second-order features in MoS₂ and the associated first-order disorder-induced bands, were measured using many laser excitation energies in the range of 1.85–2.18 eV, which covers the A and B excitonic levels. Experimental results are explained by density functional theory (DFT) calculations of the DRR scattering in monolayer and bulk MoS₂. We demonstrate that the use of multiple excitation energies is crucial for understanding the physical phenomena underlying the second-order Raman spectrum of MoS₂.

It was observed that the spectral position of some specific second-order peaks depends on the laser excitation energy, which is characteristic of DRR processes. By varying the incoming photon energy, the DRR condition selects different electronic states in the **K** and **Q** valleys, and different pairs of phonons with opposite finite momenta near (but not at) the **M** and **K** points of the BZ. Our results show that the DRR process reflects the indirect-to-direct bandgap transition from bulk to monolayer, and this effect allows the assignment of the Raman features to specific phonons near **M** or **K**.

This study can also be extended to explain the second-order Raman spectra and the double-resonance process in other semiconducting TMDs, such as MoSe_2 , WS_2 , WSe_2 . Moreover, the methodology in this thesis, based on multiple excitation Raman results and first-principle calculations, can also be used to explain the multiphonon spectra of semiconducting TMDs that exhibit a rich variety of high-frequency features, up to the fifth-order (Golasa et al., 2014; Livneh and Spanier, 2015; Berkdemir et al., 2013). Finally, it was shown that the second-order DRR spectra of MoS_2 originates in intervalley scattering by acoustic phonons, a mechanism which is also responsible for the destruction of valley polarization (*i.e.* depolarization) (Zeng et al., 2012; Kioseoglou et al., 2016). The results of this chapter are thus relevant for the field of valleytronics of MoS_2 , since the robustness of valley polarization depends sensitively on the absence of intervalley scattering (Zeng et al., 2012; Mak et al., 2012; Xiao et al., 2012).

6 CONCLUSION AND PROSPECT

This thesis investigated the electronic, optical and vibrational properties of MoS₂ using multiple laser excitation energies. At the first part, we have study the exciton-phonon coupling of mono- and few-layered MoS₂, where the laser excitation energy was continuously tuned across the excitonic transitions. We have demonstrated that the out-of-plane A_{1g} mode couples with the A, B and C excitons, whereas the in-plane E_{2g}^1 mode only combines with the C exciton. Both coupling only occurs due to the symmetry dependence between the phonons and the excitons' orbital symmetry (Carvalho et al., 2015b).

In the second part, we studied the most intense second-order Raman features of MoS₂. We observed that the frequency position of some of these features depends on the laser excitation energy, a clear characteristic of a double-resonance process. Therefore, similarly to the graphene's 2D band, by varying the incoming photon energy, the DRR mechanism selects electrons and phonons with different wave vectors, here at the **K** and **Q** valleys, and different pairs of phonons with opposite finite momenta near (but not at) the **M** and **K** points of the Brillouin zone. In addition, our findings show that the DRR process reflects the indirect-to-direct bandgap transition from bulk to monolayer MoS₂, and this effect allows the assignment of the Raman features to specific phonons near **M** or **K**. In particular, we have shown that the Raman band at around 420 cm⁻¹ is a combination of LA and TA modes at the **K** point. And, that the broadband around 460 cm⁻¹ is composed by a van Hove singularity (which is dispersionless) and by 2LA(\sim **K**) and 2LA(\sim **M**) (Carvalho et al., 2017). Our findings clarify a question opened for more than three decades on this material (Sekine et al., 1980b, 1984; Chen and Wang, 1974).

To conclude this thesis, we provide a few prospects for future studies on these two-dimensional transition-metal dichalcogenides. It is clear that

Raman spectroscopy has proven to be one valuable tool in the study of fundamental dynamics of exciton and phonon in TMDs. However, as Feynman once said *“There’s Plenty of Room at the Bottom”*. Many 2D materials are being discovered today and, more rich and exciting physics too. One route is to study the resonant Raman spectrum of beyond semiconducting TMDs, such as semi-metallic (MoTe_2 , WTe_2 , ReS_2 and ReSe_2) and superconductors (NbSe_2) TMDs. Also, their resonant behavior at low-temperature conditions. The dynamics of excitons and phonons in these kinds of TMDs are yet unclear.

Also, the possibility of study defects in 2D materials (hereafter, graphene and TMDs) by Raman spectroscopy need to take one step further on the route to identify the type of defect on the crystal lattice. It may be achieved through a combination of Raman spectroscopy and High-resolution transmission electron microscopy. Besides, the new valleytronic field, which permits to tune the valley degree of freedom in monolayer TMDs can also be investigated through Raman spectroscopy by tuning the laser energy near the exciton of a MoS_2 gate system.

In addition, each 2D material is like a Lego brick and, then they can be stacked. Thus, systems such as WS_2/MoS_2 , $\text{WS}_2/\text{MoSe}_2$, etc. and, also TMDs onto h-BN and graphene can provide new fundamental comprehension of the exciton and phonons dynamics. New Raman features may be originated from these stacked systems. Furthermore, how do exciton and phonon interact to each other? can the inter- and in-layer excitons be probed through Raman? How do the new Raman features originates and behaves? Answering this question may contribute to the development of the optical spectroscopy field using atomically thin 2D materials.

A ANGLE DEPENDENCE OF MoS₂

Here, we present a polarized Raman analysis showing the dependence of the two first-order modes of MoS₂ on the polarization direction of the incident and scattered light.

As already discussed in the thesis, 2H-MoS₂ belongs to the D_{6h} point group in the bulk form, and to the D_{3h} and D_{3d} point groups for odd and even N (number of layers), respectively. 2H-MoS₂ crystal shows four first-order Raman active modes, and their irreducible representations at the center of the Brillouin zone are:

$$\Gamma_{\text{Bulk}}^{\text{Raman}} = A_{1g} + E_{1g} + 2E_{2g}. \quad (\text{A.1})$$

The associated Raman tensors are given by (Loudon, 1964),

$$\begin{aligned} \overleftrightarrow{\mathbf{R}}(A_{1g}) &= \begin{pmatrix} a & 0 & 0 \\ 0 & a & 0 \\ 0 & 0 & b \end{pmatrix}, \\ \overleftrightarrow{\mathbf{R}}(E_{2g})_x &= \begin{pmatrix} 0 & d & 0 \\ d & 0 & 0 \\ 0 & 0 & 0 \end{pmatrix}, \quad \overleftrightarrow{\mathbf{R}}(E_{2g})_y = \begin{pmatrix} d & 0 & 0 \\ 0 & -d & 0 \\ 0 & 0 & 0 \end{pmatrix}, \\ \overleftrightarrow{\mathbf{R}}(E_{1g}) &= \begin{pmatrix} 0 & 0 & 0 \\ 0 & 0 & c \\ 0 & c & 0 \end{pmatrix}, \quad \begin{pmatrix} 0 & 0 & -c \\ 0 & 0 & 0 \\ -c & 0 & 0 \end{pmatrix}. \end{aligned} \quad (\text{A.2})$$

Chen *et al.* identified the assignment of these modes in 2H-MoS₂ crystals (Chen and Wang, 1974). It was observed that the two main first-order peaks at 383 cm⁻¹ and 408 cm⁻¹ correspond to the E_{2g}¹ and A_{1g} modes, respectively. Both modes are observed in the YY and XY configurations, but

A_{1g} mode almost disappears in the XY configuration. The E_{1g} mode appears at 286 cm^{-1} in the XZ and YZ configuration spectra but it is forbidden in the common back-scattering experiments (XX and XY configuration). The so-called rigid-layer, E_{2g}^2 mode appears only at very low-frequency, at around 32 cm^{-1} .

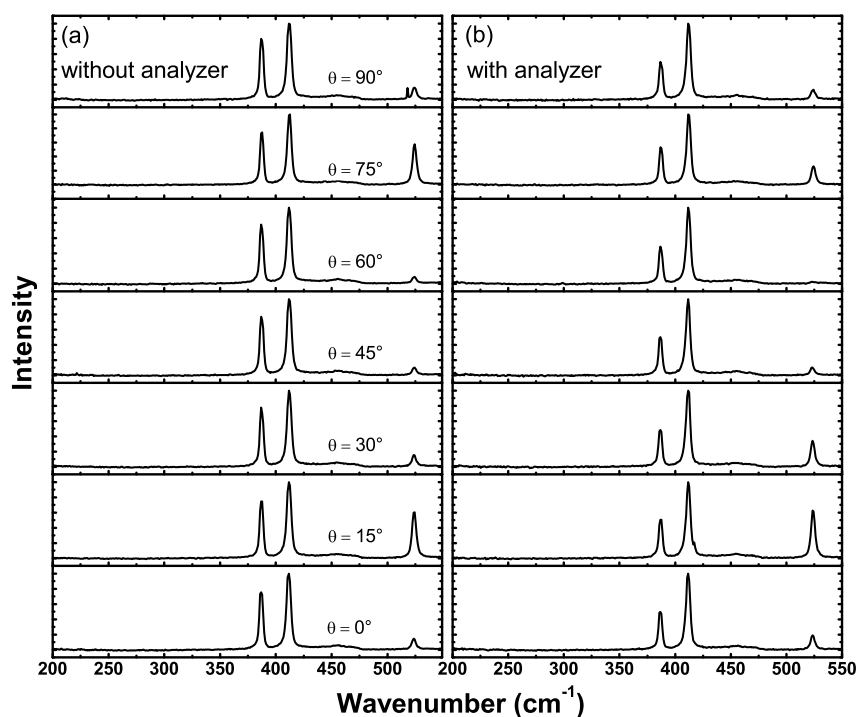


Figure A.1: **Polarized Raman spectra.** Raman spectra of bulk MoS_2 sample with different angles (a) without and (b) with analyzer recorded at 488 nm (2.54 eV) laser excitation energy.

Figure A.1 shows the angular dependence of the polarized Raman spectra, using an analyzer parallel to the incident light polarization [Fig. A.1b] and without using an analyzer [Fig. A.1a]. In both cases, the intensities of the E_{2g}^1 and A_{1g} bands are independent of θ when θ varies from 0° to

90°, showing that the results presented in Chapter 4 are independent of the sample orientation. The polarization measurements were performed using the 488 nm (2.54 eV) laser excitation wavelength. Notice that the E_{1g} mode does not appear in the Raman spectra around 286 cm^{-1} [Fig. A.1a,b] showing that our set-up is well approximated by a back-scattering geometry.

Let us now discuss the theory of the polarized Raman analysis. The Raman intensity scattering is proportional to $|\hat{e}_i \overset{\leftrightarrow}{R} \cdot \hat{e}_s|^2$, where \hat{e}_i and \hat{e}_s represent the polarization vectors of the incoming and scattered light, respectively, and $\overset{\leftrightarrow}{R}$ is the Raman tensor given in equation (A.2).

The polarized Raman experiment can be performed by (i) rotating the polarization while keeping the sample fixed and (ii) rotating the sample while keeping the polarization fixed. Evidently, both procedures must give the same intensity, but we consider the second case which is preferred in polarized Raman experiment.

First, let us consider the experimental scattering geometry where the polarization of the incident and scattered light are parallel and given by: $\hat{e}_i = \hat{e}_s = (\cos\theta, \sin\theta, 0)$. The intensity of E_{2g}^1 mode is given by,

$$I_{E_{2g}^1} = I_{E_{2g}^1}^x + I_{E_{2g}^1}^y \propto \left| \begin{pmatrix} \cos\theta & \sin\theta & 0 \end{pmatrix} \begin{pmatrix} 0 & d & 0 \\ d & 0 & 0 \\ 0 & 0 & 0 \end{pmatrix} \cdot \begin{pmatrix} \cos\theta \\ \sin\theta \\ 0 \end{pmatrix} \right|^2 + \left| \begin{pmatrix} \cos\theta & \sin\theta & 0 \end{pmatrix} \begin{pmatrix} d & 0 & 0 \\ 0 & -d & 0 \\ 0 & 0 & 0 \end{pmatrix} \cdot \begin{pmatrix} \cos\theta \\ \sin\theta \\ 0 \end{pmatrix} \right|^2 \propto d^2. \quad (\text{A.3})$$

The intensity for the A_{1g} mode is,

$$I_{A_{1g}} \propto \left| \begin{pmatrix} \cos \theta & \sin \theta & 0 \end{pmatrix} \begin{pmatrix} a & 0 & 0 \\ 0 & a & 0 \\ 0 & 0 & b \end{pmatrix} \cdot \begin{pmatrix} \cos \theta \\ \sin \theta \\ 0 \end{pmatrix} \right|^2 \propto a^2. \quad (\text{A.4})$$

Therefore, when the polarization angle θ varies from 0° to 90° , both $I_{E_{2g}^1}$ and $I_{A_{1g}}$ do not depend on θ and the intensity ratio between E_{2g}^1 and A_{1g} remains constant.

Next, we consider a situation without using an analyzer. The experimental scattering geometry corresponds to the polarization vector set: $\hat{e}_i = (\cos\theta, \sin\theta, 0)$ and $\hat{e}_s = (\cos\phi, \sin\phi, 0)$, but now we need to integrate over the scattered angle ϕ . The intensity of E_{2g}^1 and A_{1g} modes are,

$$\begin{aligned} I_{E_{2g}^1} &\propto d^2 \left(\cos^2\theta \int_0^\pi \sin^2\phi d\phi + \sin^2\theta \int_0^\pi \cos^2\phi d\phi + \cos^2\theta \int_0^\pi \cos^2\phi d\phi + \sin^2\theta \int_0^\pi \sin^2\phi d\phi \right) \propto d^2 \\ I_{A_{1g}} &\propto a^2 \left(\cos^2\theta \int_0^\pi \cos^2\phi d\phi + \sin^2\theta \int_0^\pi \sin^2\phi d\phi + 2 \cos\theta \sin\theta \int_0^\pi \cos\phi \sin\phi d\phi \right) \propto a^2. \end{aligned} \quad (\text{A.5})$$

Here again, the intensities are also independent of the angle θ . Therefore, we conclude that the polarized Raman results are isotropic in the xy plane of the spectra, using an analyzer parallel to the incident light polarization and without using an analyzer. We comment that only parallel polarization was considered here, in the case where we would have cross-polarization it is expected that the A_{1g} mode to disappear.

B ULTRASENSITIVE MOLECULAR SENSOR USING N-DOPED GRAPHENE THROUGH ENHANCED RAMAN SCATTERING

In this appendix, a highly sensitive chemical sensor based on Raman spectroscopy and using nitrogen-doped graphene as a substrate is presented. Here, nitrogen atoms were introduced into the carbon structure of graphene doping the material. This work was developed during the doctoral internship at the Pennsylvania State University, and published in the journal *SCIENCE ADVANCES* 2 (7), E1600322 (2016).

Introduction

The surface-enhanced Raman scattering (SERS) effect has become an important technique to detect trace amounts of molecules (10^{-5} to 10^{-12} M) (Burstein et al., 1979; Fleischmann et al., 1974). The SERS effect comes from two major mechanisms: (i) an intense electromagnetic field (EM) generated by plasmon resonance located close to the metallic structure (Hao et al., 2011) and (ii) a chemically enhanced mechanism (Morton and Jensen, 2009) through a charge transfer between the probe molecules and the substrate. Traditionally, SERS substrates are based on a roughened surface of a noble metal (for example, Ag and Au), which provides the plasmons for the EM mechanism to occur. However, this enhancement efficiency varies from metal to metal and largely depends on the SERS substrate fabrication process, which is relatively complex, hard to control, and difficult to keep clean. In addition, metals are usually easily oxidized and are not biologically friendly, which further limits their application in diverse fields. Recently, pristine graphene (PG) has been proven to be an excellent substrate to enhance the Raman signal of molecules (Ling

et al., 2010), giving rise to the expression “graphene-enhanced Raman scattering” (GERS). In addition, it can effectively quench the molecules’ spectral fluorescence background (Xie et al., 2009). Because of its chemical inertness and good biocompatibility, graphene is very attractive as an efficient metal-free substrate for probing trace amounts of organic molecules. To unveil the GERS mechanism of graphene, several theoretical and experimental studies have been carried out (Barros and Dresselhaus, 2014; Ling et al., 2015). Ling et al. have shown that the enhancement strongly depends on the configuration of the molecule on a graphene substrate, the so-called “first-layer effect”. It implies that the Raman scattering of the first adsorbed layer of the probe molecules on a graphene substrate will be especially enhanced over that of the subsequent layers (Ling et al., 2012b; Ling and Zhang, 2010). Later on, Xu et al. further demonstrated that the enhancement of the Raman signal can be modulated by tuning the graphene’s Fermi level (E_F) via a graphene-based field effect transistor device (Xu et al., 2011a,b). Moreover, to explain the GERS mechanism on different neutral molecules, Huang et al. probed molecules with different symmetries and concluded that the enhancement of a molecule’s Raman signal occurs if the highest occupied molecular orbital (HOMO) and the lowest unoccupied molecular orbital (LUMO) levels of that given molecule sit on a suitable energy range with respect to the E_F of graphene (Huang et al., 2015). In this context, our recent work has demonstrated that, compared with PG, substitutional doping of graphene with heteroatoms (for example, nitrogen and silicon) leads to substrates that can remarkably enhance the GERS effect (Lv et al., 2014, 2012).

Here, large-area monolayer PG and nitrogen-doped graphene (NG) were synthesized on Cu foils using methane (CH_4) and ammonia (NH_3) as precursors in an ambient pressure chemical vapor deposition (AP-CVD) system (Lv et al., 2012). We observed that, by tuning the synthesis parameters, the doping levels of NG are also tuned. A striking point lies

on the nitrogen doping configuration control within the graphene lattice when varying the synthesis conditions. For example, single substitutional doping (N_1) or double substitutional doping (N_2^{AA}) can be controlled and identified by Raman spectroscopy and scanning tunneling microscopy (STM). In addition, as-synthesized NG and PG sheets were also used as substrates to probe different fluorescent molecules and to explore the GERS mechanism. For example, we observed a consistent trend that NG leads to a better Raman signal enhancement of the studied fluorescent dye molecules [for example, rhodamine B (RhB), crystal violet (CRV), and methylene blue (MB)] when compared to PG. Through experimental and theoretical studies, we demonstrate here that the LUMO alignment with the E_F of NG is closely related to the enhancement of the Raman signal of the studied molecules. We also noted that this enhancement depends strongly on the excitation of the photon energy and the doping level of the graphene. Some signals from these dye molecules can be detected even for concentrations as low as 10^{-11} M, which provides excellent molecular sensing capabilities. Ab initio calculations were carried out to investigate a possible chemical mechanism of GERS. The results are consistent with a mechanism involving a charge-transfer excitation, which is described below.

The nitrogen-doped graphene

Large-area monolayer PG and NG sheets were synthesized on copper foils using CH_4 and NH_3 as precursors in conjunction with an AP-CVD system. Details of the synthesis procedure can be found in a previous report (Lv et al., 2012). A typical NG sheet on copper foil looks like bare copper because of graphene's high transparency. Synthesized NG can be transferred onto other materials, such as SiO_2/Si and quartz substrates by using polymethyl methacrylate (PMMA)-assisted transfer method (Reina

et al., 2009), and good transparency and homogeneity can be observed. Figure B.1A and B.1B show high-resolution transmission electron microscopy (HRTEM) images of monolayer and bilayer NG sheets transferred to TEM grids via PMMA-free methods (Regan et al., 2010). The inset of Fig. B.1A shows the corresponding selected-area electron diffraction pattern of an NG sheet, confirming the hexagonal structure of graphene. Less than 8% of the NG material consists of few layers (for example, bilayer or trilayer), revealing an interlayer spacing of ~ 0.35 nm (Fig. B.1B) (Delhaes, 2000).

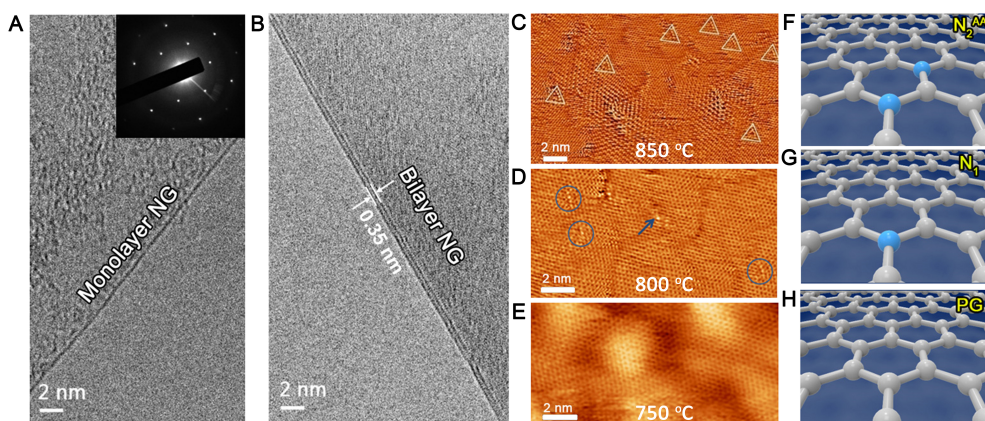


Figure B.1: HRTEM and STM images of as-transferred NG. (A and B) HRTEM images of monolayer and bilayer NG sheets on TEM grids. The inset of (A) is the corresponding selected-area electron diffraction pattern of NG. (C to E) Typical STM images of NG sheets synthesized using different doping parameters: (C) NH_3 , 850°C ; (D) NH_3 , 800°C ; and (E) NH_3 , 750°C . (F and G) Models of (F) N_2^{AA} and (G) N_1 nitrogen doping configurations. (H) Model of PG without any nitrogen doping. The triangles in (C) and the circles in (D) indicate the STM double N substitution configuration, and the arrow in (D) indicates the STM single N substitution.

First, control experiments were carried out to study the mechanism of nitrogen doping of graphene by tuning the temperature at which NH_3 is introduced during the synthesis reaction (from 950° to 750°C) and its

reaction time (from 10 to 60 min) while keeping the CH_4 reaction time and temperature constant (that is, 980°C for 30 min). The Raman spectra of NG on SiO_2/Si substrates for different synthesis conditions are shown in fig. B.2A and B.2B. Both the intensity ratio between the 2D and G bands (I_{2D}/I_G) and the sharpness of the 2D band confirm the growth of NG (Malard et al., 2009; Ferrari et al., 2006). When comparing NG to PG, we notice the emergence of a D band in our as-grown NG sheets, which can be attributed to the disorder generated by the introduction of nitrogen atoms within the graphene lattice (Ferrari et al., 2006; Yu et al., 2011a). The average distance between defects in graphene can be obtained by considering the intensity ratio between the D and G bands (Jorio et al., 2010; Lucchese et al., 2010). Note in fig. B.2A and B.2B that the intensity ratio of I_D/I_G significantly changes when the NH_3 reaction temperature and reaction time are changed, whereas the 2D band remains sharp and symmetric. Therefore, it is possible to tune the experimental conditions and achieve doping control over NG. A detailed Raman characterization analysis also suggests that there might be a competition between the N incorporation into graphene sublattices and the annealing process (fig. B.2B) when the NH_3 reaction time changes from 10 to 60 min. It is also noteworthy that the I_D/I_G values initially increase, thus suggesting more nitrogen doping, but such values decrease for reaction times beyond 30 min.

Figure B.1C–E show STM results for samples obtained using different synthesis parameters (850° , 800° , and 750°C , respectively). The results confirm the tuning of the doping level. In a previous work, it was reported that the NG sample synthesized at 850°C for 10 min in the presence of NH_3 shows a unique double substitutional N doping ($\text{N}_2^{\text{A}\text{A}}$), as can be seen in the triangles shown in Fig. B.1C (Lv et al., 2012). Figure B.1F shows a model image of the $\text{N}_2^{\text{A}\text{A}}$ configuration. It is noteworthy that a lower I_D/I_G intensity ratio is observed for the NG sample synthesized at 800°C compared to that for the NG synthesized at 850°C , whereas the NG sample

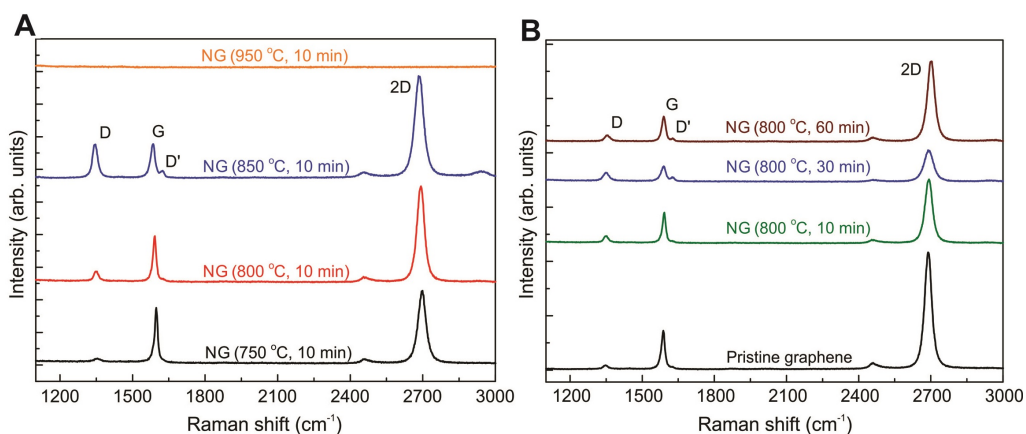


Figure B.2: NG sheets typical Raman spectra with different synthesis conditions. (A) Raman spectra of NG sheets synthesized with constant ammonia reaction time (10 min), but with different reaction temperature. (B) Raman spectra of NG sheets synthesized with constant ammonia reaction temperature (800°C), but with different reaction time. Adapted from (Feng et al., 2016).

produced at 750°C exhibits an even lower D band intensity (fig. B.2A). Therefore, the NG sample synthesized at 850°C presents a higher level of nitrogen doping, whereas the NG sample grown at 750°C barely shows any N doping. Furthermore, we notice that the NG sample doped at 800°C contains both double substitution (highlighted with circles in Fig. B.1D) and single substitution, which is called N_1 configuration (pointed out by the arrow in Fig. B.1D). Figure B.1G shows a model image of the N_1 configuration. Therefore, it is possible to correlate the Raman spectroscopy with STM studies and tune the nitrogen atom doping configurations by changing the doping parameters.

The enhancement factor efficiency of the nitrogen-doped graphene

The nitrogen doping not only affects the graphene Raman signal (D and D' bands) but also provides a considerable enhancement factor (EF) in the Raman scattering of the studied organic molecules when compared to PG (Lv et al., 2012). However, the mechanism for such enhancement remains an open question. Here, we provide an experimental and theoretical study of the GERS mechanism for both PG and NG. To study the GERS effect, different fluorescent dyes, such as RhB, CRV, and MB, were used as probe molecules.

To better compare the performance of NG and PG as substrates for GERS, we have calculated the EF for different dye molecules. The calculated EF plots are shown in fig. B.3 and are calculated using the raw intensity obtained from experimental spectra of molecules onto PG and NG. Because the Raman signal of the studied dyes (RhB, CRV, and MB) on SiO₂/Si is barely detected as a result of the strong fluorescence background (Feng et al., 2016), the calculated EF is not compared against SiO₂/Si. We report an EF that is sixteen times larger for NG than for PG (fig. B.3A). It is noteworthy that the EF of a given molecule is not the same for all the Raman modes. For instance, in fig. B.3A, the RhB Raman mode located at 1250 cm⁻¹ is much more enhanced when compared to that located at 1352 cm⁻¹. Such variations in the EF within modes have been previously reported (Huang et al., 2015).

To confirm the uniformity of the GERS effect within the graphene surfaces (PG and NG), we prepared a 1×10⁻⁷ M RhB solution and soaked both types of graphene into it. Representative Raman mappings of the intensity ratio between the 1650 cm⁻¹ peak of RhB and the graphene G band (I₁₆₅₀/I_G) are plotted in Fig. B.4A and B.4B for PG and NG, respectively. From these mappings, it can be concluded that the average ratio I₁₆₅₀/I_G

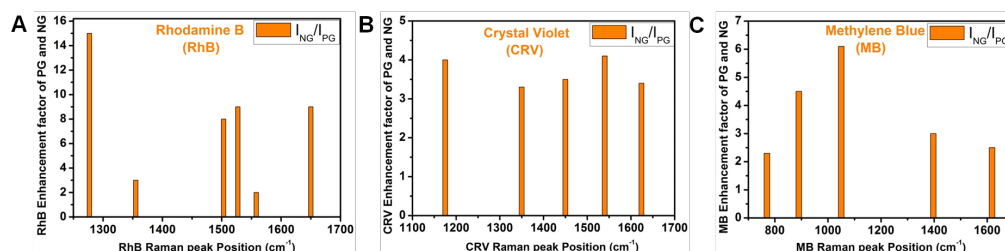


Figure B.3: Enhancement factor efficiency of the N-doped graphene. Enhancement factors for three different dye molecules between NG and PG: (A) RhB, (B) CRV, and (C) MB. It is clear that Raman intensities are larger for NG in all cases and range between 2 and 16 depending on the dye molecules and Raman peaks.

in PG is ca. 0.7, whereas that in NG is ca. 2. It could also be observed that the GERS effect is quite uniform across the surfaces. For the PG sample (Fig. B.4A), around 70% of the area is green-colored, whereas for the NG sample (Fig. B.4B), this ratio reaches around 85%, thus demonstrating a very good uniformity of the GERS effect across the samples.

The resonance Raman spectra of nitrogen-doped graphene probed for dye molecules

We further studied the GERS mechanism on these systems using several laser lines on freshly prepared NG samples with 5×10^{-5} M concentrations of RhB, CRV, and MB. Figure B.5A–C show the Raman spectra of RhB, CRV, and MB, respectively, when using a 5×10^{-5} M concentration on NG sheets recorded with excitation laser energies of 2.54 eV (488 nm), 2.41 eV (514.5 nm), 2.18 eV (568.2 nm), and 1.92 eV (647.1 nm) in the 1100 to 2900 cm⁻¹ spectral range. The spectra display the main Raman features related to graphene (the D, G, and 2D bands) and a number of other features arising from the dye molecules. The main features of the dye molecules show

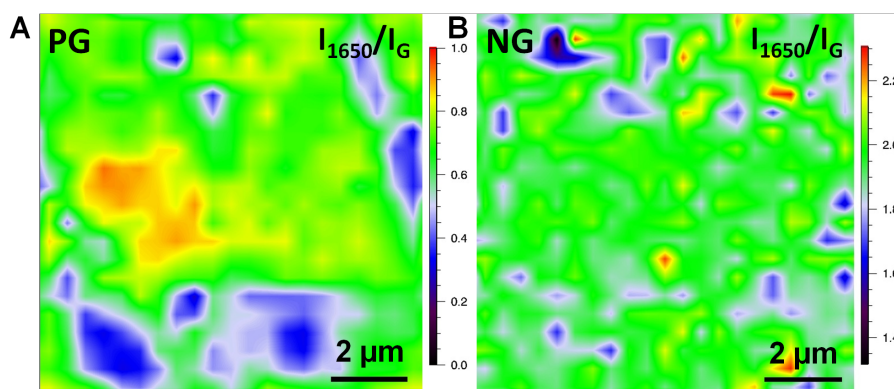


Figure B.4: **Raman mapping of PG and NG.** Raman mapping of the intensity ratio between the RhB 1650 cm^{-1} peak and the G-band (I_{1640}/I_G) plotted for (A) PG and for (B) NG. The average ratio of (I_{1650}/I_G) in PG is ca. 0.7 while for the NG is ca. 2. For PG samples around 70% of the area are green-colored, while for NG, this ratio reaches around 85%, thus demonstrating a very good uniformity across the samples and a signal enhancement for NG when compared to PG.

prominent enhancement when excited with the 2.41 eV laser line for the RhB (marked as solid diamonds) and CRV (marked as solid circles) dye molecules and with the 1.92 eV laser line for the MB (marked as solid stars) molecule. Those Raman features are barely observed for the other laser energies used. It is noteworthy that the remarkable enhancement of the Raman signal of MB, when excited with the 1.92 eV laser line, considerably screens the intensities of graphene D, G, and 2D peaks. Therefore, it is clear that the GERS effect results in a better EF when NG is used than when PG is used, and, hence, NG becomes an excellent substrate for the detection of low concentrations of fluorescent molecules, such as those described here.

The laser dependence of the 2D band frequency for various dye molecules on NG displays a linear dispersion relationship. The 2D band originated from two in-plane transverse optical (iTO) phonons around the \mathbf{K} or \mathbf{K}'

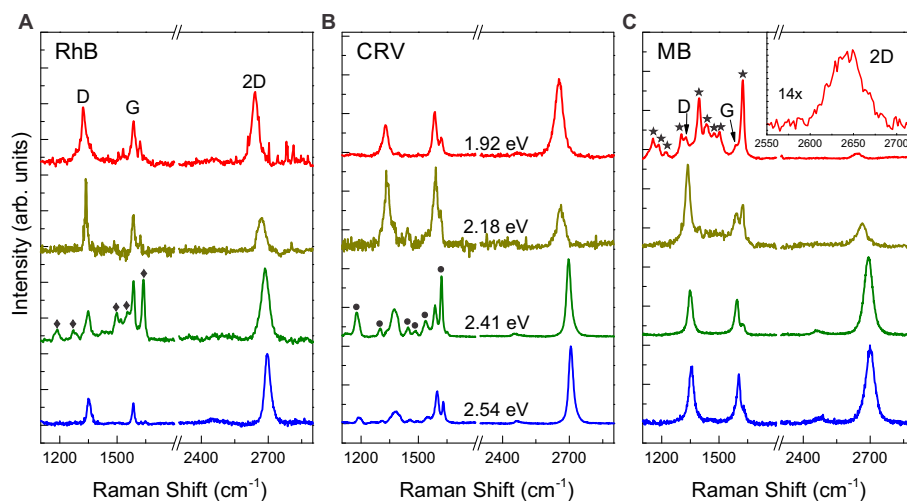


Figure B.5: **Resonant Raman scattering effect on NG sheets probed for different dye molecules.** Excitation laser energies of 2.54, 2.41, 2.18, and 1.92 eV are used to test the GERS effect of NG sheets with (A) RhB, (B) CRV, and (C) MB molecules. The probe molecule concentrations are all 5×10^{-5} M. The peaks marked with the diamond, circle and star symbols are the major Raman signals from RhB, CRV and MB molecules, respectively.

points in the first Brillouin zone and involves an intervalley double resonance (DR) process. The linear dispersion of electrons in graphene ensures that the incident photon energy will always coincide with the energy separation between the conduction and valence bands near the Dirac point, resulting in a DR process (Malard et al., 2009). The slope of the 2D band dispersion depicts a slight difference for each dye molecule. By fitting the curve, the slope values for each dye molecule are 89.7, 87.2, and $96.4 \text{ cm}^{-1}/\text{eV}$ for RhB, CRV, and MB, respectively (Feng et al., 2016). These results are in agreement with monolayer graphene (Malard et al., 2009; Carvalho et al., 2015a), thus suggesting that the iTO phonon dispersion is not significantly affected by the dye molecules.

The GERS efficiency of the nitrogen-doped graphene

To address the efficiency of the GERS mechanism on the PG and NG samples, we have prepared several RhB solutions with concentrations ranging from 5×10^{-5} to 5×10^{-11} M. Figure B.6A–G show the enhanced Raman scattering effect of each RhB concentration for both NG and PG samples. Once again, notice that the molecules on NG exhibit a higher Raman intensity when compared to the PG substrates. Therefore, the efficiency of the GERS mechanism using NG as a sensing substrate can be noticed for the very low concentration of RhB (5×10^{-11} M), whereas the dye molecules cannot be detected on PG for such a low concentration value. Here, the Raman signal remains strongly enhanced, and it is comparable to the 2D band intensity. Figure B.6H shows the relative Raman intensity ratio between the strongest Raman peak of RhB ($\sim 1650 \text{ cm}^{-1}$) and the graphene G band. The black and red curves represent the PG and NG as the sensing substrate, respectively. By comparing the relative Raman intensity of this 1650 cm^{-1} peak with different RhB concentrations, we observe that both the PG and NG samples with 5×10^{-7} M RhB show the highest enhancement effect. A possible explanation for this effect could be related to the aggregation of the RhB molecules for high concentrations (for example, 5×10^{-5} M) and the cluster formation on top of NG sheets, which decreases the Raman efficiency. In addition, for a low concentration (for example, 5×10^{-11} M), only a few RhB molecules will be involved in the Raman process, thus providing a decay of the relative Raman intensity.

From previous reports (Ling et al., 2010), it can be concluded that when the concentration is below 10^{-6} to 10^{-7} M, the layer of adsorbed dye molecule can be regarded as a sub-monolayer, which could explain that, for an even lower concentration (1×10^{-8} M), very little clustering occurs. Regarding the high-concentration samples (for example, 1×10^{-5} M), the

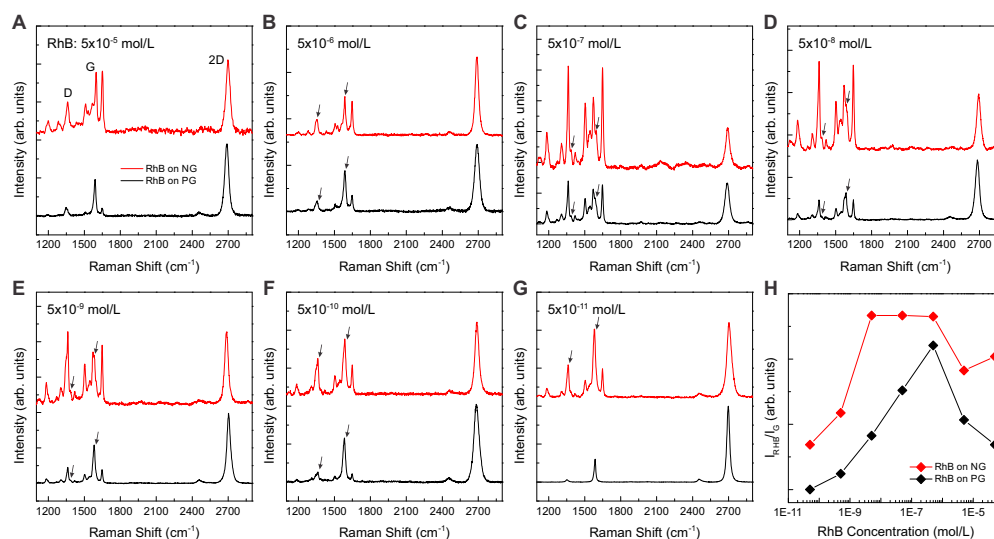


Figure B.6: Comparison of the enhanced Raman scattering effect between NG and PG sheets when probing RhB with different concentrations. Raman signals of RhB molecules on PG and NG sheets are shown here with (A) 5×10^{-5} M, (B) 5×10^{-6} M, (C) 5×10^{-7} M, (D) 5×10^{-8} M, (E) 5×10^{-9} M, (F) 5×10^{-10} M, and (G) 5×10^{-11} M RhB concentrations. The laser excitation line is 2.41 eV, and the integration time is 10 s for all cases, where the arrows indicate graphene G and D bands. (H) Raman intensity ratio between the strongest RhB peak (1650 cm^{-1}) and the graphene G band when NG (red curve) and PG (black curve) are used as a sensing substrate.

adsorbed dyes on top of PG/NG were not considered as monolayers, and clustering could happen on wrinkles, defects, etc. Therefore, rinsing does not remove all the clusters that contribute to the diminishing of the Raman signal of the molecules.

Table B.1 compares the present work with recent results of the GERS effect reported in the literature (Ling et al., 2010; Xie et al., 2009; Xu et al., 2011b; Hao et al., 2012; Ling et al., 2013; Qiu et al., 2011; Xu et al., 2013; Yu et al., 2011b). To the best of our knowledge, it is the first time that such low concentrations of dye molecules are detected when graphene is used as a substrate. Thus, it demonstrates that the NG sample can be effectively used to detect specific organic molecules with ultrahigh sensing capabilities.

Table B.1: Ultrasensitive molecular sensor. Comparison of the performance of different graphene samples as GERS substrates for molecular sensing. R6G, rhodamine 6G; PPP, protoporphyrin; CuPc, copper phthalocyanine.

Sensing material	Type of graphene	Detection level	Laser line	Reference
RhB	CVD N-doped graphene	5×10^{-11} M	514 nm	This work
R6G	CVD N-doped graphene	1×10^{-8} M	514 nm	This work
PPP	CVD N-doped graphene	1×10^{-8} M	647 nm	This work
R6G	Exfoliated graphene	8×10^{-10} M	514 nm	(Ling et al., 2010)
PPP	Exfoliated graphene	2×10^{-8} M	633 nm	(Ling et al., 2010)
R6G	Exfoliated graphene	1×10^{-5} M	514 nm	(Xie et al., 2009)
PPP	Exfoliated graphene	1×10^{-5} M	633 nm	(Xie et al., 2009)
CuPc	Exfoliated graphene	1×10^{-6} M	633 nm	(Xu et al., 2011b)
CRV	Exfoliated graphene	5×10^{-7} M	514 nm	(Qiu et al., 2011)
RhB	Mildly reduced GO	5×10^{-8} M	514 nm	(Yu et al., 2011b)
MB	Exfoliated graphene	1×10^{-4} M	647 nm	(Hao et al., 2012)
CuPc	Exfoliated graphene on Au	1 Å on top	633 nm	(Xu et al., 2013)
CuPc	Exfoliated graphene	3 Å on top	633 nm	(Ling et al., 2013)
PPP	Exfoliated graphene	3 Å on top	633 nm	(Ling et al., 2013)

First-principles calculations

To gain further insight into and build a microscopic picture of the physical mechanisms responsible for the observed GERS effect, *ab initio* calculations were carried out to study the interaction of the dye molecules with PG and NG substrates. The densities of electronic states (DOS) of the systems are depicted in Fig. B.7. The reference energy in these graphs is the E_F of the graphene cluster. The double nitrogen substituted cluster that represents a doping level of 1 atomic% has a Fermi energy raised by 0.22 eV with respect to the reference, in accordance with the expected n-type doping behavior of double substitutional nitrogen. When compared to the bare substrates, the DOS of the substrates with adsorbed organic molecules exhibit small modifications because of additional states brought by the molecules. The DOS projected on the adsorbed molecules (PDOS) are also shown (denoted by the filled curves). There is an increasing mixing of states in the order $CRV < RhB < MB$ because of the interaction of the molecules with the PG and NG electronic densities. These molecules are cations and interact electrostatically with the graphene's electronic density through the induction of image charges (Pham et al., 2016). The electric field of the image charges shifts the molecular levels and decreases the HOMO-LUMO gap. Figure B.7C and B.7D depict the DOS and PDOS of the CRV over PG and NG systems, respectively; the peaks corresponding to the HOMO (near -2.0 eV) and LUMO (near 0.7 eV) states for the molecule adsorbed on PG shift toward lower energies when adsorbed on NG because of an increased image charge field. For the CRV molecule, the charge transfer is negligible and the electrostatic effect dominates. The other two dyes interacting with NG have the band of states associated with the LUMO level partially filled, and the Coulomb repulsion shifts the HOMO level to a higher energy. The combination of image charge field and Coulomb repulsion does not change the HOMO position of RhB (Fig. B.7, A and B). Nevertheless, for MB, where the charge transfer is the

highest, the HOMO level is higher in NG (Fig. B.7, E and F). In all the studied cases, NG shifts the E_F to a higher energy and brings the LUMO bands of the adsorbates close to that E_F . The vertical line indicating the E_F of NG crosses the LUMO bands of all dyes. Figure B.7 (B, D, and F) shows the (peak-to-peak) HOMO-LUMO and the HOMO- E_F energy gaps (indicated by the two arrows), which we believe to be the resonance condition needed for outstanding Raman enhancement.

It should be noted that the studied dye molecules are cations that interact more strongly with NG. The highest E_F was achieved for RhB on NG (fig. B.3A), whose symmetry group is C_1 , which corresponds to the lowest symmetry among all tested systems (C_3 for CRV and C_{2v} for MB). This result is not in agreement with a previous report, where it was concluded that the molecular symmetry has to be close to graphene's symmetry to achieve high Raman signal enhancement (Huang et al., 2015). Because the symmetry theory does not explain our findings, we believe that there is no unique explanation for the E_F s, and many aspects may contribute to this.

Table B.2: Comparison of the calculated HOMO-LUMO gap. Calculated HOMO-LUMO gap, adsorption data and resonant Raman laser energy for each molecule in electron volts. ΔG and E_L stands for HOMO-LUMO gap and laser energy, respectively.

Dye Molecule	ΔG on PG	ΔG on NG	HOMO- E_F gap on NG	Adsor. peak	Resonant E_L
RhB	2.73	2.65	2.39	2.29	2.41
CRV	2.62	2.61	2.41	2.11	2.41
MB	2.48	2.38	2.22	1.89	1.92

Table B.2 summarizes the value of the calculated HOMO-LUMO gap of each molecule, the experimental absorption peaks for each molecule, and the laser excitation energy when resonant Raman happens with each molecule studied in this work (Fig. B.5). The calculated energy gap values of RhB, CRV, and MB on NG substrates shown in Fig. B.7 are 2.20 eV (558.5 nm), 2.41 eV (514.5 nm), and 2.39 eV (518.8 nm), respectively.

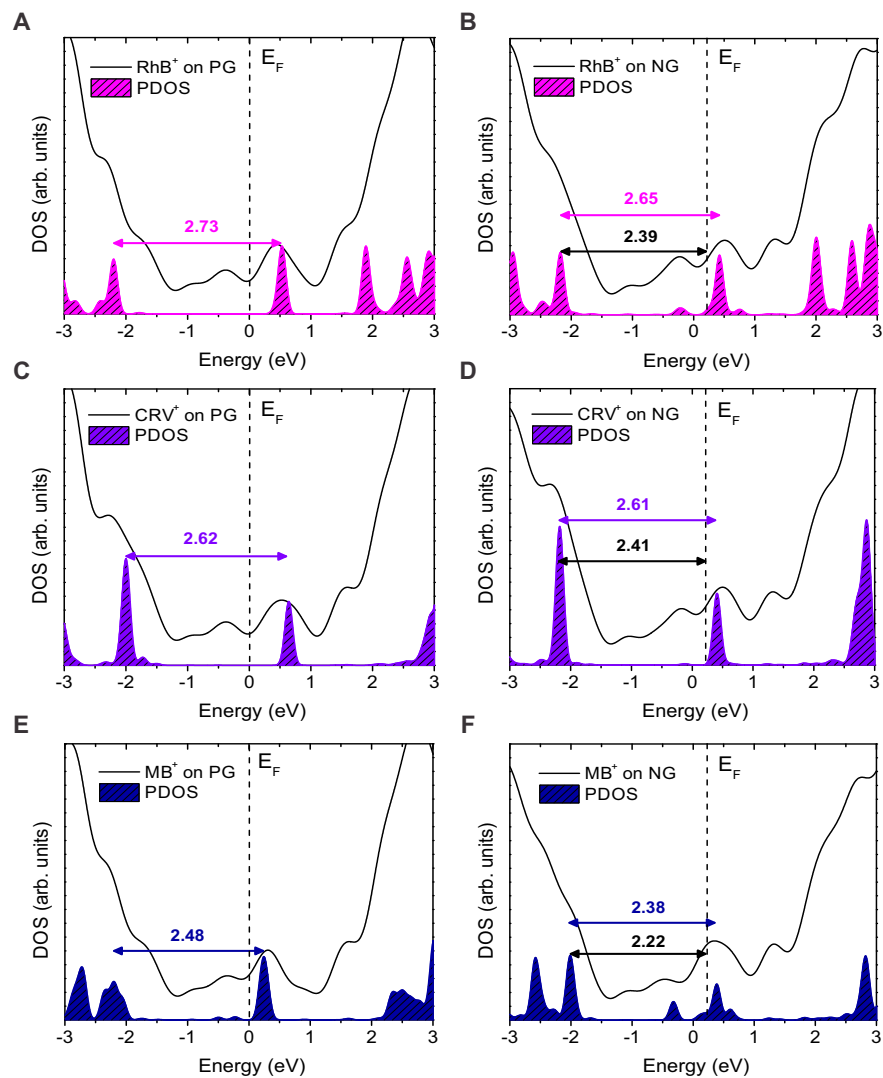


Figure B.7: **DOS of the clusters representing the adsorbed organic dyes on PG and NG.** DOS for RhB (A and B), CRV (C and D), and MB (E and F) are shown. The filled areas are the PDOS projected on the dyes. Vertical dashed lines indicate the position of the system's Fermi energy, E_F . Horizontal arrows and values indicate the HOMO-LUMO gaps (in electron volts) and the energy HOMO- E_F (in electron volts).

From the above calculations, we can conclude that enhanced Raman sensing requires a substrate's Fermi energy close to the LUMO level of the probe molecule. This feature allows an effective charge-transfer excitation: The photon originally absorbed by the substrate causes an excitation that can be transferred to the molecule through a resonance effect. We also note that Raman sensing is strongest when the laser excitation energy is close to the molecular HOMO-LUMO gap, as shown in Fig. B.7. It is noteworthy that the HOMO-LUMO gaps of linear carbon chains encapsulated inside carbon nanotubes have also been found using resonant Raman spectroscopy (Endo et al., 2006; Fantini et al., 2006). A second conclusion could be drawn by comparing the sensitivity of PG and NG toward the tested dyes: The increasing strength of interaction, that is, $CRV < RhB < MB$, corresponds to an increased sensitivity.

Ling et al. carried out wavelength-scanned Raman measurements of the CuPc molecules deposited onto mechanically exfoliated PG, obtaining the Raman excitation profile of different vibrational modes of the CuPc molecule on PG (Ling et al., 2012a). These authors concluded that the profiles obtained using PG are completely different from those recorded without graphene, and a charge-transfer resonance peak located at ~ 1.9 eV occurs when the PG E_F aligns with the molecular HOMO-LUMO gap. These results are similar to ours, in which a charge-transfer mechanism takes place; graphene can influence the Raman signal of the dye molecules, and a clear resonant effect is observed when the laser excitation energy is close to the molecular HOMO-LUMO gap. However, a clear advantage of our technique is that, by using NG as substrate, it is possible to tune the E_F of graphene and elucidate the alignment of the LUMO of the molecules with the E_F in doped graphene.

As the last test of the charge-transfer excitation model, we performed a vibrational analysis of the isolated dyes and calculated the intensities of the Raman active modes. We considered that the charge-transfer excitation is

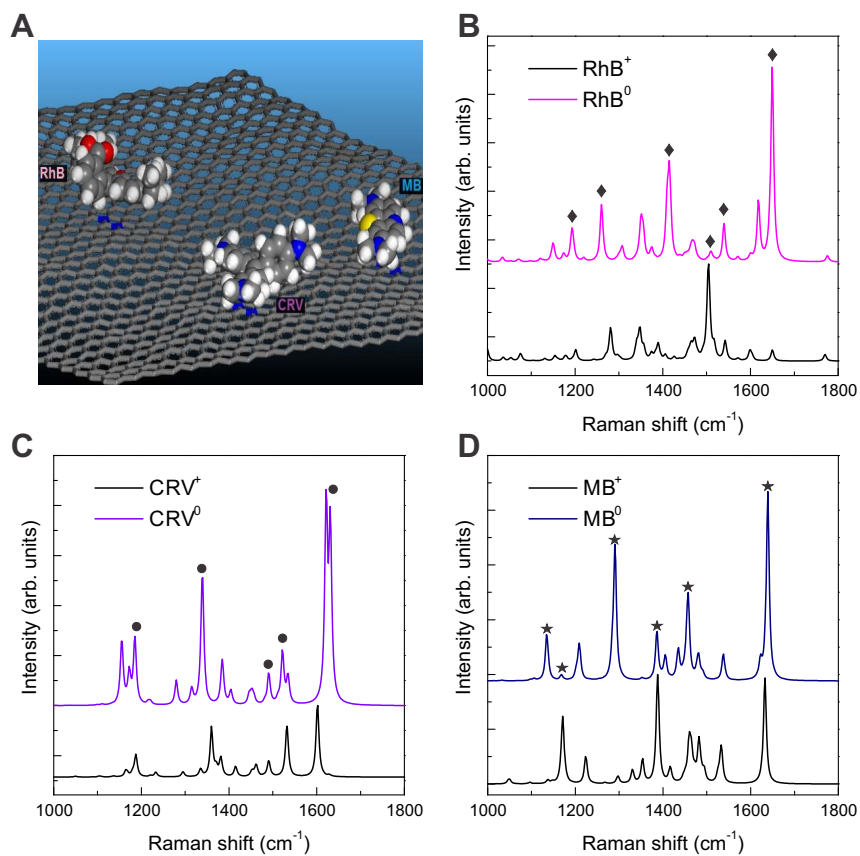


Figure B.8: **Simulated Raman spectra of the dye molecules.** (A) Simulated configuration when RhB, CRV, and MB molecules lay on top of NG sheets. (B to D) Simulated Raman spectrum when (B) RhB, (C) CRV, and (D) MB are on top of NG sheets. Black curves are the spectra of the cations, and colored curves are the spectra of neutral molecules in the same geometry of the cations.

much faster than the molecular geometric relaxation because fluorescence is suppressed. For these calculations, we adopted the conformation of the cationic ground state and two charge states, the positively charged state and a neutral state obtained by adding one electron to the molecules without allowing molecular relaxation. The resulting simulated Raman spectra are shown in Fig. B.8B–D. The frequencies of the neutral molecules do not change much from the values obtained for the cations; however, the relative intensities change because of the charge redistribution in the neutral systems. When compared to the experimental spectra shown in Fig. B.5, the simulated Raman spectra agree remarkably well with the measured frequencies and intensities. (The peaks marked with diamond, circle and star symbols are the major experimental Raman signals from RhB, CRV, and MB molecules, respectively.) We note that the features in the experimental spectra seem to be a combination of the neutral molecule (stronger) and the cation (weaker) spectra, thus suggesting that GERS comes from a charge-transfer excitation.

Conclusion

We have demonstrated that it is possible to control the nitrogen content and configuration within the graphene lattice (either as a single or as a double substitution) by changing the synthesis conditions (for example, temperature when introducing NH_3 and reaction time). These NG monolayers were then further used as GERS substrates to probe various dye molecules, and we observed extraordinary sensing properties when compared to PG sheets. For example, the Raman signals of these particular dye molecules can be detected for concentrations as low as 10^{-11} M, which is the lowest ever reported value to date when graphene is used as a substrate. Electronic structure calculations and the simulation of the Raman spectra by density functional theory (DFT) suggest that a charge-transfer excitation is

the mechanism for GERS. The enhancement of the studied molecules' Raman signal is more significant for NG than it is for PG because the LUMO levels of the dyes are closer to the E_F of NG. There is no correlation between the dye molecule symmetry and the enhancement of the Raman signal, according to the analysis of the obtained data. Furthermore, when using different laser excitations, it is possible to determine the HOMO-LUMO gap of a molecule simply by performing resonant Raman measurements. Our findings indicate that doped graphene could be tuned for an effective sensing of fluorescent molecules via GERS when the appropriate laser excitation is used, and HOMO-LUMO gaps of the molecules could also be extracted via resonant Raman. These results open up new avenues for developing emerging molecular sensing techniques. This work on NG complements other research carried out using PG, and we have explored the effects of N doping in conjunction with different dye concentrations, UV-visible transmission data, and theoretical simulations. On the basis of these results and other published work on PG, we propose a model for the Raman enhancement induced by doped graphene.

C OPTICAL IDENTIFICATION OF SULFUR VACANCIES: BOUND EXCITONS AT THE EDGES OF MONOLAYER TUNGSTEN DISULFIDE

In this appendix, we present an evidence of bound exciton emission on the edge of monolayer WS₂-CVD. Here, photoluminescence experiments at low-temperature demonstrate that bound exciton emission induced by mono-sulfur vacancies is concentrated near the edges in as-grown monolayer tungsten disulfide. This work was developed during the doctoral internship at the Pennsylvania State University, and published in the journal *SCIENCE ADVANCES* 3 (4), E1602813 (2017).

Introduction

Two-dimensional transition metal dichalcogenides (TMDs) have been studied intensively for their extraordinary electronic and optical properties (Novoselov et al., 2005; Butler et al., 2013) such as acquiring a direct band gap when thinned down from the bulk (Mak et al., 2010), hosting strong electron-hole Coulomb interactions (Mak et al., 2013; Ross et al., 2013), and supporting a variety of many-body states beyond excitons (Qiu et al., 2013; Carvalho et al., 2015b). Their intriguing optical properties have opened prospects for a broad range of applications, including valleytronics (Mak et al., 2012; Zeng et al., 2012), photosensors (Perea-López et al., 2013), and nanocavity lasers (Wu et al., 2015b).

The near-bandgap optical properties of TMDs are governed by excitons. While neutral excitons are typically mobile, both neutral and charged lattice defects can bind electron-hole pairs to form the so-called bound excitons. The finite binding energy between the neutral exciton and the defect creates a bound-exciton peak X^B in the photoluminescence (PL) spectrum

at an energy smaller than the neutral-exciton peak X^0 (Tongay et al., 2013; Mak et al., 2013; Peimyoo et al., 2014; Yuan et al., 2014). Previous works reported a bound-exciton feature in the photoluminescence spectrum of defective exfoliated TMDs after exposure to alpha irradiation or oxygen plasma treatment (Tongay et al., 2013; Chow et al., 2015), as well as in *pristine* exfoliated samples (Tongay et al., 2013; Mak et al., 2012; You et al., 2015; McCreary et al., 2016). Defects in the TMD family have also been characterized on samples synthesized by chemical vapor deposition (CVD) (Lee et al., 2012; Zhan et al., 2012; Cong et al., 2014; Lin et al., 2014; Zheng et al., 2015; Gong et al., 2014; Zhang et al., 2015). However, a quantitative study of the bound exciton's thermal stability, dynamics, and dependence on defect density remains absent and is explored here.

Here, we investigate bound-exciton emission in CVD-grown triangular islands of monolayer tungsten disulfide (WS_2), with particular focus on the differences between the interior regions and the edges of the island. We report a direct spatially resolved observation of two bound-exciton transitions X^{B_1} and X^{B_2} at the edge of the triangular islands. Atomically resolved images showed a high mono-sulfur vacancy concentration of $0.92 \pm 0.45 \text{ nm}^{-2}$ near the edges, in contrast to $0.33 \pm 0.11 \text{ nm}^{-2}$ in the interior. First-principles calculations confirmed that sulfur vacancies introduce mid-gap states that are tightly localized near sulfur vacancies, suggesting that excitons can bind more strongly to these localized charged defect than to free charge carriers. The calculated finite matrix elements between the defect states and the valence band states implies that the radiative recombination of the exciton through this channel is allowed and observable in the PL spectra. Under optical pumping, the intensity of the bound-exciton peaks show a sub-linear dependence on the laser intensity, verifying their bound nature. While the bound-exciton peak X^{B_2} is $\sim 300 \text{ meV}$ below the neutral exciton peak, temperature-dependent PL experiments determined the thermal activation energy of X^{B_2} to be only

~ 36 meV. To resolve this apparent paradox, we propose that the decay process involves the thermal dissociation of the bound exciton into a neutral exciton and the charged defect.

Spatially resolved photoluminescence at low temperature

Monolayer WS_2 samples were grown by CVD on 300 nm SiO_2/Si substrates, as detailed in Chapter 3. Similarly to monolayer MoS_2 , the structure of monolayer WS_2 is a sandwich of W atoms between two hexagonal layers of S atoms (S-W-S) with a trigonal prismatic coordination (D_{3h} point group), 1H- WS_2 (hereby, 1H denotes monolayer, D_{3h} point group) (Zhou et al., 2013). An atomically resolved image acquired from an area in the interior of a triangular island, where the defect density is lower than that near the edge, shows this 1H- WS_2 structure, as shown in Fig. C.1.

Figure C.1B shows an optical image of the triangular WS_2 selected for further investigation. Figure C.1C shows three PL spectra, normalized by the intensity of the neutral exciton, taken from the marked regions in Fig. C.1B: \circ and \square from the edges and \triangle from the interior. The spectra were acquired at 77 K using 488 nm laser excitation with a power density of 9 kWcm^{-2} to avoid heating effects. The X^0 peak in the interior (triangle) is sharp and symmetric with a full width at half maximum (FWHM) of $\Gamma_{X^0} = \sim 23$ meV; this indicates an absence of trions and a negligible degree of n-doping. For the other locations, the neutral exciton peaks redshift by 10 (square) and 20 meV (circle) as compared to the interior. This shift has been ascribed to band gap renormalization modulated by defect density (Bao et al., 2015).

In contrast to the interior, the PL spectra around 2050 meV at the two edges (circle and square) have asymmetric lineshapes that suggest the presence of bound excitons. The shoulder, which is identified here

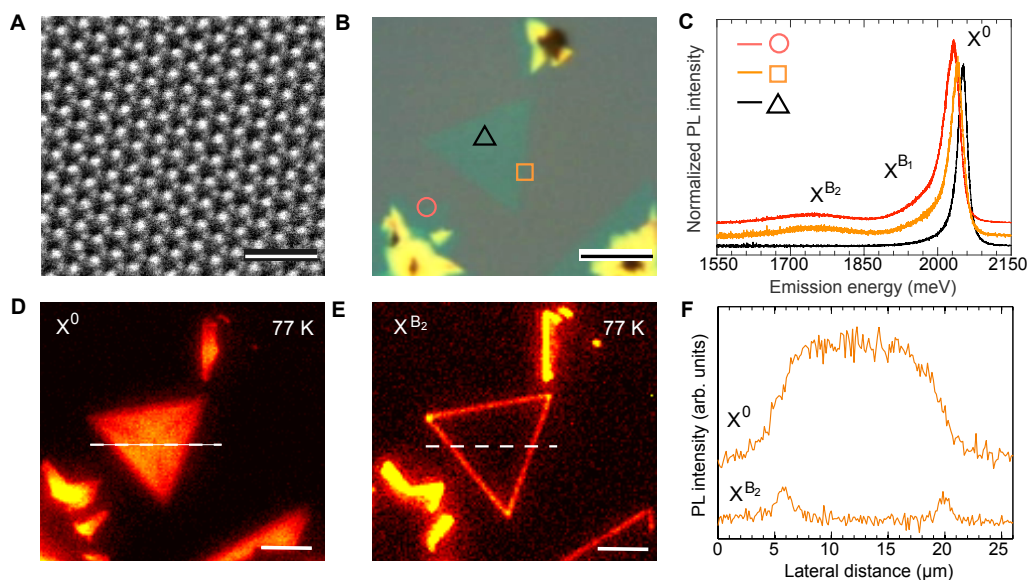


Figure C.1: **Bound excitons at the edges.** (A) Atomic structure of monolayer 1H-WS₂, scale bar is 1 nm. (B) Optical image of triangular WS₂ islands. (C) PL spectra obtained from the marked regions in (B). Photoluminescence intensity image at 77 K of (D) X⁰ peak centered at ~1970 meV and (E) X^{B₂} peak centered at ~1690 meV, scale bars are 10 μm. (F) X⁰ and X^{B₂} intensity profiles acquired along the dashed lines in (D) and (E), respectively.

as bound exciton X^{B₁}, only emerged when the bound exciton peak X^{B₂} centered at ~1750 meV also appeared. The bound exciton binding energy is defined as the energy difference between the neutral exciton and the bound exciton: $\Delta_{X^{B_n}} = E_{X^0} - E_{X^{B_n}}$. The binding energies were $\Delta_{X^{B_1}} = \sim 29$ meV and ~ 35 meV at the square and circle, respectively, while $\Delta_{X^{B_2}} = \sim 300$ meV for both edge locations. Although the measured $\Delta_{X^{B_1}}$ are close to the reported trion binding energy (Berkelbach et al., 2013; Mak et al., 2013), we will confirm in the next section that the emission is indeed from a bound exciton.

We performed spatially-resolved PL measurements at low temperatures to further investigate the bound exciton in monolayer WS₂. The

incident light spanned from 2140 to 2340 meV, while reflected light was collected using two bandpass filters centered at 1970 meV and 1690 meV. Figure C.1D and C.1E show the PL intensity map at 77 K for the X^0 peak (centered at 1970 meV) and the X^{B2} peak (centered at 1690 meV). The intensity of the neutral exciton is relatively homogeneous, whereas the bound-exciton intensity is highly localized at the edges of the WS_2 island. This behavior is also visible in the intensity profiles of Fig. C.1F acquired along the dashed lines in Figs. C.1D and C.1E. This is the first direct evidence of bound excitons in as-grown monolayer TMDs.

Defects at the edges

To investigate the structural differences between the interior and edge regions of WS_2 triangles at the atomic scale, scanning transmission electron microscopy (STEM) was performed. Prior to STEM imaging, a WS_2 triangle was transferred to a Quantifoil gold grid with holey carbon film (Fig. C.2A left panel). The interior and the edge regions marked by circles in Fig. C.2A were investigated by STEM-annular dark field (ADF) imaging. Mainly two types of defects were observed in both regions: mono-sulfur vacancies (V_S , yellow circle in Fig. C.2A) and occasional WS_3 vacancies (V_{WS_3} , orange triangle in Fig. C.2A). More V_S were found in the edge regions and they tend to aggregate. Other types of defects such as W vacancies (V_W), di-sulfur vacancies (V_{S_2}), and antisite defects such as S2 substituting a W site (S_{2W}) or its opposite (W_{S_2}) were observed only very rarely. To obtain STEM-ADF images with higher contrast from sulfur atoms, a low-angle annular dark field (LAADF) condition was used. Under this condition the ADF intensity includes both Z contrast and diffraction contrast; defect structures were confirmed by comparing ADF images with simulated STEM images, as shown in Fig. C.2B. V_S and V_{WS_3} have been previously reported for monolayer MoS_2 (Zhou et al., 2013). Here, we focus on the

density of V_S because the density of V_{WS3} defects is much lower. Counting the number of V_S on ADF images acquired from each region (Fig. C.2C), we obtain defect densities of 0.33 ± 0.11 and $0.92 \pm 0.45 \text{ nm}^{-2}$ in the interior and at the edge, respectively. The higher V_S defect density in the edge region is consistent with our observation of bound excitons at the edge, and also with previous reports on defect distribution in monolayer MoS_2 (Bao et al., 2015). These V_S defect densities are much higher than reported values for CVD-grown MoS_2 ($\sim 0.12 \text{ nm}^{-2}$) (Hong et al., 2015).

Optical pump

To verify that $X^{B_{1,2}}$ indeed involves excitons bound to defects, we investigated exciton population as a function of the incident laser power density from 9 to 230 kWcm^{-2} at 77 K, using continuum wave (CW) excitation at 488 nm. Figure C.3A and C.3B depict the evolution of PL spectra at 77 K acquired from the interior and edge regions, respectively, on a different sample from Fig. C.1B. The neutral exciton energy ($\sim 2050 \text{ meV}$) did not change as a function of laser power density. However, the Lorentzian width Γ_{X^0} of X^0 increased with increasing laser intensity, broadening by $\sim 3 \text{ meV}$ and $\sim 6 \text{ meV}$ for the interior and edges areas, respectively. The increased broadening observed from the edges could be related to bound exciton emission X^{B_1} .

The insets in Fig. C.3A and C.3B display the low-energy spectral range marked by the dotted rectangle around 1750 meV. The absence of a bound exciton in the interior of the triangle confirms that the higher laser intensities did not create such defects in the high-quality regions. In contrast, the bound exciton is clearly observed near the edges of the triangle. Figure C.3C shows a logarithmic plot for the intensity of the bound exciton transitions $I_{X^{B_1}}$ and $I_{X^{B_2}}$, obtained from the edge region (Fig. C.3B) as a function of the neutral exciton intensity, I_{X^0} . The data can be fitted by a

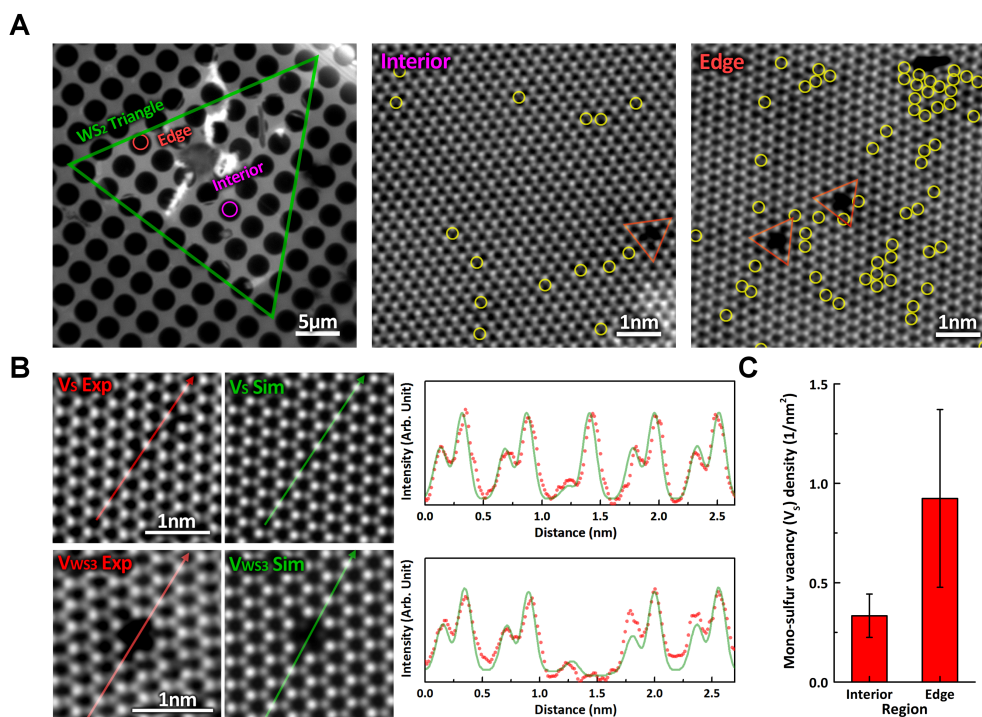


Figure C.2: **Identification of sulfur vacancies.** (A) Optical image of transferred WS₂ triangle onto Quantifoil (left), and high-magnification ADF images from center part (center) and edge part (right) which is within 1 μm from edge of WS₂ triangle. Mono-sulfur vacancies (V_S) and 1 tungsten +3 sulfur vacancies (V_{WS3}) were marked by yellow circles and orange triangle, respectively; (B) Comparison of experimental and simulation ADF image of V_S and V_{WS3} vacancies. The line profile was acquired along the line in ADF images; (C) Calculated mono-sulfur vacancy (V_S) density from center and edge region. The error bar means standard deviation of mono-sulfur vacancy density.

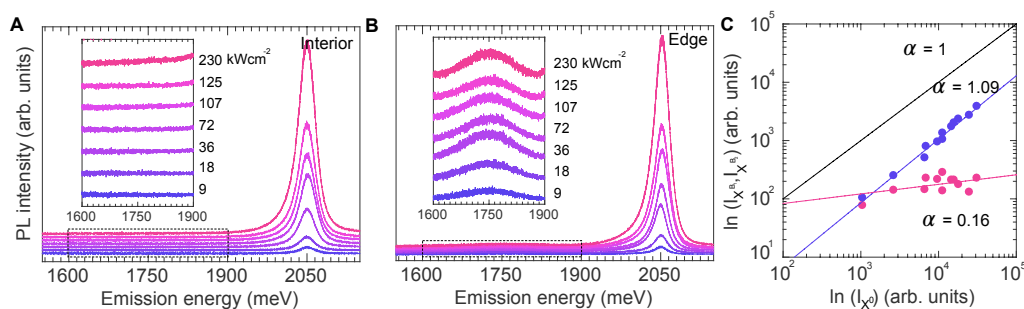


Figure C.3: **Evolution of PL spectra with laser power density.** (A) interior area and (B) at the edge. Inset, low energy region marked by a dotted rectangle around the bound exciton emission at 1750 meV. (C) Logarithmic plot of the $I_{X^{B_1}}$ (blue) and $I_{X^{B_2}}$ (pink) intensity of bound excitons, as a function of the neutral exciton emission intensity I_{X^0} . Lines are power-law fits and the dashed line $\alpha = 1$ is included for comparison.

power law of the form $I_{X^{B_1}} \propto (I_{X^0})^\alpha$ with $\alpha = 0.76 \pm 0.01$, and $I_{X^{B_2}} \propto (I_{X^0})^\alpha$ with $\alpha = 0.52 \pm 0.01$, as shown in Fig. C.3C. The difference between exponents may arise from uncertainties in extracting the X^{B_1} peak from the shoulder of the main emission (for which the position of X^{B_1} was fixed for simplicity); these uncertainties do not affect the conclusion that $\alpha < 1$. The sub-linear trend ($\alpha = 0.76$ and 0.52) is a signature of emission from bound excitons, since defect sites in the lattice become saturated with trapped excitons at higher laser intensities (Shang et al., 2015; You et al., 2015; Tongay et al., 2013). For the same reason, the bound exciton X^{B_1} cannot be attributed to free-trion emission: optical pumping of electrons to the conduction band would yield linear behavior for both neutral exciton and free-trion populations (Mitioglu et al., 2013; You et al., 2015; Ross et al., 2013) (see the guide at $\alpha = 1$ in Fig. C.3C).

Thermal stability of bound excitons

As mentioned above, bound excitons emerge when defects such as sulfur vacancies trap neutral excitons at low temperatures. The thermal stability of this complex depends on the activation energy that binds the neutral exciton to the defect (Lampert, 1958; Yu and Cardona, 2010; Hamby et al., 2003; Meyer et al., 2004). Figure C.4A shows the variation in PL intensity from 77 to 113 K acquired at the edge using a power density of 9 kWcm^{-2} , normalized by the neutral exciton peak at 2050 meV. The white vertical line traces the position of X^{B_2} , and the PL spectra for five temperatures are replotted in Fig. C.4B. The X^{B_2} peak at $\sim 1750 \text{ meV}$ decreases in intensity as the temperature increases and disappears above 107 K.

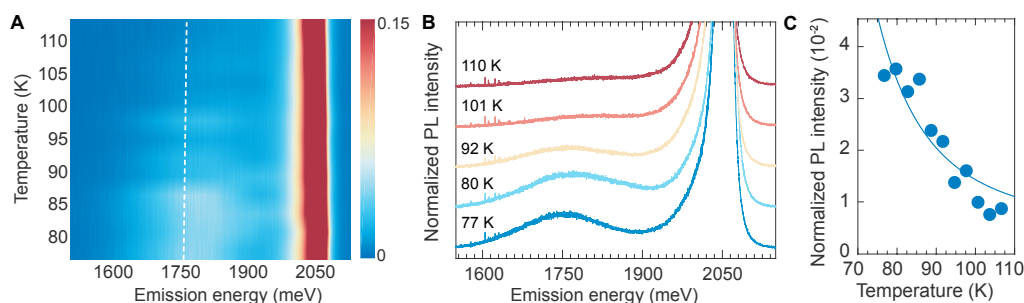


Figure C.4: Dependence of PL spectra with temperature. (A) PL intensity map of neutral and bound energy emission changing with temperature in the range between 77 and 113 K, white vertical line is guide to X^{B_2} position. (B) PL spectra extracted from (A) for five different temperatures. (C) Normalized $I_{X^{B_2}}$ peak as a functions of temperature and the corresponding fit to the data. The thermal activation energy of bound exciton is $36 \pm 6 \text{ meV}$.

To estimate the thermal activation energy, we consider a simple rate equation for bound exciton dynamics, $dN/dt = \beta - \gamma N$, where N is the density of bound excitons, β is their formation rate (assumed to be temperature-independent), and the decay rate γ is temperature-dependent according to

$$\gamma = \tau^{-1} + Ce^{-E_A/(k_B T)}. \quad (\text{C.1})$$

Here τ is the lifetime of the bound exciton, C is a prefactor and E_A is a thermal activation energy (Feldmann et al., 1987). The PL intensity $I_{X^{B_2}}$ of the bound exciton in steady state is proportional to γ^{-1} . Figure C.4C shows the normalized PL intensity $I_{X^{B_2}}$ as a function of temperature along with a fit to equation (C.1), where we find $\tau = 56$ ns, $C = 5.5 \times 10^3$ s⁻¹ and $E_A = 36 \pm 6$ meV.

The deviation of the measured PL intensity from the fit above 100 K may be attributed to the low signal-to-noise ratio of the bound-exciton peak in that temperature range, or to other unidentified excitonic levels at higher energies than the neutral exciton level that can host additional thermally activated decay pathways. Surprisingly, the thermal activation energy of X^{B_2} is far smaller than its binding energy $\Delta_{X^{B_2}} = 300$ meV, but close to the binding energy of X^{B_1} , $\Delta_{X^{B_1}} \approx 32$ meV. We propose that at low temperatures, neutral excitons bind to *negatively charged* sulfur vacancies by 36 meV, forming a *defect-bound exciton* that consists of one valence band hole, one conduction band electron, and one electron at the defect state (~ 300 meV below the conduction band minimum). Two types of emissions are expected from the defect-bound exciton: recombination of the electron localized at the defect with the valence band hole contributes to the X^{B_2} peak, while the recombination of the conduction band electron with the valence band hole contributes to the X^{B_1} peak. As the temperature increases, this *defect-bound exciton* dissociates into a neutral exciton and an electron remaining at the defect site (Naumov et al., 1993), leaving only the X^0 peak corresponding to neutral exciton recombination. In addition, the temperature dependence of the PL peak position for the neutral exciton X^0 was studied from spectra acquired from the interior and at the edges, as shown in Fig. C.5;

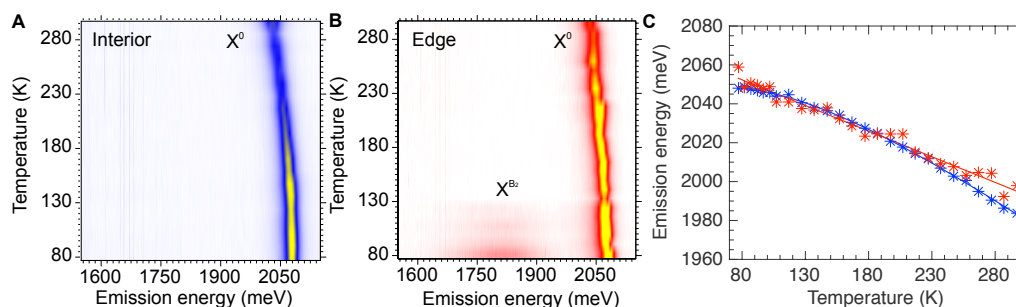


Figure C.5: **Temperature-dependent PL for the interior and edge regions.** PL intensity map at the (A) interior and (B) edge regions showing the evolution of excitons in the WS_2 sample as a function of temperature and emission energy. (C) X^0 emission energy as a function of temperature at the interior (blue) and edge (red) regions. The solid lines are fits to equation (C.2).

Figure C.5 shows PL intensity maps obtained using 0.05 mW laser power at temperatures from 77 to 300 K acquired from the interior (fig. C.5A) and edge (fig. C.5B) regions of the monolayer WS_2 . We can observe the X^{B_2} bound exciton starting at 107 K (see fig. C.5B).

Figure C.5C shows the emission energy of the neutral exciton (X^0) as a function of temperature acquired from the interior (blue) and edge (red) regions. The emission energy of the neutral exciton as a function of temperature is described by the O'Donnell model, derived from the thermodynamics of electron-hole pairs in semiconductors given by,

$$E_{X^0}(T) = E_{X^0}(0) - S\langle\hbar\omega\rangle\left[\coth\left(\frac{\langle\hbar\omega\rangle}{2kT}\right) - 1\right], \quad (\text{C.2})$$

where $E_{X^0}(0)$ is the neutral exciton energy at zero temperature, S is a dimensionless coupling constant, and $\langle\hbar\omega\rangle$ is an average phonon energy. The solid line blue (red) in fig. C.5C are reconstructions corresponding to equation (C.2). The parameters $E_{X^0}(0)$, S , and $\langle\hbar\omega\rangle$ are obtained using

nonlinear regression. We found $E_{X^0}(0) = 2205$ (2070) meV, $S = 2780$ (1530) meV, and $\langle \hbar\omega \rangle = -35$ (-0.3) meV for the interior (edge) region.

Therefore, the similar behavior of the X^0 peaks in the interior and at the edge supports the conclusion that it is unrelated to defects.

First-principles calculations

We performed density functional theory (DFT) calculations to investigate the electronic structure and optical response of WS_2 monolayers containing sulfur vacancies. The band structure of a 5×5 WS_2 supercell containing one sulfur vacancy is shown in Fig. C.6A, along with the projection of the wavefunction onto the atomic orbitals of the nearest-neighbor tungsten sites of the sulfur vacancy, represented by the red component of the colored bands. The vertical arrows indicate the optical transitions for the neutral exciton X^0 and the bound exciton X^{B_2} (or more precisely, the band transitions most closely associated with these processes). The mid-gap state is tightly localized near the sulfur vacancy. The root mean square radius of partial charge density of the defect state is 0.95 lattice constants, smaller than the typical (~ 3 lattice constant) radius of neutral excitons in monolayer TMDs (Qiu et al., 2013). Thus, if this state is charged (which is consistent with most of the CVD grown WS_2 samples being n-doped), the binding of a neutral exciton to this localized charged defect can be more stable than binding to free charge-carriers (forming free trions).

The quantitative estimate of the emission energy from the defect bands to the valence bands cannot be properly described by directly taking Kohn-Sham eigenvalues of the defect states, but instead requires correct evaluation of the energetics of charged defects, since any optical transition to or from the defect state involves a change in its charged state (Gallino et al., 2010; Van de Walle and Neugebauer, 2004; Freysoldt et al., 2014). To this end, we first calculated the defect formation energy for the charged

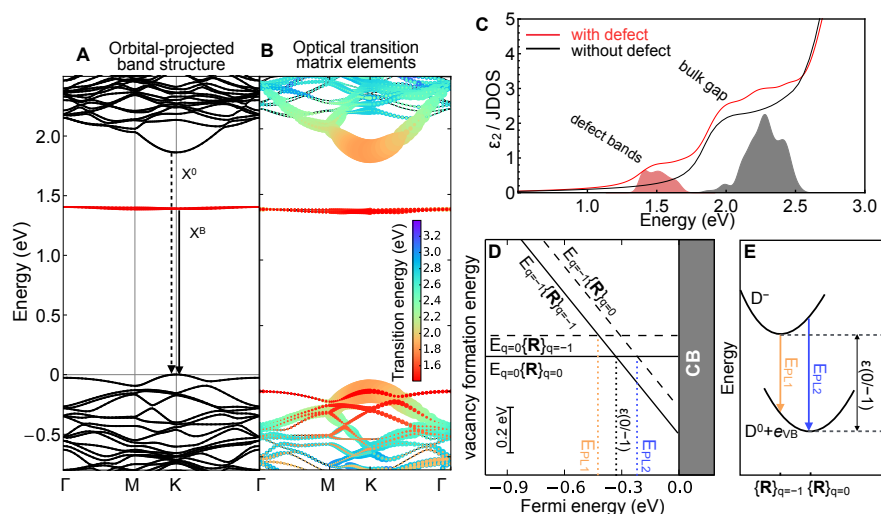


Figure C.6: **First-principles calculations of mono-sulfur vacancy.** (A) Band structure of 5×5 WS_2 supercell containing a mono-sulfur vacancy, where the red component of the colored bands represents the projection of the total wave-function onto the atomic orbitals of the three W atoms nearest to a sulfur vacancy. (B) The same band structure superimposed with colored circles representing the transition energies and magnitudes of the optical transition matrix elements. For each transition, a pair of identical circles are added to the initial and final state with colors indicating the transition energy and sizes indicating the magnitude of the matrix element. (C) Unfilled curves are the imaginary part of the RPA dielectric function for the 5×5 supercell with (black) and without (red) sulfur vacancies. Red (gray) filled curves are the joint density of states (JDOS) from the three highest valence bands to the two defect (six lowest conduction) bands. (D) Defect formation energy for a sulfur vacancy with $q = 0$ and $q = -1$, as a function of the Fermi energy (referenced to the conduction band minimum). Solid lines are energies of $q = 0$ ($q = -1$) obtained at their respective equilibrium configurations; dashed lines are obtained at the equilibrium configuration of the alternative $q = -1$ ($q = 0$) state. The thermodynamic charge transition level can be found at the cross-over between the two solid lines. (E) Schematic for the defect energies of neutral and charged defects, as a function of the collective coordinates of a system. Optical emission energies can take values between $E_{\text{PL}1}$ and $E_{\text{PL}1}$.

states $q = 0, -1$ as a function of the Fermi energy, as shown by the solid lines in Fig. C.6D, where the Fermi energy is referenced to the conduction band minimum; the thermodynamic charge transition energy $\epsilon(0/-1)$ can then be determined as the Fermi energy (electron chemical potential) where the most favorable charged state changes from $q = 0$ to -1 (Freysoldt et al., 2014; Van de Walle and Neugebauer, 2004; Gallino et al., 2010; Komsa et al., 2014). Total energies of charged defects were calculated from 6×6 supercell geometries containing an isolated sulfur vacancy, using the “special vacuum” method tailored for 2D materials that takes advantage of cancellation between two errors: the interaction of a charged defect with its periodic images and with the positive jellium background (Komsa and Krasheninnikov, 2015). The chemical potential of sulfur μ_S is needed to calculate the vacancy formation energy for each charged state, but does not affect their *relative* energies, *i.e.* charge transition energies are independent of μ_S . Hence a μ_S is chosen for the calculation but the vertical axis left unmarked in Fig. C.6D. We find that sulfur vacancies in WS_2 only support stable formation of $q = 0$ and -1 vacancies as the Fermi energy is varied from the valence band edge to the conduction band edge, similar to a previous study on MoS_2 (Komsa and Krasheninnikov, 2015) (the $q = -2$ state is found to be less favorable for all Fermi energies within the band gap and is thus omitted for clarity). The $\epsilon(0/-1)$ transition energy lies 0.33 eV below the conduction band minimum.

$\epsilon(0/-1)$ reflects the energy difference between two charged states in their respective equilibrium configurations: the $q = -1$ state relaxed into configuration $\{\mathbf{R}\}_{q=-1}$ and the $q = 0$ state relaxed into $\{\mathbf{R}\}_{q=0}$, as shown schematically in Fig. 5E, where the horizontal axis $\{\mathbf{R}\}$ represents the collective ionic coordinates of the system. Optical transitions occur on a much shorter timescales than lattice relaxation, therefore optical transition energies were evaluated with fixed atomic positions, as described below. After an electron is excited to the conduction band and decays into a defect

state D^- , it can decay radiatively to the valence band (e_{VB}), leaving behind a neutral defect D^0 (jointly denoted as $D^0 + e_{\text{VB}}$ in Fig. C.6E).

Among the possible emission dynamics, two extreme cases are considered (Gallino et al., 2010): if this decay occurs very quickly after occupation of the D^- state, then the D^- state retains the $\{\mathbf{R}\}_{q=0}$ atomic configuration of its progenitor D^0 state, *i.e.* it emits a photon at $E_{\text{PL}2}$ (blue arrow); this energy can be determined from the (0/ - 1) charge crossover when both state are held at the equilibrium configuration for $q = 0$ (see dashed blue line in Fig. 5D). If the electron dwells in D^- long enough to relax into its equilibrium position $\{\mathbf{R}\}_{q=-1}$, then the subsequent emission will occur at $E_{\text{PL}1}$, with initial and final states held at the $\{\mathbf{R}\}_{q=-1}$ configuration (orange arrow and dashed line in Fig. C.6D and C.6E). These extreme cases bracket a range of allowed emission energies between $E_{\text{PL}1}$ and $E_{\text{PL}2}$, which are 0.42 and 0.21 eV below the conduction band edge. Finally, assuming that the neutral exciton binding energy is comparable to the *total* defect-bound exciton binding energy (*i.e.* the binding between an neutral exciton and a charged defect is much weaker than the neutral exciton binding energy), we can infer that the emission energy of the bound exciton is also approximately 420 – 210 meV below the neutral exciton emission energy. This is consistent with the peak position and broad linewidth of the bound exciton peak, which spans from 200 to 400 meV below the neutral exciton emission energy. Since the above broadening mechanism requires an excitation lifetime comparable to the lattice relaxation time (which must exceed the characteristic phonon period), lifetime broadening is negligible in this scenario, compared to the observed width. Lifetime broadening of a shorter-lived excited state and/or inhomogeneous broadening could also be considered, in alternative scenarios.

To determine whether the transition from the defect state $X^{\text{B}2}$ is optically active, we also calculated the optical transition matrix elements between the valence band and the conduction or defect band states of a

5×5 WS_2 supercell containing one sulfur vacancy, as shown in Fig. C.6B. That is, we assume that the optical transition matrix element between two many-body states (before and after electron-hole recombination) mainly consists of matrix elements between single-particle valence band states and defect/conduction band states (by expanding many-body states into single-particle electron-hole pairs, under the Tamm-Dancoff approximation (Rohlfing and Louie, 2000)). The magnitude of the matrix element for each vertical transition is represented by the radius of a pair of circles marking the initial and final states for that transition, the color of those same circles representing the energy of that transition. Apart from the expected large matrix element between the valence band maximum and conduction band minimum at the \mathbf{K} point, the matrix elements between the highest valence band and the defect bands are also significant, indicating possible channels of bound exciton recombination. We further calculated the imaginary part of the dielectric function ($\epsilon_{xx} = \epsilon_{yy}$) in a 5×5 WS_2 supercell with and without one sulfur vacancy, as shown in Fig. C.6C. Due to the relative large size of these systems, the dielectric function was calculated within the Random Phase Approximation (RPA) without including local field effects (Gajdoš et al., 2006). The band gap calculated at the DFT-RPA level, 1.82 eV, is underestimated, but happens to agree with the PL measurement better than the quasi-particle band gap, due to partial cancellation of quasi-particle effects and exciton binding (Shi et al., 2013b; Komsa and Krasheninnikov, 2012). The joint density of states (JDOS) in the 5×5 structure is also superimposed as filled plots: red (gray) curves are the JDOS from the three highest valence bands to the two defect (six lowest conduction) bands. As expected, the defect states introduce an additional low-energy feature at ~ 1.5 eV, corresponding to the transition X^{B_2} .

To rule out possibilities that the bound exciton states are introduced by adsorbed gas molecules during the PL experiment (conducted in ambient

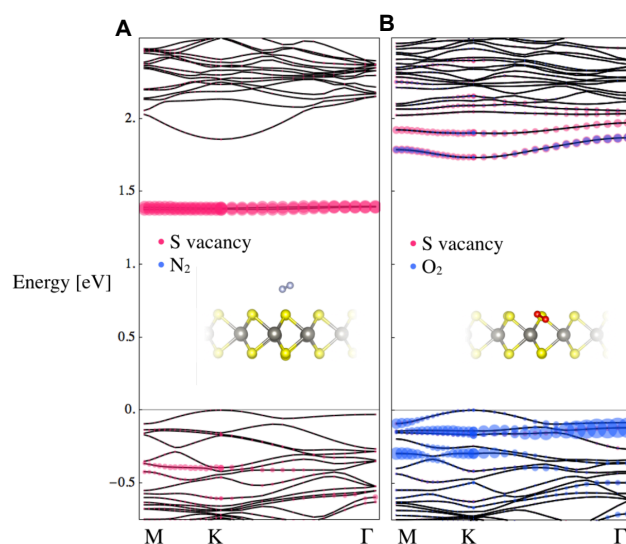


Figure C.7: **Band structure of a 5×5 WS_2 supercell with an N_2 or O_2 molecule adsorbed on the surface at a sulfur vacancy site.** The bands with red or blue circles superimposed mainly consist of atomic orbitals near a sulfur vacancy or on a gas molecule for (A) N_2 or (B) O_2 .

nitrogen), the interactions between sulfur vacancies and two types of gas molecules, nitrogen and oxygen (from residual oxygen), are also modeled within DFT and shown in fig. C.7. A N_2 molecule is found to physically adsorb onto the vacancy site and introduces no new levels near the band edges or mid-gap in the WS_2 system, while an O_2 molecule is found to strongly bind to a vacancy site, significantly altering the orbital characters the band edge states, but it only introduces mid-gap states within ~ 100 meV of the conduction band minimum. Hence neither gas molecule are expected to induce the observed defect-bound excitons ~ 300 meV below the neutral exciton energy.

The electronic structure and the optical response of another type of point defect frequently observed in STEM images, WS_3 vacancies, is also

shown in fig. C.8. Although WS_3 vacancies introduce mid-gap states 0.3–0.9 eV below the conduction band minimum (as shown by the orbital-projected band structure in fig. C.8A, where the defect bands are in red) and have finite optical transition matrix elements with the valence band edge states (as shown in fig. C.8B), they are not expected to dominate the optical spectra since they are estimated to be 25 times less common than sulfur vacancies, based on STEM image analysis (*i.e.* their relative small population compared to sulfur vacancies).

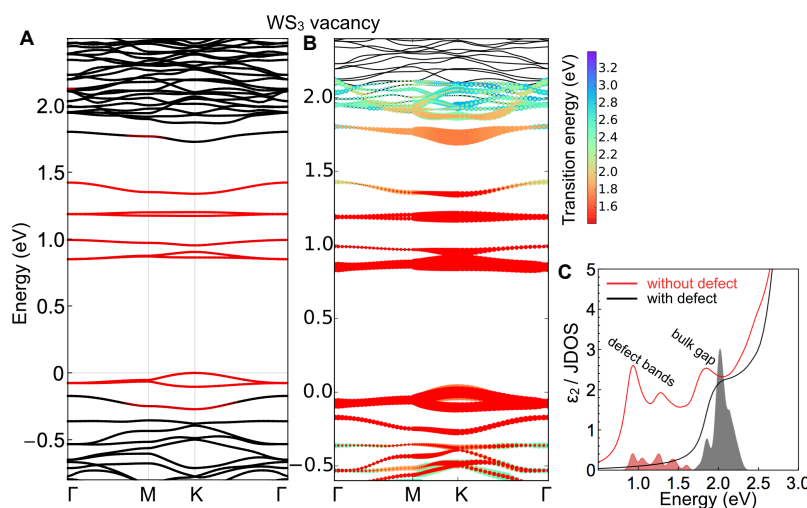


Figure C.8: Band structure of a WS_3 vacancy within a 5×5 supercell. (A) The red component of the colored bands indicates projection onto d orbitals of the six W atoms closest to the missing W atom. (B) The dominant optical transition matrix elements between valence and conduction bands, as indicated by pairs of circles on the initial and final states. The colors of the circles represent the transition energy and the radii represent the magnitude of the matrix element. (C) Imaginary dielectric function (unfilled curves) and joint density of states (filled plots) of a 5×5 WS_2 supercell containing a WS_3 vacancy. Red (black) filled curves are the JDOS from the valence bands to the defect (conduction) bands.

Conclusion

In summary, the interior and edge regions of as-grown monolayer WS₂ triangular islands have been investigated using photoluminescence spectroscopy, scanning electron microscopy, and first-principle calculations. In the PL spectra at low temperature, two additional features X^{B1} and X^{B2} corresponding to bound excitons can be observed only at the edges and not in the interior. A lower mono-sulfur vacancies density in the interior, $0.33 \pm 0.11 \text{ nm}^{-2}$, was confirmed by atomic resolution images, as compared to a much larger concentration near the island edges. Optical pumping experiments revealed sub-linear behavior for both bound exciton transitions when increasing the power density, which is a signature of defect-bound species. In addition, temperature-dependent PL measures showed that a bound exciton dissociates into a neutral exciton and a negative defect at relatively low temperatures, circa 107 K. First-principle calculations of defective WS₂ reveals a finite optical transition matrix element between the highest valence band and the mid-gap states introduced by sulfur vacancies.

REFERENCES

-
- Ashcroft, Neil W., and N. David Mermin. 1976. Introduction to solid state physics. *Saunders, Philadelphia*.
- Bao, Wei, Nicholas J. Borys, Changhyun Ko, Joonki Suh, Wen Fan, Andrew Thron, Yingjie Zhang, Alexander Buyanin, Jie Zhang, Stefano Cabrini, Paul D. Ashby, Alexander Weber-Bargioni, Sefaattin Tongay, Shaul Aloni, D. Frank Ogletree, Junqiao Wu, Miquel B. Salmeron, and P. James Schuck. 2015. Visualizing nanoscale excitonic relaxation properties of disordered edges and grain boundaries in monolayer molybdenum disulfide. *Nature Communications* 6:7993.
- Baranov, A. V., A. N. Bekhterev, Y. S. Bobovich, and V. I. Petrov. 1987. Interpretation of certain characteristics in Raman spectra of graphite and glassy carbon. *Opt. Spectrosk.* 62:1036–1042.
- Barros, E. B., and M. S. Dresselhaus. 2014. Theory of raman enhancement by two-dimensional materials: Applications for graphene-enhanced raman spectroscopy. *Physical Review B* 90(3):035443.
- Beal, A. R., and H. P. Hughes. 1979. Kramers-Kronig analysis of the reflectivity spectra of 2H-MoS₂, 2H-MoSe₂ and 2H-MoTe₂. *Journal of Physics C: Solid State Physics* 12:881.
- Beal, A. R., J. C. Knights, and W. Y. Liang. 1972. Transmission spectra of some transition metal dichalcogenides. ii. group via: trigonal prismatic coordination. *Journal of Physics C: Solid State Physics* 5(24):3540.
- Berkdemir, Ayse, Humberto R. Gutierrez, Andres R. Botello-Mendez, Nestor Perea-Lopez, Ana Laura Elias, Chen-Ing Chia, Bei Wang, Vincent H. Crespi, Florentino Lopez-Urias, Jean-Christophe Charlier, Humberto Terrones, and Mauricio Terrones. 2013. Identification of individual and few layers of ws₂ using raman spectroscopy. *Scientific Reports* 3:1755.

Berkelbach, Timothy C., Mark S. Hybertsen, and David R. Reichman. 2013. Theory of neutral and charged excitons in monolayer transition metal dichalcogenides. *Physical Review B* 88(4):045318.

Bromley, R. A., R. B. Murray, and A. D. Yoffe. 1972. The band structures of some transition metal dichalcogenides. iii. group via: trigonal prism materials. *Journal of Physics C: Solid State Physics* 5(7):759.

Burstein, E., Y. J. Chen, C. Y. Chen, S. Lundquist, and E. Tosatti. 1979. "giant" raman scattering by adsorbed molecules on metal surfaces. *Solid State Communications* 29(8):567–570.

Butler, Sheneve Z., Shawna M. Hollen, Linyou Cao, Yi Cui, Jay A. Gupta, Humberto R. Gutiérrez, Tony F. Heinz, Seung Sae Hong, Jiaying Huang, Ariel F. Ismach, Ezekiel Johnston-Halperin, Masaru Kuno, Vladimir V. Plashnitsa, Richard D. Robinson, Rodney S. Ruoff, Sayeef Salahuddin, Jie Shan, Michael G. Spencer Li Shiâ—, Mauricio TerronesvWolfgang Windl, and Joshua E. Goldberger. 2013. Progress, Challenges, and Opportunities in Two-Dimensional Materials Beyond Graphene. *ACS Nano* 7(4):2898–2926.

Cançado, L. G., M. A. Pimenta, R. Saito, A. Jorio, L. O. Ladeira, A. Grueneis, A. G. Souza-Filho, G. Dresselhaus, and M. S. Dresselhaus. 2002. Stokes and anti-stokes double resonance raman scattering in two-dimensional graphite. *Physical Review B* 66:035415.

Cardona, Manuel, and Gernot Güntherodt. 1982. *Light scattering in solids ii*, vol. 8 of *Topics in Applied Physics*. Springer Berlin Heidelberg.

Carvalho, Bruno R., Yufeng Hao, Joaquin F. Rodriguez-Nieva, Luigi Colombo, Rodney S. Ruoff, Marcos A. Pimenta, and Cristiano Fantini. 2015a. Probing carbon isotope effects on the Raman spectra of graphene with different ¹³C concentrations. *Physical Review B* 92:125406.

Carvalho, Bruno R., Leandro M. Malard, Juliana M. Alves, Cristiano Fantini, and Marcos A. Pimenta. 2015b. Symmetry-Dependent Exciton-Phonon Coupling in 2D and Bulk MoS₂ Observed by Resonance Raman Scattering. *Physical Review Letters* 114:136403 – Erratum: 2016. *Physical Review Letters* 116:089904.

Carvalho, Bruno R., Yuanxi Wang, Sandro Mignuzzi, Debdulal Roy, Mauricio Terrones, Cristiano Fantini, Vincent H. Crespi, Leandro M. Malard, and Marcos A. Pimenta. 2017. Intervalley scattering by acoustic phonons in two-dimensional MoS₂ revealed by double-resonance Raman spectroscopy. *Nature Communications* 8:14670.

Castellanos-Gomez, Andres, Nicolas Agrait, and Gabino Rubio-Bollinger. 2010. Optical identification of atomically thin dichalcogenide crystals. *Applied Physics Letters* 96(21):213116.

Cerdeira, F., W. Dreybrodt, and M. Cardona. 1972. Resonant raman scattering in germanium. *Solid State Communications* 10(7):591–595.

Chae, Seung Jin, Fethullah Günes, Ki Kang Kim, Eun Sung Kim, Gang Hee Han, Soo Min Kim, Hyeon-Jin Shin, Seon-Mi Yoon, Jae-Young Choi, Min Ho Park, Cheol Woong Yang, Didier Pribat, and Young Hee Lee. 2009. Synthesis of large-area graphene layers on poly-nickel substrate by chemical vapor deposition: Wrinkle formation. *Advanced Materials* 21(22):2328–2333.

Chakraborty, Biswanath, Achintya Bera, D. V. S. Muthu, Somnath Bhowmick, U. V. Waghmare, and A. K. Sood. 2012. Symmetry-dependent phonon renormalization in monolayer MoS₂ transistor. *Physical Review B* 85:161403.

Chakraborty, Biswanath, H. S. S. Ramakrishna Matte, A. K. Sood, and C. N. R. Rao. 2013. Layer-dependent resonant Raman scattering of a few layer MoS₂. *Journal of Raman Spectroscopy* 44(1):92–96.

Cheiwchanchamnangij, Tawinan, and Walter R. L. Lambrecht. 2012. Quasiparticle band structure calculation of monolayer, bilayer, and bulk MoS₂. *Physical Review B* 85:205302.

Chen, J. M., and C. S. Wang. 1974. Second order Raman spectrum of MoS₂. *Solid State Communications* 14(9):857 – 860.

Chow, Philippe K., Robin B. Jacobs-Gedrim, Jian Gao, Toh ming Lu, Bin Yu, Humberto Terrones, and Nikhil Koratkar. 2015. Defect-Induced Photoluminescence in Monolayer Semiconducting Transition Metal Dichalcogenides. *ACS Nano* 9(2):1520–1527.

Coehoorn, R., C. Haas, and R. A. de Groot. 1987. Electronic structure of MoSe₂, MoS₂, and WSe₂. II. The nature of the optical band gaps. *Physical Review B* 35:6203–6206.

Cong, Chunxiao, Jingzhi Shang, Xing Wu, Bingchen Cao, Namphung Peimyoo, Caiyu Qiu, Litao Sun, and Ting Yu. 2014. Synthesis and Optical Properties of Large-Area Single-Crystalline 2D Semiconductor WS₂ Monolayer from Chemical Vapor Deposition. *Advanced Optical Materials* 2(2):131–136.

del Corro, Elena, Humberto Terrones, Ana Elias, Cristiano Fantini, Simin Feng, Minh An Nguyen, Thomas E. Mallouk, Mauricio Terrones, and Marcos A. Pimenta. 2014. Excited excitonic states in 1L, 2L, 3L, and bulk WSe₂ observed by resonant Raman spectroscopy. *ACS Nano* 8(9): 9629–9635.

Delhaes, Pierre. 2000. *Graphite and precursors*, vol. 1. CRC Press.

Delhaye, Michel, Jacques Barbillat, Jean Aubard, and Edouard Da Silva Michel Bridoux. 1996. *Raman microscopy, development and applications*. Academic, San Diego.

Endo, Morinobu, Yoong Ahm Kim, Takuya Hayashi, Hiroyuki Muramatsu, Mauricio Terrones, Riichiro Saito, Federico Villalpando-Paez, Shin Grace Chou, and Mildred S. Dresselhaus. 2006. Nanotube coalescence-inducing mode: A novel vibrational mode in carbon systems. *Small* 2(8-9):1031–1036.

Fan, Jia-He, Po Gao, An-Min Zhang, Bai-Ren Zhu, Hua-Ling Zeng, Xiao-Dong Cui, Rui He, and Qing-Ming Zhang. 2014. Resonance Raman scattering in bulk 2H-MX_2 ($\text{M}=\text{Mo}, \text{W}$; $\text{X}=\text{S}, \text{Se}$) and monolayer MoS_2 . *Journal of Applied Physics* 115(5):053527.

Fantini, C., E. Cruz, A. Jorio, M. Terrones, H. Terrones, G. Van Lier, J.-C. Charlier, M. S. Dresselhaus, R. Saito, Y. A. Kim, T. Hayashi, H. Muramatsu, M. Endo, and M. A. Pimenta. 2006. Resonance raman study of linear carbon chains formed by the heat treatment of double-wall carbon nanotubes. *Physical Review B* 73(19):193408.

Feldmann, J., G. Peter, E. O. Göbel, P. Dawson, K. Moore, C. Foxon, and R. J. Elliott. 1987. Linewidth dependence of radiative exciton lifetimes in quantum wells. *Physical Review Letters* 59(20):2337–2340.

Feng, Simin, Maria Cristina dos Santos, Bruno R. Carvalho, Ruitao Lv, Qing Li, Kazunori Fujisawa, Ana Laura Elías, Yu Lei, Nestor Perea-López, Morinobu Endo, Minghu Pan, Marcos A. Pimenta, and Mauricio Terrones. 2016. Ultrasensitive molecular sensor using N-doped graphene through enhanced Raman scattering. *Science Advances* 2(7).

Ferrari, A. C., J. C. Meyer, V. Scardaci, C. Casiraghi, M. Lazzeri, F. Mauri, S. Piscanec, D. Jiang, K. S. Novoselov, S. Roth, and A. K. Geim. 2006. Raman spectrum of graphene and graphene layers. *Physical Review Letters* 97:187401.

- Fleischmann, Martin, Patrick J Hendra, and AJ McQuillan. 1974. Raman spectra of pyridine adsorbed at a silver electrode. *Chemical Physics Letters* 26(2):163–166.
- Frey, Gitti L., Reshef Tenne, Manyalibo J. Matthews, M. S. Dresselhaus, and G. Dresselhaus. 1999. Raman and resonance Raman investigation of MoS₂ nanoparticles. *Physical Review B* 60:2883–2892.
- Freysoldt, Christoph, Blazej Grabowski, Tilmann Hickel, Jörg Neugebauer, Georg Kresse, Anderson Janotti, and Chris G. Van de Walle. 2014. First-principles calculations for point defects in solids. *Review of Modern Physics* 86:253–305.
- Frindt, R. F. 1966. Single crystals of MoS₂ several molecular layers thick. *Journal of Applied Physics* 37(4):1928–1929.
- Gallino, Federico, Gianfranco Pacchioni, and Cristiana Di Valentin. 2010. Transition levels of defect centers in zno by hybrid functionals and localized basis set approach. *The Journal of Chemical Physics* 133(14).
- García-Cristóbal, A., A. Cantarero, C. Trallero-Giner, and M. Cardona. 1994. Excitonic model for second-order resonant raman scattering. *Physical Review B* 49:13430–13445.
- Golasa, K., M. Grzeszczyk, P. Leszczyński, C. Faugeras, A. A. L. Nicolet, A. Wysmolek, M. Potemski, and A. Babiński. 2014. Multiphonon resonant Raman scattering in MoS₂. *Applied Physics Letters* 104(9):092106.
- Golberg, D., Y. Bando, C. C. Tang, and C. Y. Zhi. 2007. Boron nitride nanotubes. *Advanced Materials* 19(18):2413–2432.
- Gong, Yongji, Junhao Lin, Xingli Wang, Gang Shi, Sidong Lei, Zhong Lin, Xiaolong Zou, Gonglan Ye, Robert Vajtai, Boris I. Yakobson, Humberto Terrones, Mauricio Terrones, Beng Kang Tay, Jun Lou, Sokrates T. Pantelides, Zheng Liu, Wu Zhou, and Pulickel M. Ajayan. 2014. Vertical and

in-plane heterostructures from WS₂/MoS₂ monolayers. *Nature Materials* 13:1135–1142.

Habenicht, Carsten, Martin Knupfer, and Bernd Büchner. 2015. Investigation of the dispersion and the effective masses of excitons in bulk 2H-MoS₂ using transition electron energy-loss spectroscopy. *Physical Review B* 91:245203.

Hamby, D. W., D. a. Lucca, M. J. Klopstein, and G. Cantwell. 2003. Temperature dependent exciton photoluminescence of bulk ZnO. *Journal of Applied Physics* 93(6):3214–3217.

Hao, Qingzhen, Bei Wang, Jeremy A Bossard, Brian Kiraly, Yong Zeng, I-Kao Chiang, Lasse Jensen, Douglas H Werner, and Tony Jun Huang. 2012. Surface-enhanced raman scattering study on graphene-coated metallic nanostructure substrates. *The Journal of Physical Chemistry C* 116(13): 7249–7254.

Hao, Qingzhen, Yong Zeng, Bala Krishna Juluri, Xiande Wang, Brian Kiraly, I-Kao Chiang, Lasse Jensen, Douglas H. Werner, Vincent H. Crespi, and Tony Jun Huang. 2011. Metallic membranes with subwavelength complementary patterns: Distinct substrates for surface-enhanced raman scattering. *ACS Nano* 5(7):5472–5477.

Heavens, Oliver S. 1991. *Optical properties of thin solid films*. Courier Corporation.

Hong, Jinhua, Zhixin Hu, Matt Probert, Kun Li, Danhui Lv, X Yang, Lin Gu, Nannan Mao, Qingliang Feng, Liming Xie, Jin Zhang, Dianzhong Wu, Zhiyong Zhang, Chuanhong Jin, Wei Ji, Xixiang Zhang, Jun Yuan, and Ze Zhang. 2015. Exploring atomic defects in molybdenum disulphide monolayers. *Nature Communications* 6:6293.

Huang, Shengxi, Xi Ling, Liangbo Liang, Yi Song, Wenjing Fang, Jin Zhang, Jing Kong, Vincent Meunier, and Mildred S. Dresselhaus. 2015. Molecular selectivity of graphene-enhanced raman scattering. *Nano letters* 15(5):2892–2901.

Jackson, John D. 2006. *klassische elektrodynamik*. Walter de Gruyter.

Jin, Zhenghe, Xiaodong Li, Jeffrey T. Mullen, and Ki Wook Kim. 2014. Intrinsic transport properties of electrons and holes in monolayer transition-metal dichalcogenides. *Physical Review B* 90:045422.

Jorio, Ado, Mildred S. Dresselhaus, Riichiro Saito, and Gene Dresselhaus. 2011. *Raman spectroscopy in graphene related systems*. Wiley-VCH; 1 edition.

Jorio, Ado, Erlon H. Martins Ferreira, Marcus V. O. Moutinho, Fernando Stavale, Carlos A. Achete, and Rodrigo B. Capaz. 2010. Measuring disorder in graphene with the g and d bands. *Physica Status Solidi (b)* 247(11-12): 2980–2982.

Kaasbjerg, Kristen, Kristian S. Thygesen, and Karsten W. Jacobsen. 2012. Phonon-limited mobility in n-type single-layer MoS₂ from first principles. *Physical Review B* 85:115317.

Kauschke, W., V. Vorlíček, and M. Cardona. 1987. Resonant Raman scattering in GaP: Excitonic and interference effects near the E₀ and E₀+Δ₀ gaps. *Physical Review B* 36(17):9129.

Kioseoglou, George, Aubrey T. Hanbicki, Marc Currie, Adam L. Friedman, and Berend T. Jonker. 2016. Optical polarization and intervalley scattering in single layers of MoS₂ and MoSe₂. *Scientific Reports* 6.

Klar, P., E. Lidorikis, A. Eckmann, I. A. Verzhbitskiy, A. C. Ferrari, and C. Casiraghi. 2013. Raman scattering efficiency of graphene. *Physical Review B* 87:205435.

Klingshirn, Claus F. 2012. *Semiconductor optics*. Springer Science & Business Media.

Klots, A. R., A. K. M. Newaz, B. Wang, D. Prasai, H. Krzyzanowska, J. Lin, D. Caudel, N. J. Ghimire, J. Yan, B. L. Ivanov, K. A. Velizhanin, A. Burger, D. G. Mandrus, N. H. Tolk, S. T. Pantelides, and K. I. Bolotin. 2014. Probing excitonic states in suspended two-dimensional semiconductors by photocurrent spectroscopy. *Scientific Reports* 4.

Komsa, Hannu-Pekka, Natalia Berseneva, Arkady V. Krasheninnikov, and Risto M. Nieminen. 2014. Charged point defects in the flatland: Accurate formation energy calculations in two-dimensional materials. *Physical Review X* 4:031044.

Komsa, Hannu Pekka, and Arkady V. Krasheninnikov. 2012. Effects of confinement and environment on the electronic structure and exciton binding energy of MoS₂ from first principles. *Physical Review B* 86:241201.

Komsa, Hannu-Pekka, and Arkady V. Krasheninnikov. 2015. Native defects in bulk and monolayer MoS₂ from first principles. *Physical Review B* 91:125304.

Kormányos, Andor, Viktor Zólyomi, Neil D. Drummond, Péter Rakyta, Guido Burkard, and Vladimir I. Fal'ko. 2013. Monolayer MoS₂: Trigonal warping, the Γ valley, and spin-orbit coupling effects. *Physical Review B* 88:045416.

Kozawa, Daichi, Rajeev Kumar, Alexandra Carvalho, Kiran Kumar Amara, Weijie Zhao, Shunfeng Wang, Minglin Toh, Ricardo M. Ribeiro, A. H. Castro Neto, Kazunari Matsuda, and Goki Eda. 2014. Photocarrier relaxation pathway in two-dimensional semiconducting transition metal dichalcogenides. *Nature Communications* 5:4543.

- Lampert, Murray A. 1958. Mobile and immobile effective mass-particle complex in nonmetallic solids. *Physical Review Letters* 1(12):450–452.
- Lee, Changgu, Hugen Yan, Louis E. Brus, Tony F. Heinz, James Hone, and Sunmin Ryu. 2010. Anomalous Lattice Vibrations of Single- and Few-Layer MoS₂. *ACS Nano* 4(5):2695–2700.
- Lee, Jae-Ung, Jaesung Park, Young-Woo Son, and Hyeonsik Cheong. 2015. Anomalous excitonic resonance Raman effects in few-layer MoS₂. *Nanoscale* 7:3229–3236.
- Lee, Yi Hsien, Xin Quan Zhang, Wenjing Zhang, Mu Tung Chang, Cheng Te Lin, Kai Di Chang, Ya Chu Yu, Jacob Tse Wei Wang, Chia Seng Chang, Lain Jong Li, and Tsung Wu Lin. 2012. Synthesis of large-area MoS₂ atomic layers with chemical vapor deposition. *Advanced Materials* 24(17):2320–2325.
- Li, Hong, Qing Zhang, Chin Chong Ray Yap, Beng Kang Tay, Teo Hang Tong Edwin, Aurelien Olivier, and Dominique Baillargeat. 2012a. From Bulk to Monolayer MoS₂: Evolution of Raman Scattering. *Advanced Functional Materials* 22(7):1385–1390.
- Li, Jiantong, and Mikael Östling. 2015. Scalable fabrication of 2d semi-conducting crystals for future electronics. *Electronics* 4(4):1033–1061.
- Li, Song-Lin, Hisao Miyazaki, Haisheng Song, Hiromi Kuramochi, Shu Nakaharai, and Kazuhito Tsukagoshi. 2012b. Quantitative raman spectrum and reliable thickness identification for atomic layers on insulating substrates. *ACS Nano* 6(8):7381–7388.
- Li, Xiaodong, Jeffrey T. Mullen, Zhenghe Jin, Kostyantyn M. Borysenko, M. Buongiorno Nardelli, and Ki Wook Kim. 2013. Intrinsic electrical transport properties of monolayer silicene and MoS₂ from first principles. *Physical Review B* 87:115418.

Li, Xuesong, Weiwei Cai, Jinho An, Seyoung Kim, Junghyo Nah, Dongxing Yang, Richard Piner, Aruna Velamakanni, Inhwa Jung, Emanuel Tutuc, Sanjay K. Banerjee, Luigi Colombo, and Rodney S. Ruoff. 2009. Large-area synthesis of high-quality and uniform graphene films on copper foils. *Science* 324(5932):1312–1314.

Limmer, W., H. Leiderer, K. Jakob, W. Gebhardt, W. Kauschke, A. Cantarero, and C. Trallero-Giner. 1990. Resonant Raman scattering by longitudinal-optical phonons in $Zn_{1-x}Mn_xSe$ ($x=0, 0.03, 0.1$) near the E_0 gap. *Physical Review B* 42(17):11325.

Lin, Zhong, Bruno R. Carvalho, Ethan Kahn, Ruitao Lv, Rahul Rao, Humberto Terrones, Marcos A. Pimenta, and Mauricio Terrones. 2016. Defect engineering of two-dimensional transition metal dichalcogenides. *2D Materials* 3(2):022002.

Lin, Zhong, Michael T. Thee, Ana Laura Elías, Simin Feng, Chanjing Zhou, Kazunori Fujisawa, Néstor Perea-López, Victor Carozo, Humberto Terrones, and Mauricio Terrones. 2014. Facile synthesis of MoS_2 and $Mo_xW_{1-x}S_2$ triangular monolayers. *APL Materials* 2(9):092514.

Ling, Xi, Shengxi Huang, Shibin Deng, Nannan Mao, Jing Kong, Mildred S. Dresselhaus, and Jin Zhang. 2015. Lighting up the raman signal of molecules in the vicinity of graphene related materials. *Accounts of chemical research* 48(7):1862–1870.

Ling, Xi, Luciano G. Moura, Marcos A. Pimenta, and Jin Zhang. 2012a. Charge-transfer mechanism in graphene-enhanced raman scattering. *The Journal of Physical Chemistry C* 116(47):25112–25118.

Ling, Xi, Juanxia Wu, Liming Xie, and Jin Zhang. 2013. Graphene-thickness-dependent graphene-enhanced raman scattering. *The Journal of Physical Chemistry C* 117(5):2369–2376.

- Ling, Xi, Juanxia Wu, Weigao Xu, and Jin Zhang. 2012b. Probing the effect of molecular orientation on the intensity of chemical enhancement using graphene-enhanced raman spectroscopy. *Small* 8(9):1365–1372.
- Ling, Xi, Liming Xie, Yuan Fang, Hua Xu, Haoli Zhang, Jing Kong, Mildred S Dresselhaus, Jin Zhang, and Zhongfan Liu. 2010. Can graphene be used as a substrate for raman enhancement? *Nano letters* 10(2):553–561.
- Ling, Xi, and Jin Zhang. 2010. First-layer effect in graphene-enhanced raman scattering. *Small* 6(18):2020–2025.
- Liu, Hsiang-Lin, Huaihong Guo, Teng Yang, Zhidong Zhang, Yasuaki Kumamoto, Chih-Chiang Shen, Yu-Te Hsu, Lain-Jong Li, Riichiro Saito, and Satoshi Kawata. 2015. Anomalous lattice vibrations of monolayer MoS₂ probed by ultraviolet Raman scattering. *Journal of Physics and Chemistry of Solids* 17:14561–14568.
- Liu, Hsiang-Lin, Chih-Chiang Shen, Sheng-Han Su, Chang-Lung Hsu, Ming-Yang Li, and Lain-Jong Li. 2014. Optical properties of monolayer transition metal dichalcogenides probed by spectroscopic ellipsometry. *Applied Physics Letters* 105(20):201905.
- Liu, Keng-Ku, Wenjing Zhang, Yi-Hsien Lee, Yu-Chuan Lin, Mu-Tung Chang, Ching-Yuan Su, Chia-Seng Chang, Hai Li, Yumeng Shi, Hua Zhang, Chao-Sung Lai, and Lain-Jong Li. 2012. Growth of Large-Area and Highly Crystalline MoS₂ Thin Layers on Insulating Substrates. *Nano Letters* 12(3):1538–1544.
- Livneh, Tsachi, and Jonathan E. Spanier. 2015. A comprehensive multi-phonon spectral analysis in MoS₂. *2D Materials* 2(3):035003.
- Loudon, Rodney. 1964. The raman effect in crystals. *Advances in Physics* 13(52):423–482.

Lucchese, Márcia Maria, F. Stavale, E. H. Martins Ferreira, C. Vilani, M. V. O. Moutinho, Rodrigo B. Capaz, C. A. Achete, and A. Jorio. 2010. Quantifying ion-induced defects and raman relaxation length in graphene. *Carbon* 48(5):1592–1597.

Lv, Ruitao, Qing Li, Andrés R Botello-Méndez, Takuya Hayashi, Bei Wang, Ayse Berkdemir, Qingzhen Hao, Ana Laura Elías, Rodolfo Cruz-Silva, Humberto R. Gutiérrez, Yoong Ahm Kim, Hiroyuki Muramatsu, Jun Zhu, Morinobu Endo, Humberto Terrones, Jean-Christophe Charlier, Minghu Pan, and Terrones Mauricio. 2012. Nitrogen-doped graphene: beyond single substitution and enhanced molecular sensing. *Scientific Reports* 2.

Lv, Ruitao, Maria Cristina dos Santos, Claire Antonelli, Simin Feng, Kazunori Fujisawa, Ayse Berkdemir, Rodolfo Cruz-Silva, Ana Laura Elías, Nestor Perea-Lopez, Florentino López-Urías, Humberto Terrones, and Mauricio Terrones. 2014. Large-area si-doped graphene: Controllable synthesis and enhanced molecular sensing. *Advanced Materials* 26(45): 7593–7599.

Lv, Ruitao, Humberto Terrones, Ana Laura Elías, Néstor Perea-López, Humberto R Gutiérrez, Eduardo Cruz-Silva, Lakshmy Pulickal Rajukumar, Mildred S Dresselhaus, and Mauricio Terrones. 2015. Two-dimensional transition metal dichalcogenides: Clusters, ribbons, sheets and more. *Nano Today* 10(5):559–592.

M. L. Bansal, M. Cardona, A. K. Sood. 1991. Strongly dispersive low frequency raman modes in germanium. *Solid State Communications* 78(7): 579–582.

Mak, Kin Fai, Keliang He, Changgu Lee, Gwan Hyoung Lee, James Hone, Tony F. Heinz, and Jie Shan. 2013. Tightly bound trions in monolayer MoS₂. *Nature Materials* 12(3):207–211.

- Mak, Kin Fai, Keliang He, Jie Shan, and Tony F. Heinz. 2012. Control of valley polarization in monolayer MoS₂ by optical helicity. *Nature Nanotechnology* 7:494–498.
- Mak, Kin Fai, Changgu Lee, James Hone, Jie Shan, and Tony F. Heinz. 2010. Atomically Thin MoS₂: A New Direct-Gap Semiconductor. *Physical Review Letters* 105:136805.
- Mak, Kin Fai, Kathryn L. McGill, Jiwoong Park, and Paul L. McEuen. 2014. The valley Hall effect in MoS₂ transistors. *Science* 344(6191):1489–1492.
- Malard, L. M., M. A. Pimenta, G. Dresselhaus, and M. S. Dresselhaus. 2009. Raman spectroscopy in graphene. *Physics Reports* 473(5-6):51–87.
- Martin, R. M., and L. M. Falicov. 1983. *Resonant raman scattering*, vol. 8 of *Topics in Applied Physics*. Springer Berlin Heidelberg.
- Martins, Luiz Gustavo Pimenta. 2015. High-pressure raman study of graphene: a spectroscopic evidence for the diamondol. Master's thesis, Universidade Federal de Minas Gerais.
- Maultzsch, J., S. Reich, and C. Thomsen. 2004. Double-resonant raman scattering in graphite: Interference effects, selection rules, and phonon dispersion. *Physical Review B* 70:155403.
- Mccreary, Amber, Ayse Berkdemir, Junjie Wang, Minh An Nguyen, Kazunori Fujisawa, Bernd Kabius, Victor Carozo, David A. Cullen, Thomas E. Mallouk, Jun Zhu, and Mauricio Terrones. 2016. Distinct photoluminescence and Raman spectroscopy signatures for identifying highly crystalline WS₂ monolayers produced by different growth methods. *Journal of Material Research* 31(7):931–944.
- Mertens, Jan, Yumeng Shi, Alejandro Molina-Sánchez, Ludger Wirtz, Hui Ying Yang, and Jeremy J Baumberg. 2014. Excitons in a mirror:

Formation of “optical bilayers” using MoS₂ monolayers on gold substrates. *Applied Physics Letters* 104(19):191105.

Meyer, Bruno K., H. Alves, D. M. Hofmann, W. Kriegseis, D. Forster, F. Bertram, J. Christen, A. Hoffmann, M. Straßburg, M. Dworzak, U. Habocek, and A. V. Rodina. 2004. Bound exciton and donor-acceptor pair recombinations in ZnO. *Physica Status Solidi (b)* 241(2):231–260.

Mignuzzi, Sandro, Andrew J. Pollard, Nicola Bonini, Barry Brennan, Ian S. Gilmore, Marcos A. Pimenta, David Richards, and Debdulal Roy. 2015. Effect of disorder on Raman scattering of single-layer MoS₂. *Physical Review B* 91:195411.

Mitioglu, A., P. Plochocka, J. Jadczyk, W. Escoffier, G. Rikken, L. Kulyuk, and D. K. Maude. 2013. Optical manipulation of the exciton charge state in single-layer tungsten disulfide. *Physical Review B* 88(245403):245403.

Mohr, M., M. Machón, J. Maultzsch, and C. Thomsen. 2006. Double-resonant Raman processes in germanium: Group theory and *ab initio* calculations. *Physical Review B* 73:035217.

Molina-Sánchez, A., D. Sangalli, K. Hummer, A. Marini, and L. Wirtz. 2013. Effect of spin-orbit interaction on the optical spectra of single-layer, double-layer, and bulk MoS₂. *Physical Review B* 88(4):045412.

Molina-Sánchez, A., and L. Wirtz. 2011. Phonons in single-layer and few-layer MoS₂ and WS₂. *Physical Review B* 84:155413.

Molina-Sánchez, Alejandro, Maurizia Palumbo, Andrea Marini, and Ludger Wirtz. 2016. Temperature-dependent excitonic effects in the optical properties of single-layer MoS₂. *Physical Review B* 93(15):155435.

Moreira, Leandro Malard. 2009. Raman spectroscopy of graphene: probing phonons, electrons and electron-phonon interactions. Ph.D. thesis, Universidade Federal de Minas Gerais.

Morton, Seth M, and Lasse Jensen. 2009. Understanding the molecule-surface chemical coupling in sers. *Journal of the American Chemical Society* 131(11):4090–4098.

Naumov, A., K. Wolf, T. Reisinger, H. Stanzl, and W. Gebhardt. 1993. Luminescence due to lattice mismatch defects in ZnTe layers grown by metalorganic vapor phase epitaxy. *Applied Physics Letters* 73(1993):2581.

Novoselov, K. S., D. Jiang, F. Schedin, T. J. Booth, V. V. Khotkevich, S. V. Morozov, and A. K. Geim. 2005. Two-dimensional atomic crystals. *Proceedings of the National Academy of Sciences of the United States of America* 102(30):10451–10453.

Novoselov, Kostya S., Andre K. Geim, Sergei V. Morozov, D. Jiang, Y. Zhang, Sergey V. Dubonos, Irina V. Grigorieva, and Alexandr A. Firsov. 2004. Electric field effect in atomically thin carbon films. *Science* 306: 666–669.

de Oliveira Lopes Cançado, Luiz Gustavo. 2006. Raman spectroscopy of nanographites. Ph.D. thesis, Universidade Federal de Minas Gerais.

Peimyoo, Namphung, Weihuang Yang, Jingzhi Shang, Xiaonan Shen, Yanlong Wang, and Ting Yu. 2014. Chemically Driven Tunable Light Emission of Charged and Neutral Excitons in Monolayer WS₂. *ACS Nano* 8(11):11320–11329.

Perea-López, Néstor, Ana Laura Elías, Ayse Berkdemir, Andres Castro-Beltran, Humberto R. Gutiérrez, Simin Feng, Ruitao Lv, Takuya Hayashi, Florentino López Urías, Sujoy Ghosh, Baleeswaraiiah Muchharla, Saikat Talapatra, Humberto Terrones, and Mauricio Terrones. 2013. Photosensor Device Based on Few-Layered WS₂ Films. *Advanced Functional Materials* 23(44):5511–5517.

Pham, V. D., F. Joucken, V. Repain, C. Chacon, A. Bellec, Y. Girard, S. Rousset, R. Sporcken, M. C. dos Santos, and J. Lagoute. 2016. Molecular adsorbates as probes of the local properties of doped graphene. *Scientific Reports* 6.

Pimenta, M. A., G. Dresselhaus, M. S. Dresselhaus, L. G. Cancado, A. Jorio, and R. Saito. 2007. Studying disorder in graphite-based systems by raman spectroscopy. *Physical Chemistry Chemical Physics* 9:1276–1290.

Pimenta, Marcos A., Elena del Corro, Bruno R. Carvalho, Cristiano Fantini, and Leandro M. Malard. 2015. Comparative Study of Raman Spectroscopy in Graphene and MoS₂-type Transition Metal Dichalcogenides. *Accounts of Chemical Research* 48:41–47.

Qiu, Caiyu, Haiqing Zhou, Huaichao Yang, Minjiang Chen, Yanjun Guo, and Lianfeng Sun. 2011. Investigation of n-layer graphenes as substrates for raman enhancement of crystal violet. *The Journal of Physical Chemistry C* 115(20):10019–10025.

Qiu, Diana Y., Felipe H. da Jornada, and Steven G. Louie. 2013. Optical Spectrum of MoS₂: Many-Body Effects and Diversity of Exciton States. *Physical Review Letters* 111:216805.

Ramasubramaniam, Ashwin. 2012. Large excitonic effects in monolayers of molybdenum and tungsten dichalcogenides. *Physical Review B* 86: 115409.

Regan, William, Nasim Alem, Benjamín Alemán, Baisong Geng, Çağlar Girit, Lorenzo Maserati, Feng Wang, Michael Crommie, and A. Zettl. 2010. A direct transfer of layer-area graphene. *Applied Physics Letters* 96(11):113102.

Reina, Alfonso, Xiaoting Jia, John Ho, Daniel Nezich, Hyungbin Son, Vladimir Bulovic, Mildred S. Dresselhaus, and Jing Kong. 2009. Large

area, few-layer graphene films on arbitrary substrates by chemical vapor deposition. *Nano Letters* 9(1):30–35.

Renucci, J. B., R. N. Tyte, and M. Cardona. 1975. Resonant raman scattering in silicon. *Physical Review B* 11:3885–3895.

Renucci, M. A., J. B. Renucci, R. Zeyher, and M. Cardona. 1974. Second-order Raman scattering in germanium in the vicinity of the E_1 , $E_1 + \Delta_1$ edges. *Physical Review B* 10:4309–4323.

Ribeiro-Soares, J., R. M. Almeida, E. B. Barros, P. T. Araujo, M. S. Dresselhaus, L. G. Cançado, and A. Jorio. 2014. Group theory analysis of phonons in two-dimensional transition metal dichalcogenides. *Physical Review B* 90:115438.

Rohlfing, Michael, and Steven G. Louie. 2000. Electron-hole excitations and optical spectra from first principles. *Physical Review B* 62:4927–4944.

Ross, Jason S., Sanfeng Wu, Hongyi Yu, Nirmal J. Ghimire, Aaron M. Jones, Grant Aivazian, Jiaqiang Yan, David G. Mandrus, Di Xiao, Wang Yao, and Xiaodong Xu. 2013. Electrical control of neutral and charged excitons in a monolayer semiconductor. *Nature Communications* 4:1474.

Scheuschner, Nils, Oliver Ochedowski, Marika Schleberger, and Janina Maultzsch. 2012. Resonant raman profiles and μ -photoluminescence of atomically thin layers of molybdenum disulfide. *Physica Status Solidi (b)* 249(12):2644–2647.

Sekine, T., T. Nakashizu, K. Toyoda, K. Uchinokura, and E. Matsuura. 1980a. Raman scattering in layered compound 2H-WS₂. *Solid State Communications* 35(4):371 – 373.

Sekine, Tomoyuki, Mitsuru Izumi, Tsuneo Nakashizu, Kunimitsu Uchinokura, and Etsuyuki Matsuura. 1980b. Raman Scattering and Infrared

Reflectance in 2H-MoSe₂. *Journal of the Physical Society of Japan* 49(3): 1069–1077.

Sekine, Tomoyuki, Kunimitsu Uchinokura, Tsuneo Nakashizu, Etsuyuki Matsuura, and Ryozo Yoshizaki. 1984. Dispersive Raman Mode of Layered Compound 2H-MoS₂ under the Resonant Condition. *Journal of the Physical Society of Japan* 53(2):811–818.

Shang, Jingzhi, Xiaonan Shen, Chunxiao Cong, Namphung Peimyoo, Bingchen Cao, Mustafa Eginligil, and Ting Yu. 2015. Observation of Excitonic Fine Structure in a 2D Transition-Metal Dichalcogenide Semiconductor. *ACS Nano* 9(1):647–655.

Shi, Hongliang, Hui Pan, Yong-Wei Zhang, and Boris I. Yakobson. 2013a. Quasiparticle band structures and optical properties of strained monolayer MoS₂ and WS₂. *Physical Review B* 87:155304.

Shi, Hongliang, Hui Pan, Yong Wei Zhang, and Boris I. Yakobson. 2013b. Quasiparticle band structures and optical properties of strained monolayer MoS₂ and WS₂. *Physical Review B* 87:155304.

Song, Li, Lijie Ci, Hao Lu, Pavel B. Sorokin, Chuanhong Jin, Jie Ni, Alexander G. Kvashnin, Dmitry G. Kvashnin, Jun Lou, Boris I. Yakobson, and Pulickel M. Ajayan. 2010. Large scale growth and characterization of atomic hexagonal boron nitride layers. *Nano Letters* 10(8):3209–3215.

Soubelet, P., A. E. Bruchhausen, A. Fainstein, K. Nogajewski, and C. Faugeras. 2016. Resonance effects in the Raman scattering of monolayer and few-layer MoSe₂. *Physical Review B* 93:155407.

Sourisseau, C., F. Cruege, M. Fouassier, and M. Alba. 1991. Second-order Raman effects, inelastic neutron scattering and lattice dynamics in 2H-WS₂. *Chemical Physics* 150(2):281 – 293.

Splendiani, Andrea, Liang Sun, Yuanbo Zhang, Tianshu Li, Jonghwan Kim, Chi-Yung Chim, Giulia Galli, and Feng Wang. 2010. Emerging Photoluminescence in Monolayer MoS₂. *Nano Letters* 10(4):1271–1275.

Stacy, A. M., and D. T. Hodul. 1985. Raman spectra of ivb and vib transition metal disulfides using laser energies near the absorption edges. *Journal of Physics and Chemistry of Solids* 46(4):405 – 409.

Sun, Linfeng, Jiayu Yan, Da Zhan, Lei Liu, Hailong Hu, Hong Li, Ben Kang Tay, Jer-Lai Kuo, Chung-Che Huang, Daniel W. Hewak, Pooi See Lee, and Ze Xiang Shen. 2013. Spin-Orbit Splitting in Single-Layer MoS₂ Revealed by Triply Resonant Raman Scattering. *Physical Review Letters* 111:126801.

Terrones, H., E. Del Corro, S. Feng, J. M. Poumirol, D. Rhodes, D. Smirnov, N. R. Pradhan, Z. Lin, M. A. T. Nguyen, A. L. Elias, T. E. Mallouk, L. Balicas, M. A. Pimenta, and M. Terrones. 2014. New first order raman-active modes in few layered transition metal dichalcogenides. *Scientific Reports* 4:4215.

Thomsen, C., and S. Reich. 2000. Double resonant raman scattering in graphite. *Physical Review Letters* 85:5214.

Tinkham, Michael. 1992. *Group theory and quantum mechanics*. McGraw Hill, New York.

Tongay, Sefaattin, Joonki Suh, Can Ataca, Wen Fan, Alexander Luce, Jeong Seuk Kang, Jonathan Liu, Changhyun Ko, Rajamani Raghunathanan, Jian Zhou, Frank Ogletree, Jingbo Li, Jeffrey C Grossman, and Junqiao Wu. 2013. Defects activated photoluminescence in two-dimensional semiconductors: interplay between bound, charged, and free excitons. *Scientific Reports* 3(2657):2657.

- Venezuela, Pedro, Michele Lazzeri, and Francesco Mauri. 2011. Theory of double-resonant raman spectra in graphene: Intensity and line shape of defect-induced and two-phonon bands. *Physical Review B* 84:035433.
- Verble, J. L., and T. J. Wieting. 1970. Lattice Mode Degeneracy in MoS₂ and Other Layer Compounds. *Physical Review Letters* 25:362–365.
- Voiry, Damien, Aditya Mohite, and Manish Chhowalla. 2015. Phase engineering of transition metal dichalcogenides. *Chemical Society Reviews* 44(9):2702–2712.
- Gajdoš, M., K. Hummer, G. Kresse, J. Furthmüller, and F. Bechstedt. 2006. Linear optical properties in the projector-augmented wave methodology. *Physical Review B* 73:045112.
- Van de Walle, Chris G., and Jörg Neugebauer. 2004. First-principles calculations for defects and impurities: Applications to iii-nitrides. *Journal of Applied Physics* 95(8):3851–3879.
- Wilson, J. A., and A. D. Yoffe. 1969. The transition metal dichalcogenides discussion and interpretation of the observed optical, electrical and structural properties. *Advances in Physics* 18(73):193–335.
- Wu, Fengcheng, Fanyao Qu, and A. H. MacDonald. 2015a. Exciton band structure of monolayer MoS₂. *Physical Review B* 91:075310.
- Wu, Sanfeng, Sonia Buckley, John R. Schaibley, Liefeng Feng, Jiaqiang Yan, David G. Mandrus, Fariba Hatami, Wang Yao, Jelena Vučković, Arka Majumdar, and Xiaodong Xu. 2015b. Monolayer semiconductor nanocavity lasers with ultralow thresholds. *Nature* 420:69–72.
- Xiao, Di, Gui-Bin Liu, Wanxiang Feng, Xiaodong Xu, and Wang Yao. 2012. Coupled Spin and Valley Physics in Monolayers of MoS₂ and Other Group-VI Dichalcogenides. *Physical Review Letters* 108:196802.

- Xie, Liming, Xi Ling, Yuan Fang, Jin Zhang, and Zhongfan Liu. 2009. Graphene as a substrate to suppress fluorescence in resonance raman spectroscopy. *Journal of the American Chemical Society* 131(29):9890–9891.
- Xu, Hua, Yabin Chen, Weigao Xu, Haoli Zhang, Jing Kong, Mildred S. Dresselhaus, and Jin Zhang. 2011a. Modulating the charge-transfer enhancement in gers using an electrical field under vacuum and an n/p-doping atmosphere. *Small* 7(20):2945–2952.
- Xu, Hua, Liming Xie, Haoli Zhang, and Jin Zhang. 2011b. Effect of graphene fermi level on the raman scattering intensity of molecules on graphene. *ACS Nano* 5(7):5338–5344.
- Xu, Weigao, Jiaqi Xiao, Yanfeng Chen, Yabin Chen, Xi Ling, and Jin Zhang. 2013. Graphene-veiled gold substrate for surface-enhanced raman spectroscopy. *Advanced Materials* 25(6):928–933.
- Xu, Xiaodong, Wang Yao, Di Xiao, and Tony F. Heinz. 2014. Spin and pseudospins in layered transition metal dichalcogenides. *Nature Physics* 10:343–350.
- Yang, Li, Jack Deslippe, Cheol-Hwan Park, Marvin L. Cohen, and Steven G. Louie. 2009. Excitonic effects on the optical response of graphene and bilayer graphene. *Physical Review Letters* 103:186802.
- Yoon, Duhee, Hyerim Moon, Young-Woo Son, Jin Sik Choi, Bae Ho Park, Young Hun Cha, Young Dong Kim, and Hyeonsik Cheong. 2009. Interference effect on Raman spectrum of graphene on SiO₂/Si. *Physical Review B* 80:125422.
- You, Yumeng, Xiao Xiao Zhang, Timothy C. Berkelbach, Mark S. Hybertsen, David R. Reichman, and Tony F. Heinz. 2015. Observation of biexcitons in monolayer WSe₂. *Nature Physics* 11:477–482.

- Yu, Peter Y., and Manuel Cardona. 2010. *Fundamentals of semiconductors*. Springer-Verlag Berlin Heidelberg, New York.
- Yu, Qingkai, Luis A. Jauregui, Wei Wu, Robert Colby, Jifa Tian, Zhihua Su, Helin Cao, Zhihong Liu, Dongguang Wei Deepak Pandey, Ting Fung Chung, Peng Peng, Nathan P. Guisinger, Eric A. Stach, Jiming Bao, Shin-Shem Pei, and Yong P. Chen. 2011a. Control and characterization of individual grains and grain boundaries in graphene grown by chemical vapour deposition. *Nature Materials* 10(6):443–449.
- Yu, Xinxin, Hongbing Cai, Wenhua Zhang, Xinjing Li, Nan Pan, Yi Luo, Xiaoping Wang, and J. G. Hou. 2011b. Tuning chemical enhancement of sers by controlling the chemical reduction of graphene oxide nanosheets. *ACS Nano* 5(2):952–958.
- Yuan, Shengjun, Rafael Roldán, M. I. Katsnelson, and Francisco Guinea. 2014. Effect of point defects on the optical and transport properties of MoS₂ and WS₂. *Physical Review B* 90(041402):041402.
- Zeng, Hualing, Junfeng Dai, Wang Yao, Di Xiao, and Xiaodong Cui. 2012. Valley polarization in MoS₂ monolayers by optical pumping. *Nature Nanotechnology* 7:490–493.
- Zhan, Yongjie, Zheng Liu, Sina Najmaei, Pulickel M. Ajayan, and Jun Lou. 2012. Large-area vapor-phase growth and characterization of MoS₂ atomic layers on a SiO₂ substrate. *Small* 8(7):966–971.
- Zhang, Xin Quan, Chin Hao Lin, Yu Wen Tseng, Kuan Hua Huang, and Yi Hsien Lee. 2015. Synthesis of Lateral Heterostructures of Semiconducting Atomic Layers. *Nano Letters* 15(1):410–415.
- Zhao, Weijie, Ricardo Mendes Ribeiro, and Goki Eda. 2015. Electronic structure and optical signatures of semiconducting transition metal dichalcogenide nanosheets. *Accounts of Chemical Research* 48(1):91–99.

Zheng, Shoujun, Linfeng Sun, Tingting Yin, Alexander M. Dubrovkin, Fucui Liu, Zheng Liu, Ze Xiang Shen, and Hong Jin Fan. 2015. Monolayers of $W_xMo_{1-x}S_2$ alloy heterostructure with in-plane composition variations. *Applied Physics Letters* 106:063113.

Zhou, Wu, Xiaolong Zou, Sina Najmaei, Zheng Liu, Yumeng Shi, Jing Kong, Jun Lou, Pulickel M. Ajayan, Boris I. Yakobson, and Juan Carlos Idrobo. 2013. Intrinsic Structural Defects in Monolayer Molybdenum Disulfide. *Nano Letters* 13:2615–2622.

Zhu, H. W., C. L. Xu, D. H. Wu, B. Q. Wei, R. Vajtai, and P. M. Ajayan. 2002. Direct synthesis of long single-walled carbon nanotube strands. *Science* 296(5569):884–886.